San Jose State University

SJSU ScholarWorks

Spring 2020

A Three Dimensional Adaptive Mesh Refinement Hydrodynamical Simulation of Eta Carinae's Colliding Stellar Winds Around Periastron

Trung Peter Ho
San Jose State University

Follow this and additional works at: https://scholarworks.sjsu.edu/etd_theses

A THREE DIMENSIONAL ADAPTIVE MESH REFINEMENT HYDRODYNAMICAL SIMULATION OF ETA CARINAE'S COLLIDING STELLAR WINDS AROUND PERIASTRON

A Thesis

Presented to

The Faculty of the Department of Physics and Astronomy

San José State University

In Partial Fulfillment

of the Requirements for the Degree

Master of Science

by

Trung Peter Ho

May 2020

The Designated Thesis Committee Approves the Thesis Titled

A THREE DIMENSIONAL ADAPTIVE MESH REFINEMENT
HYDRODYNAMICAL SIMULATION OF ETA CARINAE'S COLLIDING
STELLAR WINDS AROUND PERIASTRON

by

Trung Peter Ho

APPROVED FOR THE DEPARTMENT OF PHYSICS AND ASTRONOMY

SAN JOSÉ STATE UNIVERSITY

May 2020

Dr. Thomas Madura   Department of Physics and Astronomy

Dr. Patrick Hamill   Department of Physics and Astronomy

Dr. Aaron Romanowsky   Department of Physics and Astronomy

ABSTRACT

A THREE DIMENSIONAL ADAPTIVE MESH REFINEMENT
HYDRODYNAMICAL SIMULATION OF ETA CARINAE'S COLLIDING
STELLAR WINDS AROUND PERIASTRON

by Trung Peter Ho

One of the most luminous and mysterious binary star systems, classified as a
Luminous Blue Variable (LBV), is known to astronomers as Eta Carinae (η Car).
Located 7,500 light years away, this system holds a combined mass upwards of
$\sim 120 \, \mathrm{M}_\odot$ and a total luminosity of over $5 \times 10^6 \, \mathrm{L}_\odot$, making η Car a unique
astrophysical laboratory. The incredible mass loss of this system is due to powerful
radiation-driven stellar winds propelled by η Car's enormous luminosity. In this
thesis, the time-dependent, three-dimensional (3D) grid-based adaptive mesh
refinement (AMR) hydrodynamics code `RAMSES` is used to simulate the η Car binary
and its colliding stellar winds around periastron (closest approach). The results of
this simulation are presented as slices of density, temperature, and wind velocity
centered in the three major coordinate planes (xy, xz, and yz). The results show
that grid-based AMR codes will ultimately improve upon past simulations
performed with SPH methods. Furthermore, by comparing the simulation results to
observational data, the various orbital, stellar, and wind parameters of η Car can be
refined. The `RAMSES` simulation plots of density, temperature, and wind velocity are
of a significantly higher resolution than those of past SPH simulations and, to this
benefit, the higher resolution results show in detail the various instabilities (e.g.,
Kelvin-Helmholtz, thin shell) that arise at the colliding winds region and are
important for understanding X-ray observational studies. This simulation presents
the idea that grid-based AMR simulations can remain open for future refinement of
η Car's parameters, including an analysis at apastron, or furthest approach.

DEDICATION

To the many souls lost to the Coronavirus pandemic and racial injustice.

ACKNOWLEDGEMENTS

I am extremely grateful to Dr. Thomas Madura, for his support and guidance throughout this project. I have definitely enjoyed the hours spent talking while sharing the frustrations figuring out "simple" commands on a super computer together. It was his willingness to take me on that made this project and the collaborative friendship the highlight of my master's program.

Many thanks to Dr. Patrick Hamill and Dr. Aaron Romanowsky for participating on my committee, and with regards to ensuring timely progress to complete this work. I appreciate the time Dr. Hamill has spent with ongoing research discussions among other students, and Dr. Romanowsky for the guidance with Python inspired diagrams.

A special thanks to Dr. Neil Switz, for his spontaneous and thoughtful advice as we spoke typically in the hallway. Although our conversations were short, much of his advice has given me the tools to approach the challenges from taking classes and to starting this thesis.

Many thanks to Marilyn Booye, who has opened an opportunity to allow me to begin this program and ultimately this work, and acknowledging the assistance of Linh Pham, for helping me understand the small calculations.

Lastly, an appreciation my parents "Momma" and "B´ô", brothers Paul and Perry, and sisters Lien and Aimee for their support. And most of all to my wife "Tú", for all the endearing support and the absolute patience for the years I have focused my attention towards my education throughout the failures and successes.

TABLE OF CONTENTS

CHAPTER

LIST OF TABLES

Table

LIST OF FIGURES

Figure

xiii

CHAPTER 1
INTRODUCTION

1.1   Eta Carinae

Eta Carinae (η Car) is a unique and luminous binary star system that has been closely studied observationally and theoretically for the past $\sim$175 years (Humphreys & Davidson 1984; Davidson & Humphreys 1997; Humphreys & Davidson 1999; Smith & Frew 2011; Damineli et al. 2019). Located approximately 7,500 light years away in our Galaxy (Smith 2012), η Car's estimated total mass is >120 times the mass of the Sun ($M_\odot$); $\sim$90 $M_\odot$ for the primary star and $\sim$40 $M_\odot$ for the secondary (Hamaguchi et al. 2018). The binary orbit is highly elliptical with an eccentricity of 0.9 and an orbital period of 2024 days (5.54 years; Corcoran et al. 2017). The estimated luminosity of η Car is 5×10^6 times that of the Sun ($L_\odot$; Davidson & Humphreys 1997). Due to their extreme luminosities, the stars in η Car possess stellar wind mass outflows that reach speeds of 420 km/s (primary star) and 3000 km/s (secondary star; Madura et al. 2013). Radiation pressure is the driving force behind these outflows, leading to tremendous stellar mass loss at rates of $\sim 8.5 \times 10^{-4}$ $M_\odot$ yr^{-1} (primary) and $\sim 1.4 \times 10^{-5}$ $M_\odot$ yr^{-1} (secondary; Madura et al. 2013). For context, the overall rate of mass loss from our Sun is only $\sim 10^{-14}$ $M_\odot$ yr^{-1}. The powerful stellar winds in η Car collide between the stars, forming a wind-wind-collision (WWC) shock zone that is responsible for complex time-varying spectroscopic and photometric variability observed across a wide range of wavelengths from the radio to gamma rays. There is great interest in understanding the physical processes that lead to this observed multi-wavelength variability (Damineli et al. 2019), since such an understanding provides us with relevant information about the late-stage evolution of nearby extremely massive

stars and supernova progenitors. Three-dimensional (3D) numerical simulations of η Car's binary system and colliding stellar winds provide one important way of studying the system. Comparison of results from numerical models to direct observations reveals important details about the binary's orbital motion, photoionization properties, and recent (5 to 15 year) mass loss history. Such an analysis also provides a baseline for following future changes in η Car as the stars approach the ends of their lives.

Study of η Car began in the 1600s, but interest in η Car did not really take off until η Car's "Great Eruption" in the 1840s when the system suddenly became the second brightest non-solar-system object in the sky (Humphreys & Davidson 1999; Damineli et al. 2019). The mass loss at this time is measured to be at least 10 $M_\odot$, perhaps as much as 40 $M_\odot$, over a period of $\sim$10 years. This eruption is responsible for forming the spectacular bipolar "Homunculus" nebula that now surrounds the stars (Smith 2012). The Homunculus presents a challenge for observing the central η Car binary, as the nebula obscures any direct observation and contributes a blanket of additional spectral emission and absorption lines. The Homunculus nebula remains a target of detailed observational studies by instruments like the Hubble Space Telescope (HST) since many of the nebula's properties and its formation history are still not well understood (Smith 2012). Some early studies, such as (Van Genderen 1984), outline interpretations of the nebula's structure and photometric variability. Recent studies like (Smith 2012) and (Steffen et al. 2014) outline the structure of the Homunculus. Our current understanding of the structure of the Homunculus is that it is bi-lobed, with an equatorial disk at the center, and measures approximately one light year in length from pole to pole. Meanwhile, dust and molecules form in the walls of the nebula as the material within expands and cools as it moves farther away from the central stars.

While the surrounding Homunculus nebula provides some clues on the nature of the inner binary system, such as the chemical composition and evolutionary status, there are still questions that have not been answered about the individual massive stars, and massive stars in general. The origin and mechanisms behind its many large eruptions, the exact masses of the individual stars, and the spectral type of the secondary star are a few of the many remaining questions associated with η Car. η Car also provides a unique nearby astrophysical laboratory for studying extremely massive stars similar to those that existed in the early universe, which are thought to have been very massive (Smith 2012). Ultimately, the big remaining questions in astronomy that studying η Car can help answer are "What determines the ultimate fate of massive stars, e.g. how do massive stars end their lives?," "How does mass-loss, via stellar winds and giant mass eruptions, affect massive star evolution?," "How did the first stars form, lose mass, evolve, and affect later generations of stars?," and "How are the heavy elements, dust, and molecules that form in massive stars and their deaths ejected and redistributed throughout galaxies, and how does this affect galaxy evolution?".

1.2   Modeling Stellar Winds

Classification of the primary component of η Car as a Luminous Blue Variable (LBV) sets the foundation for the development of showing the relationship between a star's brightness and mass as established in (Humphreys & Davidson 1984). As Luminous Blue Variables are considered to be a class of stars that are hot, massive, and luminous by having extreme photometric and spectroscoptic variability (Vink 2012). They are luminous hot stars that some times erupt or end in an outburts with an large mass loss. This is where η Car earns the title of LBV with evidence from the first Great Eruption of 1840.

With such variability among massive stars there is an instability limit where sudden outbursts are driven by luminosity. This comes as the additional classification called the Humphreys-Davidson limit (HDL; Glatzel & Kiriakidis 1993). Stars that exist beyond the HD limit are likely to be unstable resulting in significant mass loss. Examples of these cases that are in the Milky Way are P Cygni and η Car that are high luminosity stars (Humphreys 2019). While the HD limit is an empirically determined limit, it helps determine how massive stars around this limit lose significant mass. Understanding η Car's mass loss helps draw a clear picture on how stars near the HD limit losss mass. Establishing the HD Limit begins with the mapping of main sequence stars on a Hertzsprung-Russell Diagram (HR-Diagram). Among this mapping are stars rich with hydrogen fuel that stabilizes the life cycle of a star. Luminosity helps drive mass loss but are in hydrostatic equilibrium, creating more stable stars along the main sequence. The HR Diagram is representative of stellar evolution as the correlation between mass, temperature, and luminosity outline the life cycle of a star. In contrast the extreme luminosity and mass of η Car places it in a unique region of the upper HR Diagram, then pushing beyond the HD Limit. Exceeding proposed mass limits in (Humphreys & Davidson 1984) sets η Car to be a carefully studied stellar object. Luminosity becomes the driving force for stellar winds.

For hot and massive stars, radiation pressure as a result of the star's extreme luminosity sets a defining limit within the HD Limit known as the Eddington Limit. Exceeding this Eddington Limit then gives meaning to stellar wind conditions and the physics of radiation driven stellar winds (Cranmer 1996). Some characteristics of stellar winds, such as mass loss rate and wind speed, are determined from theoretical modeling and analytical methods. These conditions for stellar wind mass loss follow a velocity limit based on thermodynamic principles (Owocki 2005).

Density from mass loss rate and velocity follows from an analytical method of colliding winds. Temperature follows from an understanding of cooling processes (optically-thin radiative cooling vs. adiabatic cooling) in the winds and post-shock colliding wind material (Stevens et al. 1992).

By determining these characteristics with modeling stellar wind conditions, and by applying the parameters of η Car's orbit the aim is to understand intrinsic properties of interaction in this system. For example, what are the velocity magnitudes in wind speeds further away from the bow shock front? At what point does temperature in ejecting wind switch from adiabatic to radiative? A question related to temperature that is still unknown in the study of η Car is the spectral emissions from hot shocked gas following a wind collision. Most importantly, current observations are now examining this emission on the X-ray spectrum as described by (Corcoran et al. 2017) and (Damineli et al. 2019).

Other than modeling winds are determining the general composition of η Car. Massive stars such as η Car are considered to be of Wolf-Rayet (WR) type or early type O and type B, where hydrogen that is the main source of fuel becomes depleted. Instead, nuclear reaction involving Carbon (C), Nitrogen (N), and Oxygen (O) are used as fuel in a Carbon-Nitrogen-Oxygen (CNO Cycle) environment (Davidson & Humphreys 1997). These are other leads that potentially have the opportunity to modeling.

1.3   Colliding Wind Simulations

Properly simulating the binary colliding winds of η Car requires a full 3D time-dependent computational approach. Hydrodynamical simulations using the grid-based code with adaptive mesh refinement (AMR), while computationally expensive, are now possible. This numerical method is used widely among the

astronomy community in running simulations of galaxy formation, and including the simulation of colliding winds as seen in (Calderón et al. 2020). Characteristics from past work and observations within η Car are applied in this numerical code, see (Madura 2010) and (Madura et al. 2013) for past work, and (Corcoran et al. 2017; Damineli et al. 2019; Hamaguchi et al. 2018) for examples of observations that set the simulation parameters.

By extrapolating the results from an AMR simulation, a 3D model is constructed to further investigate the properties of η Car's colliding wind binary. While constructing this model, the output is then plotted through visual modules with the use of Python programming. The generated plots represent density, temperature, and wind velocity with parameters at η Car periastron approach. This is made possible by applying initial conditions based on past observational data, and early modeling approaches using Smooth Particle Hydrodynamics code (SPH). Applications of 3D modeling provides further insight some of the most interesting properties within the colliding wind shock zone to the Homunculus nebula. In particular, of these properties are energy emitted in the colliding wind shock zone where emission can reach X-ray wavelengths (Hamaguchi et al. 2018). Mass-loss, being a result of radiation pressure effects the type of radiation emitted during periastron passage as the wind speeds switches from adiabatic to radiative cooling, also plays a role in modeling stellar winds.

Modeling mass-loss rates with density, temperature, and wind velocity not only allows for comparisons with observational data, but is not limited to comparisons with past modeling methods. As mentioned, past simulations performed η Car colliding winds made use of SPH code on small domains and lower resolution (Madura et al. 2013). While current AMR grid-based simulations make use of RAMSES code are compiled at higher resolutions and larger domains. Well

defined plots are made possible through the use of Python programming and YT visualization modules. Concluding this thesis, is a presentation on 3D planar slice plots (where $x = 0$, $y = 0$, and $z = 0$) show a more intricate detail the colliding winds of η Car. At larger domains and high resolution presented are improvements in defined points of fluid instability, an opening shock angle, wind temperature differences, and a broader estimation for terminal velocity.

CHAPTER 2
HISTORICAL ERUPTIONS

Study of the unique features of η Car spans over four hundred years, starting in the 1600s (Humphreys & Davidson 2012), during which time came the first observations made by early astronomers, who were able to observe and determine visual apparent magnitudes. Around 1842, an eruption known as "The Great Eruption" occurred when the peak apparent magnitude reached about -1. (Smith 2012) suggests that the surrounding "Homonculus" nebula formed from this spectacular event. Following the Great Eruption, the system dimmed before brightening again in 1900, when a "Lesser Eruption" occurred, producing the "Little Homunculus" nebula that sits within the larger Homunculus (Smith 2012). Around this time, new observational tools were being developed which would allow future detailed spectral and photometric studies. In this chapter, we discuss the key properties of η Car and some highlights from observational studies of the system throughout history. Lastly, we establish the classification of η Car as a LBV star via its observed variability across multiple wavelengths.

2.1 The Great Eruption

The first modern recorded observations of η Car occur near the year 1600 (Davidson & Humphreys 1997). From then until the 1830s, η Car was observed as a second or fourth apparent magnitude star. As demonstrated in Figure 2.1, η Car was not a very interesting object until 1843, so very little is known about the object prior to then. Further discussions on observational studies in the 1600s, 1700s, and early 1800s are left to the reader (see e.g. Humphreys & Martin 2012), while other historical facts can be found in (Humphreys & Davidson 2012). The apparent visual
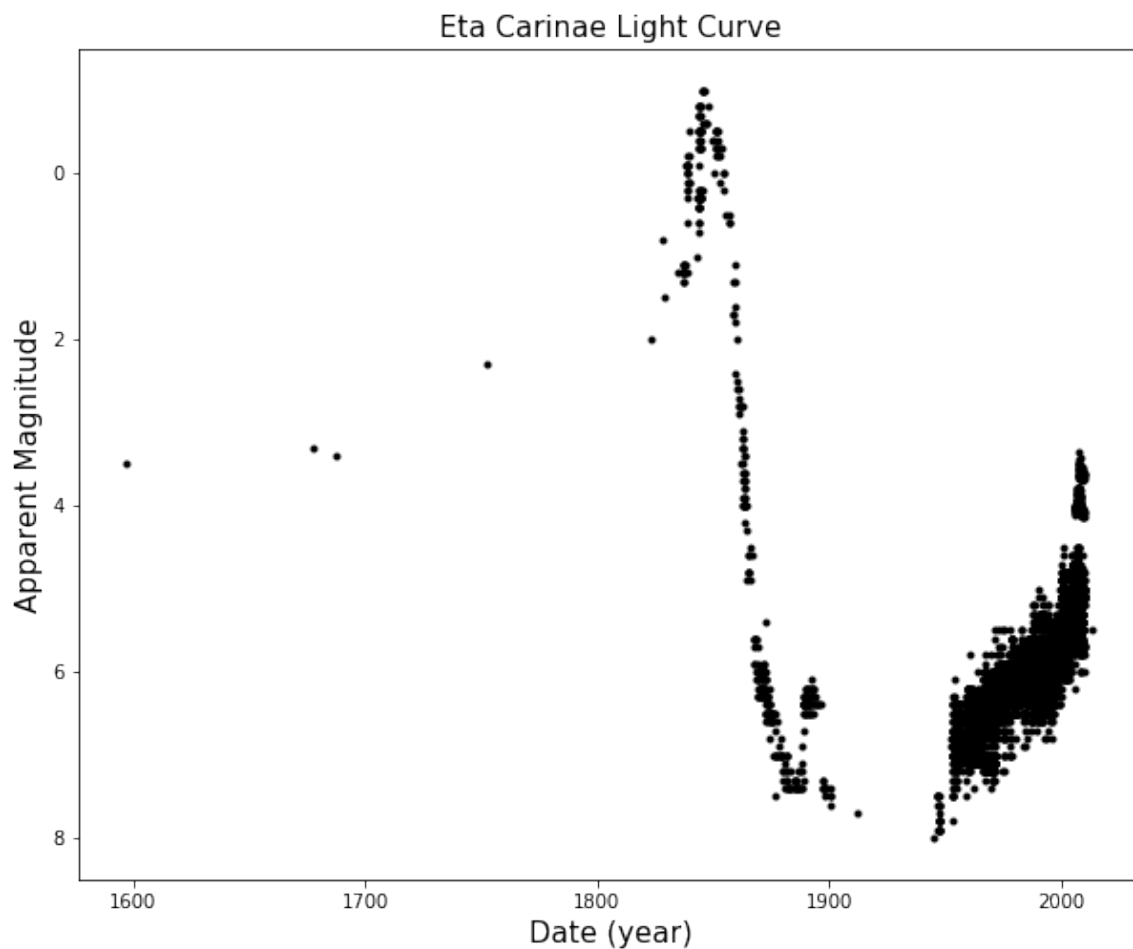
Figure 2.1: The historical light curve of η Car with apparent visual magnitude between the years 1600 and 2010. Key features of this light curve are peak brightness occurs at 1840 during "The Great Eruption" declining until 1900 where a sharp rise occurs during a "Lesser Eruption". Additional verified observations begin to take place after 1930 as brightness begins to move upwards towards magnitude 4. Data provided by the American Associate of Variable Star Observer (AAVSO) database on η Car, www.aavso.org.

magnitude of η Car is thought to have been between 2 and 4 up until the 1830s, before the Great Eruption occurred (Humphreys & Davidson 1999).

The years between 1830 and 1850 are a significant time period for η Car. This spectacular event where mass loss was perhaps up to 40 $M_\odot$ is known as the "Great Eruption." During this time, around the year 1843, η Car reaches its peak apparent visual brightness, ~ -1 (Davidson & Humphreys 1997). Figure 2.1 shows the historical light curve before, during, and following this event. After 1856, η Car faded and temporarily stabilized to seventh or eighth magnitude around the year 1870. (Humphreys & Davidson 1999) believe that this apparent magnitude decrease is due to absorption of light by surrounding, newly formed and ejected dust from the Great Eruption.

Between 1887 and 1895, a second brightening event and eruption occurred, although much smaller than the Great Eruption. During this time η Car brightened to about sixth magnitude, ejected about 0.1 $M_\odot$ of material, and formed the "Little Homunculus" nebula (Smith 2012). After this, the system dimmed and stabilized to nearly eighth magnitude around the year 1900. η Car's brightness was then relatively stable up until the 1950's, when it started to gradually brighten. Over the last $\sim$ 70 years, η Car's brightness has increased by nearly four magnitudes, and current observations place the system at an apparent magnitude of about 4, the brightest the system has been since just before and during the Great Eruption.

The luminosity of η Car during the Great Eruption is estimated to be on the order of $10^{7.3}$ $L_\odot$. The causes of the Great Eruption and lesser eruption of the 1890s are still unknown, although recently detected "light echoes" are helping to provide some new insights. By understanding the reflection of spectral absorption lines from nearby dust, (Rest et al. 2012) was able to confirm estimates of mass ejection speeds, mass loss, and temperature arising from the Great Eruption.

2.2   The Homunculus Nebula

A unique and grand feature that was a direct result of the Great Eruption is the surrounding Homunculus nebula, primarily made of dust formed from material ejected during the Great Eruption (Humphreys & Davidson 2012). Visually the Homunculus is described by its bipolar lobes and an equatorial skirt. Figure 2.2 shows a detailed image of the Homunculus taken by the Hubble Space Telescope (HST) in July 2019. Determining the size and mass density begin with early estimates measuring the total mass of the Homunculus were to be about 2-3 $M_\odot$ (Davidson & Humphreys 1997). While on more recent estimates indicate a total mass of $\sim$20 $M_\odot$ (Smith 2012) based on a gas-to-dust ratio of 100. Following this with near-infrared observations, a mass estimation of the same gas-to-dust ratio shows total mass of more than 45 $M_\odot$, (Morris et al. 2017). In the same study is the composition that makes up the Homunculus nebula. Primarily the composition of the Homunculus is composed of nitrogen (N) while deficient in carbon (C) and oxygen (O). This suggests that the main fuel in this system has made the transition from the CNO cycle to burning helium (He) as fuel making the Homunculus nebula is a prime candidate for infrared (IR) observations.

The central binary in the Homunculus plays a role in influencing the shape and overall structure (Steffen et al. 2014). Modeling and infrared spectroscopy allows for observations of Homunculus expansion and a precise 3D structure to be mapped. This sets some boundaries as the kinetic energy of the Homunuculus is estimated. The results in (Steffen et al. 2014) show that with the influence of the central binary, the general structure of the Homunculus having: (1) circumpolar trenches in each lobe positioned point symmetrically from the center and (2) off-planar protusions in the equatorial region from each lobe at longitutinal ($\sim 55°$) and latitudinal ($10° - 20°$) distances from the projected apastron direction of the

binary orbit. In addition, the angular distance between the protrustions ($\sim 110°$) is simular to the angular extent of each polar trench ($\sim 130°$) and near equal to the opening angle of the wind-wind collision cavity ($\sim 110°$).

Another important feature is the total kinetic energy of the expansion in the Homunculus nebula, (Smith et al. 2018). Observations show that ejected mass reaches up to -10,000 km s^{-1} on the near side of the nebula and up to +20,000 km s^{-1} on the far side. This gives an estimate for total mass loss during the great eruption, but also gives an estimate for total initial mass of the central binary with the upper limits of $\sim 150\,M_\odot$. In an independent analysis of Near-IR of the Homunculus, (Smith 2012) shows that an implied ejected mass of $> 10 M_\odot$ as a result from the great eruption has kinetic energy in the range of $10^{49.6} - 10^{50}$ erg.

Understanding the features of the Homunculus and the great eruption of 1840 help astronomers find clues to the evolutionary states of massive stars. Massive eruptions also give clues on how massive stars reach supernova attaining their ultimate fate. A particularly long-standing mystery in the life cycle stars can be interpreted by studying the Homunculus and the central binary itself. Current models of the Homunculus rely on certain assumptions such as the accretion from the secondary star (Steffen et al. 2014). Modeling the Homunculus requires hydrodynamical simulations to investigate the overall stucture.

2.3   Photometry and Spectrophotometry

Modern spectroscopic and photometric methods paved a way for serious inquiry into η Car the later half of the 20th century. Interest in η Car becomes apparent as methods of observation begin to advance starting in the 1960s (Davidson & Humphreys 1997; Humphreys & Martin 2012). However, despite numerous intricate studies with modern tools, η Car remains not well understood.

Figure 2.2: A detailed photograph taken by Hubble Space Telescope using Hubble's Wide Field 3. The image is then mapped to the ultraviolet-light glow of magnesium that is within the gas. Shown here is the homunculus nebula surrounding a luminous center. A unique characteristic is the bipolar lobes with and equatorial skirt at the center. Credits: NASA, ESA, N. Smith (University of Arizona) and J. Morse (BoldlyGo Institute)

Multi-wavelength observational studies helped determine η Car's spectral distribution over radio, infrared (IR), optical, ultraviolet (UV), X-ray, and gamma-ray wavelengths. In early studies, η Car was originally thought to be a single massive star radiating in the UV. Later it was understood that η Car's central binary emits optical and UV radiation, but this radiation is absorbed and re-emitted in the IR by the Homunculus nebula. X-ray observations in the late 1990s confirmed the presence of a central binary system, with the X-ray emission arising from the shock-heated gas at the interface where the two stellar winds collide. X-rays are not as attenuated by the Homunculus nebula, providing important diagnostics on the properties of the colliding winds and central binary, such as the shock temperature, wind terminal speeds, orbital eccentricity, and periodicity.

In combination with the total system luminosity obtained from studies of the Homunculus nebula, spectroscopic observations of η Car indicate a total system mass $\gtrsim$120 M$_\odot$. Modeling of HST spectroscopic observations also places tight limits on the mass loss rate and wind speed of the primary star, as well as limits on the mass and luminosity of the secondary star. Spectroscopic studies also provide essential information on the temperature structure of the stellar winds and colliding winds region. The amounts and distribution of H, He, C, N, O, and other heavy elements help in determining the likely evolutionary stage of the star. Understanding the distribution and abundances of elements can lead to a better understanding of how future stars are formed. Whether or not η Car has exhausted its main H fuel source is not known. There is some justification for classifying η Car's secondary star as a post-main-sequence Wolf-Rayet (WR) star given its unusually high mass loss rate, wind speed, and temperature. This would further suggest that η Car may be nearing the end of its life and supernova explosion. However, this is not well understood.

2.4   Eta Carinae as a Luminous Blue Variable

Classifying stars as LBVs has been a research topic of interest for astronomers starting as early as the 1970s. The basic property of a star classified as an LBV is considerable variations in its spectra and photometry, (Vink 2012). LBVs are also known for exhibiting bursts of extreme mass loss, such as η Car's Great Eruption. Variability is measured on a time span of years. Other considerations for classifying η Car as an LBV include stellar luminosity and temperature. As luminosity scales roughly with mass as $M^{3.5}$, η Car's primary star mass of ~ 90 M$_\odot$ implies a luminosity of nearly seven million L$_\odot$. In reality, the star is not quite this luminous since the power-law dependence on mass flattens out as the star approaches the Eddington Limit. Still, current estimates place the primary star's luminosty at $\gtrsim 4 \times 10^6$ L$_\odot$. In terms of temperature, the "surface" of the primary star likely has a temperaure near 35,000 K. However, because the primary is so luminous and has such a dense, optically thick stellar wind, we are unable to directly observe the surface of the star. Instead, we are only able to peer down to an optical depth of $\sim 2/3$ at any particular wavelength, resulting in a spatially-extended "wind photosphere" that has a radius of ~ 880 R$_\odot$ and temperature of ~ 9000 K. Photoionization and spectral modeling of ejecta near the stars places limits on the secondary star's luminosity and temperature of $\sim 10^6$ M$_\odot$ and 40,000 K.

Large variations in the luminosity of η Car can affect its stability. Observational limits on stability are available via Hurtzsprung-Russell diagrams, discussed in detail later in this thesis. η Car famously exceeded a luminosity to mass limit known as the Eddington Limit, wherein the star becomes so luminous it effectively becomes gravitaionally unbound. However, in addition to such large variations in luminosity, the stars in η Car are bright enough to exhibit continuous mass loss via radiation-driven stellar winds. Any proper numerical simulation of the

η Car binary must account for such mass loss. This necessitates a proper discussion of the physics of mass loss from massive stars (Owocki & Shaviv 2012), leading to an eventual discussion of such mass loss in massive binary systems and the colliding wind binary (CWB) phenomenon.

CHAPTER 3
MASS LOSS FROM MASSIVE STARS

The ultimate fate of η Car depends on its mass loss. The Great Eruption, producing at least 0.1 M$_\odot$ in mass loss per year, is an extraordinarily high rate of mass loss. In fact, this is the largest non-terminal stellar mass loss rate currently known (non-terminal meaning that the star survived the mass loss and did not go supernova or form a compact object). In this chapter we summarize some key aspects of mass loss from massive stars that is due to radiation pressure. Futhermore, we establish η Car as a LBV. By classifying η Car as a massive star and LBV, we can show that the properties observed can be modeled by extension of the HR Diagram. By extension, we will show that η Car approaches the Humphreys-Davidson limit. The Humphreys-Davidson limit describes the stability of massive stars given their luminosity. Beyond these limits, a star's radiation pressure can overcome gravity, making the star inherently unstable.

3.1 Hurtzsprung-Russell Diagram

The Hurtzprung-Russell Diagram (HRD) model is applied in the determination of star classification. Based upon evolutionary stages of a star's life cycle, the HRD provides a foundation for understanding the stability of stars (Glatzel & Kiriakidis 1993). Fundamentally, the HR diagram provides insights on some global characteristics of a star (Carroll & Ostlie 2014). The key parameters required to construct an HR Diagram are stellar luminosity and temperature, where luminosity implies stellar mass. Observationally-determined HR diagrams use absolute magnitude as a proxy for luminosity and color as a proxy for effective temperature. Plotting absolute magnitude versus color for a large number of
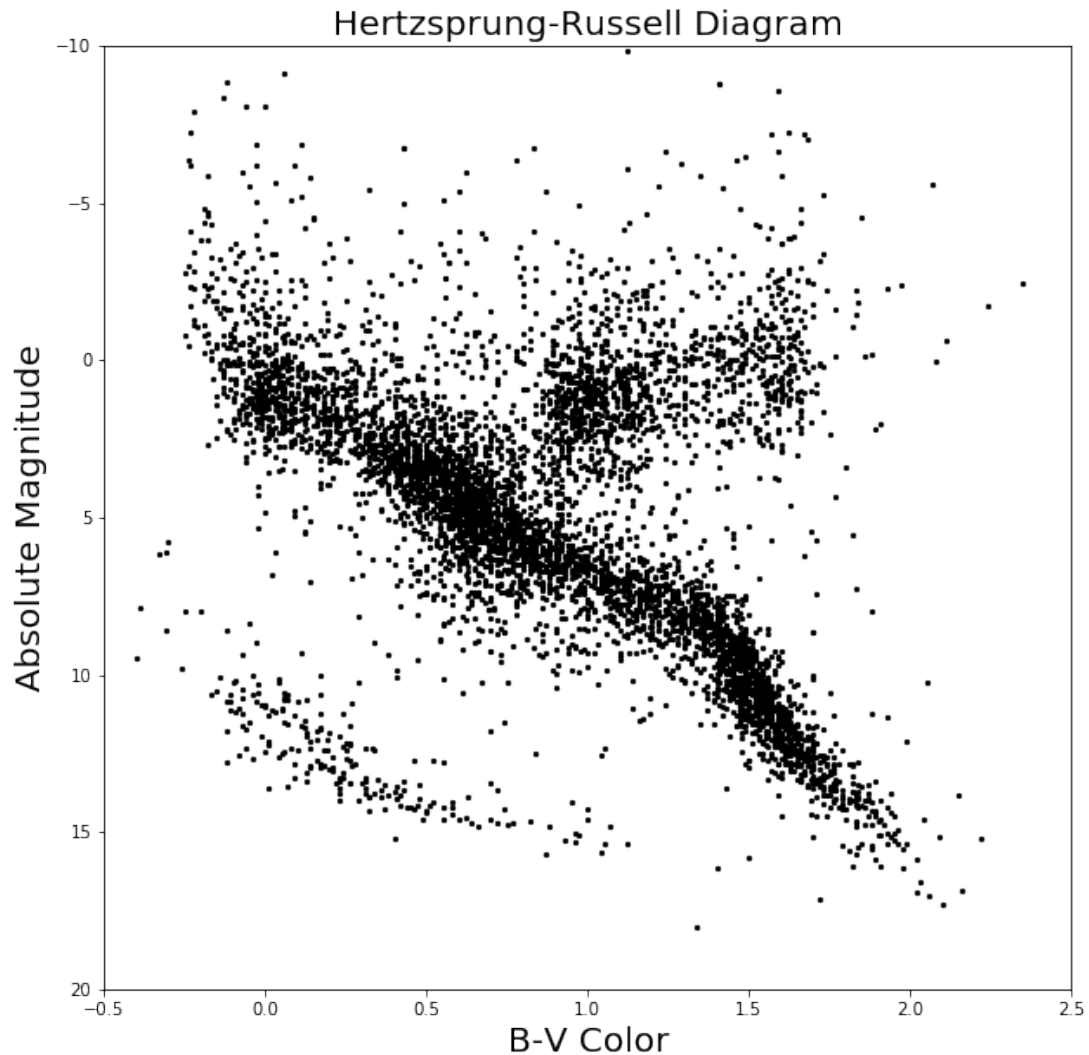
Figure 3.1: A Python generated plot of the Hurtzsprung-Russell Diagram based on observational data provided by the Yale Trigonometic Parallax Dataset (van Altena et al. 1995). The horizontal axis represents the B-C color index and the vertical axis absolute magnitude. The diagonal grouping of stars through the middle of the plot represents stars on the main sequence. More massive, hotter and bluer stars trend towards the upper left hand corner, while smaller, cooler and redder stars trend towards the lower right. The upper right hand side represents the evolved red giants, while to the lower leftmost portion of the plot are the smaller and less luminous white dwarfs, the remnants of dead Sun-like stars.

observed stars then produces an HR diagram, as demonstrated in Figure 3.1. The large grouping of stars running through the middle of the diagram is known as the "main sequence" and indicates where stars spend the majority of their lives as they burn through their nuclear fuel and remain in hydrostatic equilibrium. More massive and bluer stars are located to the upper left on the main sequence, while lower mass, redder stars are located to the lower right on the main sequence. Indicators such as the placement of white dwarfs on the lower left hand corner and super red giants on the upper right show that evolved outlier stars do not fall within the main sequence. The HR diagram thus provides a snapshot of stellar evolution across a wide range of stellar masses.

3.2   Humphreys-Davidson Limit

Further classifying LBVs would require an extension to the HR-Diagram at the upper limits for massive stars. LBVs exceeding the mass and luminosity limits are distributed based on an effective temperature scale towards the left in the HRD, compared to supergiants that exist in the upper right region of the HRD. LBVs are observed to be at lower temperatures in comparison to supergiants existing at much higher temperatures. The empirical limit for the stability of massive stars indicated in 3.2 by a solid line is the point at which the luminosity implies stellar mass loss. This empirical limit is based on the Eddington Limit that describes the outward radiation force overcoming gravitational inward forces (Glatzel & Kiriakidis 1993). Exceeding the Eddington Limit produces outward pressure that can drive extreme stellar mass loss.

3.3   Stellar Opacity of Massive Stars

Photons moving through a dense medium are likely to be absorbed and scattered, thus resulting in an overall lower intensity. The depletion of photons via

Humphreys-Davidson Limit

η Car

P Cyg

$100 M_\odot$

$80 M_\odot$

$60 M_\odot$

$40 M_\odot$

$30 M_\odot$

$20 M_\odot$

Bolometric Magnitude

Spectral Type

-12

-11

-10

-9

-8

-7

-6

Hertzsprung-Russell Diagram

Absolute Magnitude

B-V Color
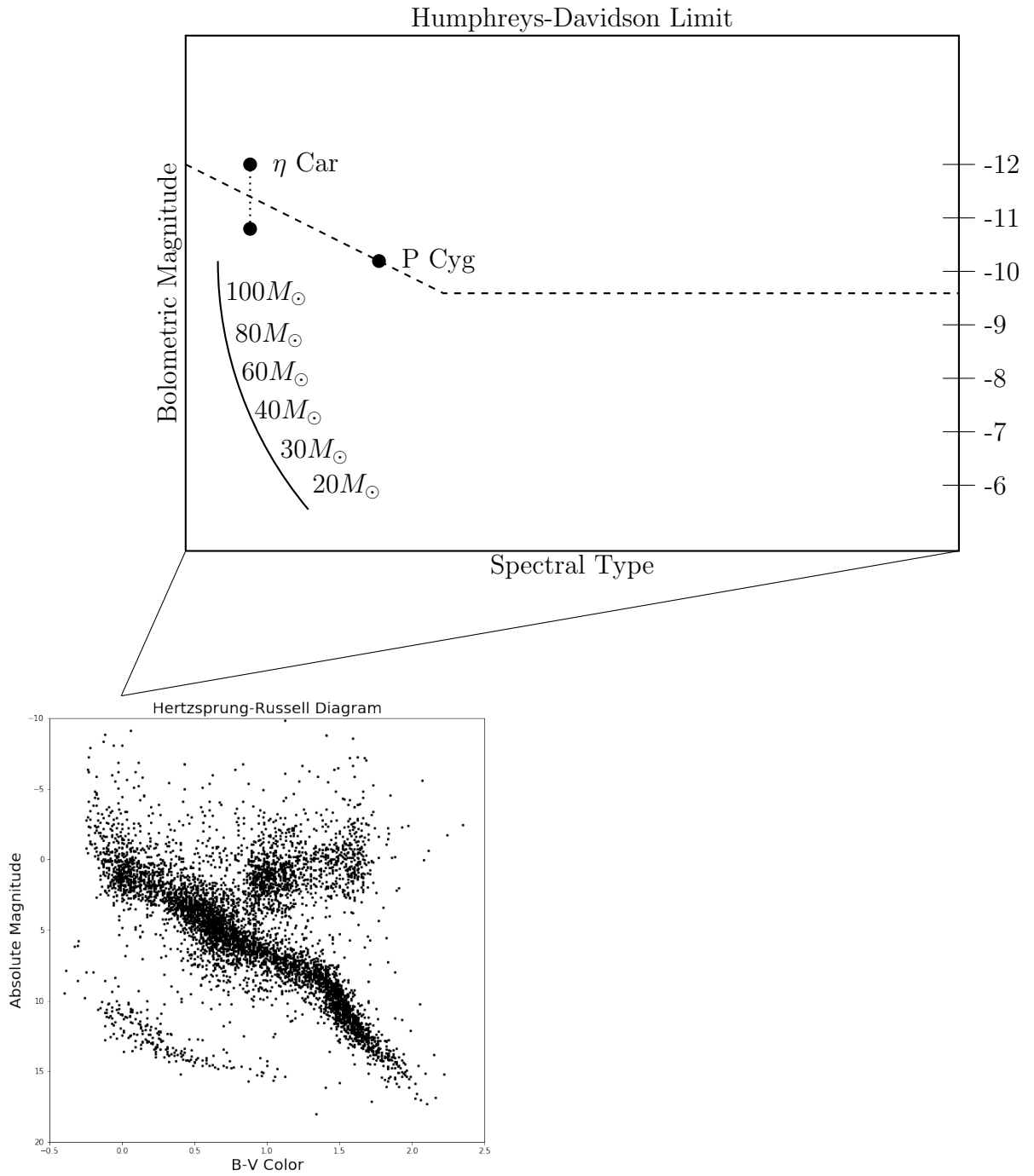
Figure 3.2: Extending the HR diagram in the upper limits is the Humphreys-Davidson limit. Beyond this limit stars become unstable as luminosity creates mass loss from radiation pressure.

scattering and absorption in stellar atmospheres is characterized by the opacity κ. Opacity can be better understood by imagining a cylindrical beam of light moving through a gas. In this beam the total absorption from photon scattering and absorption by electron transitions contributes to the total opacity (Carroll & Ostlie 2014). For stellar atmospheres, opacity is comprised of several absorption factors that arise as a result of multiple microscopic processes that depend on the physical properties and composition of the absorbing medium. It is the cross section for the absorption of photons having wavelength λ per unit mass of stellar material. More generally, the opacity of a gas is a function of its composition, density, and temperature.

For a light beam propagating through a gas the intensity I is proportional to opacity κ, density of gas ρ, and the distance, s, that the beam traverses

$$I \propto \kappa \rho s. \tag{3.1}$$

This gives the units of opacity as $m^2 kg^{-1}$. Dependent on the wavelength of the light, λ, the change in intensity dI_λ over a distance ds can be expressed as

$$dI_\lambda = -\kappa_\lambda I_\lambda \, \rho \, ds. \tag{3.2}$$

Opacity is the coefficient of intensity dependent on wavelength. The intensity decreases the further a light beam propagates through the gas.

Individual sources of opacity can contribute to the total continuum of opacity. With total opacity being comprised of its constituents, which can include bound-bound transitions, bound-free absorption, free-free absorption, and electron scattering. In a descriptive reference by (Carroll & Ostlie 2014), pages 276-281, and by the order of each description as referenced in the text, the constituent parts of opacity may include:

- **Bound-Bound Transitions** ($\kappa_{\lambda,\mathbf{bb}}$) or the transition of electrons from one bound energy state to another. Occurs when an incident photon is absorbed by an electron bound to an atom. The absorption of a photon transitions an electron to a higher energy state while the re-emission of a photon transitions an electron down to a lower energy state. Both transitions are taking place at once in stellar atmospheres and occur only at the specific wavelength of the transition in question.

- **Bound-Free Absorption** ($\kappa_{\lambda,\mathbf{bf}}$) or photoionization, is the effect of incident photons ejecting electrons from their bound state in an atom. This effect ionizes atoms, given a photon has enough incident energy. In contrast, ionized atoms can also capture electrons in a reverse ionization process, thus resulting in the emitting of a photon of a specific wavelength.

- **Free-Free Absorption** ($\kappa_{\lambda,\mathbf{ff}}$) occurs when a free electron near an ion absorbs a photon. Because a free electron cannot absorb a photon due to momentum and energy conservation, and by the same principles an electron will increase in its speed or total momentum in conservation of energy with an incident photon. The reverse process can occur when a free electron approaches an ion causing a "braking radiation" where there is the emission of a photon when an electron slows down. This mechanism occurs for a continuous range of wavelengths, thus free-free absorption is a contributor to the continuum opacity.

- **Electron Scattering**($\kappa_{\lambda,\mathbf{es}}$) occurs when there is interaction between an incident photon and a free electron. A free electron cannot absorb a photon, but rather will deviate from its path trajectory through a transfer of momentum and energy. The two types of scattering of this type are

Thomson and Compton scattering where Thomson scattering is an incident photon to an electron will re-emit a photon at the same wavelength. Photons incident with a certain wavelength by contrast to Thomson scattering will be re-emitted at a different wavelength for Compton scattering.

Electron scattering is the most abundant and dominant form of opacity in the atmospheres and winds of hot, massive stars whose effective temperatures can range from 15,000 K to upwards of 50,000 K. At such temperatures, hydrogen is easily fully ionized. This and partial ionization of other heavy elements creates an abundance of free electrons, leading to an increasing electron density. Photons are more likely to interact through Thomson and Compton scattering as the cross section for an electron is much smaller than a hydrogen nucleus. The cross sectional area for an electron via Thomson scattering is

$$\sigma_T = \frac{1}{6\pi\epsilon_0^2}\left(\frac{e^2}{m_e c^2}\right) = 6.65 \times 10^{-29} \text{ m}^2 \ , \tag{3.3}$$

meaning that the cross section is much smaller, up to a billion times smaller, than a hydrogen nucleus.

Considering that the total opacity reduces the overall luminosity of a massive star, the effective luminosity then depends on the various contributions of opacity, which requires understanding the compositional, density, and temperature structure of the star's atmosphere. The wavelength dependent total opacity is

$$\kappa_\lambda = \kappa_{\lambda,\mathbf{bb}} + \kappa_{\lambda,\mathbf{bf}} + \kappa_{\lambda,\mathbf{ff}} + \kappa_{\lambda,\mathbf{es}} \ . \tag{3.4}$$

For the high temperatures of massive stars, the dominant source of opacity will be electron scattering, so this expression can be approximated as

$$\kappa_\lambda \approx \sigma_{\lambda,\mathbf{es}}. \tag{3.5}$$

However, electron scattering is a "gray" or wavelength independent form of scattering that affects all photons equally. One can thus further simplify the notation as $\kappa_\lambda \approx \kappa_e$ when discussing massive stars.

3.4   Exceeding the Eddington Limit

For a typical star, its stability depends on a state of hydrostatic equilibrium, which occurs when the outward radiation pressure matches the inward pull of gravity. The limit where the radiation pressure exceeds gravity is known as the Eddington Limit. Radiation pressure is driven by a star's total luminosity. Specifically, for hot, massive stars, radiation pressure is applied (Owocki & Shaviv 2012), as opposed to the pressure driven winds that occur in less massive stars. The Eddington Limit considers the ratio of stellar luminosity to mass. The great eruption of η Car shows the dramatic effects that can occur when the luminosity reaches its peak near/exceeding the Eddington Limit. The mass loss during the Great Eruption is the result of outward radiation pressure exceeding gravitational forces at this extreme.

When outward and inward forces are equivalent at hydrostatic equilibrium, the gradient of pressure P equals the gravitational force $F = \rho\mathbf{g}$, leading to

$$\nabla P - \rho\mathbf{g} = 0 \ . \tag{3.6}$$

Further discussions on radiative line acceleration and the detailed determination of stellar mass loss rates will be discussed in the following section (3.5). For simplicity, here we consider only the simple case of scattering by free electrons, which is a gray or wavelength-independent process. To determine the radiation pressure, we begin by considering the radiative energy flux from a spherically symmetric star

$$F_{\mathrm{rad}} = \frac{L}{A} \ , \tag{3.7}$$

where L is the total stellar luminosity and A the total surface area of a symmetric sphere. Since gray scattering cannot alter the star's total luminosity L, the radiative energy flux at any radius r is

$$F_{\text{rad}} = \frac{L}{4\pi r^2} \ , \tag{3.8}$$

corresponding to a radiative momentum flux of F_{rad}/c. However, there are factors that affect the total luminosity, one being the opacity κ_e. A unit of opacity per speed of light c is κ_e/c. Multiplying the radiative energy flux F_{rad} by κ_e/c gives us the radiative acceleration (force per unit mass) due to the opacity κ_e:

$$g_{\text{rad}} = \frac{(\kappa_e/c)L}{4\pi r^2} \ . \tag{3.9}$$

Division of g_{rad} by the gravitational acceleration $g_{\text{grav}} = GM/r^2$, where M is the mass of the star, leads to a ratio of accelerations g_{rad} to g_{grav}. The Eddington parameter Γ_e is defined as this ratio of the radiative acceleration to the gravitational acceleration

$$\Gamma_e \equiv \frac{\kappa_e L}{4\pi c G M} \ , \tag{3.10}$$

where G is the gravitational constant. This Eddington parameter has a characteristic value for each star. As the luminosity increases, radiative forces become more important. If $\Gamma_e > 1$, radiative acceleration exceeds gravitational acceleration, leading to stellar mass loss. Giant outbursts during η Car's great eruption period are a prime example of exceeding the Eddington limit.

For electron scattering in an ionized medium, the opacity is simply a constant, $\kappa_e = \sigma_e/\mu_e$, where σ_e is the classical Thompson cross-section (σ_T) and the mean atomic mass per free electron is

$$\mu_e = \frac{2m_H}{1+X} \ , \tag{3.11}$$

with m_H the mass of the hydrogen atom and X the mass fraction of hydrogen (typically $X = 0.72$ for solar abundances). Applying the value of the Thomson electron cross section given by equation 3.3, a simplified relation for computing the value of κ_e for a given mass fraction of hydrogen X is (Owocki & Shaviv 2012)

$$\kappa_e = \frac{\sigma_e}{\mu_e} = 0.2(1 + X) \text{ cm}^2/\text{g} \ , \tag{3.12}$$

which gives $\kappa_e \approx 0.34 \text{ cm}^2/\text{g}$, assuming $X = 0.72$.

For an Eddington parameter to exceed the value of one would imply a rather large value of luminosity compared to mass! For an LBV and η Car, sudden bursts in luminosity can cause the star to exceed the Eddington limit. This surpasses the limits of stability.

3.5   Radiation Driven Stellar Winds and Mass Loss Rate

For massive stars, radiation pressure becomes the dominant driving force for stellar winds, including the loss of stellar mass. This is in contrast to our Sun, which has a convective upper atmosphere and a solar wind driven by simple gas pressure. Radiation driven stellar winds have a long history of study. Early foundations described by (Lucy & Solomon 1970) outline an analytical approach to determining mass loss and mass loss rates of massive stars. Afterward, the theory evolved into the modern theory of line-driven stellar winds, otherwise referred to as CAK Theory, as described in (Castor et al. 1975). Current understanding of line-driven winds is extended to multi-line scattering and instabilities, as described by (Owocki 2005). Without exhausting on the development of stellar wind theory, the general formalism sets the problem for modeling the outflow of mass from a massive star and its overall mass loss rate.

3.5.1 Radiative Accelerating Outflow

The condition for stellar wind mass loss require that the radiation pressure exceed the gravitational force of the star. Assuming first a star's atmosphere acts like a fluid, it can be described as having some density ρ with outflow at a velocity v. One can then begin determining the relationships governing mass outflow of a star using the general fluid equations.

The outflow flux ρv, of a massive star has a mass density much greater than the velocity. This leads to the speed of the mass flow being less than the gas sound speed a. This occurrence at hydrostatic equilibrium is described by the mass outflow equivalent to the gravitational force

$$\nabla P = \rho \mathbf{g_{grav}} \; , \tag{3.13}$$

where ∇P is the pressure gradient and $\mathbf{g_{grav}}$ is the gravitational acceleration. While the pressure can include several contributions, a generic simple approach would be to apply the ideal gas law

$$P = \frac{\rho k T}{\mu} \tag{3.14}$$

where k is Boltzmann's constant, T is temperature, and μ is the mean molecular weight. The sound speed a can now be defined as

$$a = \sqrt{\frac{kT}{\mu}} \; , \tag{3.15}$$

that is the speed at which information propagates through the atmospheric medium. The pressure then depends on the sound speed as

$$P = \rho a^2 \; . \tag{3.16}$$

For a non-equilibrium state in fluid flow, the application of Newton's second law for

a net acceleration gives

$$\frac{d\mathbf{v}}{dt} = \frac{\partial \mathbf{v}}{\partial t} + \mathbf{v} \cdot \nabla \mathbf{v} = -\mathbf{g_{grav}} - \frac{GM_*}{r^2}\hat{\mathbf{r}} + \mathbf{g_x} = -\frac{\nabla P}{\rho} - \frac{GM_*}{r^2}\hat{\mathbf{r}} + \mathbf{g_x} \qquad (3.17)$$

with $\mathbf{v}$ as the flow velocity and $\mathbf{g_x}$ a yet to be defined acceleration factor (e.g., a radiative acceleration). The middle term is the gravitational acceleration dependent on the gravitational constant G and star's mass M_*, as related to a radial factor $\hat{\mathbf{r}}/r^2$.

The general equations of fluid flow also give the relationship between mass density and flow velocity via

$$\frac{\partial \rho}{\partial t} + \nabla \cdot \rho \mathbf{v} = 0 \; , \qquad (3.18)$$

followed by the fluid equation for energy

$$\frac{\partial e}{\partial t} + \nabla \cdot e\mathbf{v} = -P\nabla \cdot \mathbf{v} - \nabla \cdot \mathbf{F}_c + Q_x \; . \qquad (3.19)$$

Terms in the fluid equation for energy are similar to those in 3.17, where the term Q_x is an undefined volumetric transfer of heat energy. The $\mathbf{F}_c$ term represents the conductive heat flux density, dependent on temperature as

$$\mathbf{F}_c = K_o T^{5/2} \nabla T \qquad (3.20)$$

where K_o is the electron conduction coefficient $K_o = 5.6 \times 10^{-7} \text{erg/s/cm/K}^{7/2}$ (Owocki 2005). These equations are in a general sense, fluid equations describing the outflow of mass for a star. Other limiting factors such as opacity are not considered in limiting the flow for these equations. However, the benefit here of these general equations imply solutions for a time-dependent multidimensional stellar wind.

Naturally, one may apply this formalism to a steady state spherically symmetric star to determine the equation of motion. That is, for a star of mass M_*, radius R_*, and bolometric luminosity L_*, the equation for mass conservation is

$$\frac{1}{r^2}\frac{\partial}{\partial r}(\rho v_r r^2) = 0 \; . \tag{3.21}$$

This implies that the term $\rho v_r r^2$ is constant, therefore implying the mass loss rate is

$$\dot{M} = \text{constant} = 4\pi\rho v_r r^2 \; . \tag{3.22}$$

Then, expressing the radial component of the momentum equation gives

$$v\frac{\partial v}{\partial r} = -\frac{1}{\rho}\frac{\partial P}{\partial r} - \frac{GM_*}{r^2} + g_r \; . \tag{3.23}$$

From the ideal gas law, $P = \rho a^2$. Noting that from the mass loss equation 3.22, density ρ can be reduced, the equation of motion becomes

$$\left(1 - \frac{a^2}{v}\right)v\frac{dv}{dr} = \frac{2a^2}{r} - \frac{da^2}{dr} - \frac{GM_*}{r^2} + g_r \; . \tag{3.24}$$

Since massive stars do not possess a hot corona, wind temperatures stay close to the stellar photospheric temperature T_*. The sound speed a thus stays well below the escape velocity $v_{esc} = \sqrt{2GM_*/R_*}$ at the surface, meaning that the gas pressure term is negligible compared to the radiative driving term. A net acceleration that indicates a supersonic outflow thus requires the right hand side of 3.24 to have a net positive right hand side value (Owocki 2005).

A massive star's outflow must overcome gravity. In a Sun-like star, the sound speed terms from 3.24 reach a value higher than the gravitational acceleration term, while the radiative acceleration term, g_r, is effectively non-existent. The condition for mass outflow for a massive star is that the term g_r becomes larger than the gravitational acceleration term. This g_r term consists of two components,

$$g_r = g_e + g_L \; , \tag{3.25}$$

where g_e is due to the scattering of continuum photons by free electrons and g_L is due to spectral lines. The scattering of continuum photons by free electrons does not depend on frequency of photons, but rather on luminosity and opacity via

$$g_e(r) = \frac{\kappa_e L_*}{4\pi r^2 c} \; .\tag{3.26}$$

Operating in tandem with the radiation pressure due to scattering of photons by free electrons is the radiative acceleration due to absorption by multiple various spectral lines in bound atoms.

3.5.2   Radiative Line-Driven Outflow

The second major contribution to the line acceleration in equation 3.25 is the acceleration in spectral lines, g_L. Furthermore, (Owocki 2005) has shown that in contrast to acceleration due to continuum photons scattering off of free electrons, g_e, there are other important and complex contributions to the radiative acceleration that is the shuffling of electrons at discrete energy levels. Early motivations in understanding spectral line acceleration are detailed in (Lucy & Solomon 1970), while more recent discussions can be found in (Cranmer 1996) and (Madura 2010) point to a refinement in theory of stellar winds with spectral line contributions the resonant nature of bound electrons. In its complexity, spectral line contributions involve the sum of total absorption and scattering by atoms. Opacity becomes a factor in limiting the intensity and line acceleration, creating an even greater condition for radiative forces for stellar winds.

The general formalism for understanding spectral line contributions begins with the simplifying assumption of a point-source star. Then, by integrating over all frequencies and angles normalized by the speed of light c, the line force per unit mass at a radius r is given by

$$\mathbf{g_{rad}} = \frac{1}{c} \oint \int_{\nu=0}^{\infty} \kappa_\nu I_\nu(r,\hat{n})\hat{\mathbf{n}}d\Omega d\nu \ . \tag{3.27}$$

The opacity term κ_ν is the total isotropic mass absorption coefficient that includes both scattering and absorption at a frequency ν. The monochromatic frequency-dependent radiative intensity I_ν is integrated along the direction $\hat{\mathbf{n}}$ over all solid angles Ω. The radiative force due to a single line is

$$\mathbf{g_{line}} = \frac{\kappa_L}{c} \oint \int_{\nu=0}^{\infty} \tilde{\phi}(\nu - \nu')I_\nu(r,\hat{n}) \, \hat{\mathbf{n}} \, d\Omega \, d\nu \ , \tag{3.28}$$

where κ_L is the mass absorption coefficient for the line. The term $\tilde{\phi}(\nu)$ is a normalizing line profile function and ν' is the line frequency in the comoving frame of the gas. The relationship between ν' and the emitted frequency ν_0 for a non-relativistic flow velocity $\mathbf{v}(\mathbf{r})$ at a position $\mathbf{r}$ is

$$\nu' = \nu_0 \left(1 + \frac{\hat{\mathbf{n}} \cdot \mathbf{v}(\mathbf{r})}{c}\right) \tag{3.29}$$

For convenience, we use a change of variables

$$x \equiv \left(\frac{\nu - \nu_0}{\Delta\nu_D}\right) \tag{3.30}$$

where the frequency x is defined in units of the Doppler width $\Delta\nu_D = \nu_0 v_{th}/c$, and v_{th} is the ion thermal speed in a gas. Defining the ion thermal speed is similar to defining the isothermal sound speed a, namely,

$$v_{th} = \sqrt{\frac{2k_B T}{A_i m_H}} \ , \tag{3.31}$$

noting that A_i is the mean atomic weight of the driving ions. The single line acceleration force can now be expressed as

$$\mathbf{g_{line}} = \frac{\kappa_L \Delta\nu_D}{c} \oint \int_{\nu=-\infty}^{\infty} \phi\left(x - \frac{\hat{\mathbf{n}} \cdot \mathbf{v}(\mathbf{r})}{v_{th}}\right) I_\nu(r,\hat{n})\hat{\mathbf{n}}d\Omega d\nu \tag{3.32}$$

The line profile functions $\tilde{\phi}$ and ϕ, are noted to be normalized so that

$$\int_{\nu=0}^{\infty} \tilde{\phi}(\nu)d\nu = \int_{\nu=-\infty}^{\infty} \phi(x)dx = 1 \; , \qquad (3.33)$$

where the variable x is extended from $-c/v_{th}$ to $-\infty$ without significant error because of a line's opacity in the overall spectrum being finite (Cranmer 1996; Madura 2010).

The intensity term $I_\nu(r, \hat{\mathbf{n}})$ also is generally comprised of two contributions that make up the total intensity. First there is the direct contribution $I_{\nu,\text{direct}}$ resulting from radiation originating from the core of a star where direct absorption occurs. Then there is the diffuse contribution $I_{\nu,\text{diffuse}}$ due to radiation scattered or created in the wind. However, the diffuse contribution is generally not considered since it is negligible compared to the direct component in most of the wind (Cranmer 1996). The total intensity can be related to the direct contribution via

$$I_{\nu,\text{total}} = I_{\nu,\text{direct}} + I_{\nu,\text{diffuse}} \approx I_{\nu,\text{direct}} \; . \qquad (3.34)$$

Defining the relationship for direct intensity at a distance r, returns a relationship of core intensity I_*, assumed to be at a constant value, so that

$$I_{\nu,\text{direct}}(r) = I_* e^{-\tau_\nu(r)} \; , \qquad (3.35)$$

where $\tau_\nu(r)$ is the optical depth along r. The optical depth τ_ν as defined depends on frequency and is independent of geometry. It is defined along the path r of the moving atmospheric stellar medium as the integral

$$\tau_\nu(r) = \int_{R_*}^{r} \kappa_L \rho(r')\phi\left(x - \frac{\hat{\mathbf{n}} \cdot \mathbf{v}(r')}{v_{th}}\right) dr' \qquad (3.36)$$

Computing this integral then requires an approximation known as the "Sobolev Approximation" that is defined over a characteristic length scale L_{Sob}, while κ_L and

ρ are constant (Sobolev 1960). This allows for a change of variables simplifying the integral. In a physical sense, the flow velocity must be great enough for the Doppler shift to be in resonance with the line frequency near or at the same local point of flow velocity (Cranmer 1996). With the line frequency at a position $\mathbf{r}$ dependent on the Dropper length $\Delta\nu_D$, the local thermal speed of scattering then becomes the lower bound for flow velocity

$$L_{\text{Sob}} \approx \frac{v_{th}}{dv/dr} << \frac{v}{dv/dr} \; , \tag{3.37}$$

implying that the Sobolev length has a lower limit of zero or that flow velocity is much greater than thermal speed. The optical depth integral then becomes

$$\tau_\nu(r) = \kappa_L \rho(r') \int_0^r \phi\left(x - \frac{\hat{\mathbf{n}} \cdot \mathbf{v}(\mathbf{r}')}{v_{th}}\right) dr' \; , \tag{3.38}$$

where κ_L and ρ are treated as constants, and the limits of integration begin at the stellar surface to some position r above. A change of variables can now be imposed by setting

$$x' = x - \frac{\hat{\mathbf{n}} \cdot \mathbf{v}(\mathbf{r}')}{v_{th}} \tag{3.39}$$

and

$$dx' = -\frac{1}{v_{th}}(\hat{\mathbf{n}} \cdot \nabla)(\hat{\mathbf{n}} \cdot \mathbf{v}(\mathbf{r}'))dr' \; . \tag{3.40}$$

In terms of the gradient of velocity from differentiation, the terms remain almost constant as the varying of flow velocity is slow or close to v_{th} in scale. Expressing the optical depth integral now leads to

$$\tau_\nu(r) = \frac{\kappa_L \rho(r')v_{th}}{(\hat{\mathbf{n}} \cdot \nabla)(\hat{\mathbf{n}} \cdot \mathbf{v}(\mathbf{r}'))} \int_{x - \hat{\mathbf{n}} \cdot \mathbf{v}(\mathbf{r}')/v_{th}}^{\infty} \phi\left(x'\right) dr' \tag{3.41}$$

where the "Sobolev optical depth" is defined as the terms outside the integral

$$\tau_S \equiv \kappa_L \rho \left[\frac{v_{th}}{(\hat{\mathbf{n}} \cdot \nabla)(\hat{\mathbf{n}} \cdot \mathbf{v}(\mathbf{r}'))}\right] \; , \tag{3.42}$$

while the line profile function is redefined for convenience so that

$$\Phi(x, \mathbf{r}) \equiv \int_{x-\hat{\mathbf{n}}\cdot\mathbf{v}(\mathbf{r}')/v_{th}}^{\infty} \phi\left(x'\right) dr' \, . \tag{3.43}$$

The line force equation (equation 3.32) can now be expressed as

$$\mathbf{g_{line}} = \frac{\kappa_L \Delta\nu_D}{c} \oint \int_{x=-\infty}^{\infty} I_* e^{-\tau_S \Phi(x,\mathbf{r})} \, \hat{\mathbf{n}} \, d\Omega \, d\Phi(x, \mathbf{r}) \, . \tag{3.44}$$

Thus, integrating this gives the general form for the force due to a single line

$$\mathbf{g_{line}} = \frac{\kappa_L \Delta\nu_D}{c} \left(\oint I_* \hat{\mathbf{n}} \, d\Omega \left[\frac{1 - e^{-\tau_S}}{\tau_S} \right] \right) \, . \tag{3.45}$$

The term in brackets is the total radiation flux at frequency ν and distance r.

3.5.3   An Ensemble of Lines

In reality, the radiative force is comprised of a series of lines that drive the stellar wind. Consider the sum of all single line forces from equation 3.45 as

$$\mathbf{g_{lines}} = \sum_{\text{lines}} \frac{\kappa_L \Delta\nu_D}{c} \left(\oint I_* \hat{\mathbf{n}} d\Omega \left[\frac{1 - e^{-\tau_S}}{\tau_S} \right] \right) \, , \tag{3.46}$$

where $\mathbf{g_{line}}$ represents an ensemble for a statistical distribution since the number of lines is very large. Recalling that the Doppler shift for a line frequency is $\Delta\nu_D = v_0 v_{th}/c$, and that the radiative flux $F_\nu = L_\nu/4\pi r^2$, the ensemble is computed to be

$$\mathbf{g_{lines}} = \sum_{\text{lines}} \frac{\kappa_L v_0 v_{th} L_\nu}{4\pi r^2 c^2} \left[\frac{1 - e^{-\tau_S}}{\tau_S} \right] \, , \tag{3.47}$$

and the optical depth τ_S has the value

$$\tau_S = \frac{\kappa_L v_t h \rho(r)}{\partial v/\partial r} \, . \tag{3.48}$$

Because massive stars are hot and luminous, the lines under consideration are near the peak of the continuum spectrum such that $v_0 L_\nu \to L_*$ (Madura 2010). The ensemble of line forces then becomes

$$\mathbf{g_{lines}} = \sum_{\text{lines}} \frac{\kappa_L v_{th} L_*}{4\pi r^2 c^2} \left[\frac{1 - e^{-\tau_S}}{\tau_S} \right] \tag{3.49}$$

Computing the cumulative sum of line forces requires a simplifying assumption that the spectral distribution keeps each line independent (Owocki 2005). A way to compute the cumulative line-force from a parameterized ensemble of lines by simply assuming that the spectral distribution keeps the individual lines nearly independent was developed by (Castor et al. 1975) and is referred to generally as CAK Theory. In CAK theory, the line force is treated as a force multiplier that follows a power law

$$\mathbf{g_{line}} = kt^{-\alpha} \, , \tag{3.50}$$

where k represents the scaling factor of the line force and α determines the fraction of optically thick lines. t is the optical depth

$$t = \frac{\kappa \rho v_{th}}{\partial v / \partial r} \tag{3.51}$$

This would eventually be generalized by (Owocki 2005) in the form of line strength q as

$$q \frac{dN}{dq} = \frac{1}{\Gamma(\alpha)} \left(\frac{q}{\bar{Q}} \right)^{\alpha - 1} \, , \tag{3.52}$$

where $\Gamma(\alpha)$ is the Gamma function. The summation in equation 3.49 can then be evaluated as an integral over the number distribution dN/dq. Applying typical parameters for a massive stars, in our case spectral types O and B, gives a constant cumulative line strength $\bar{Q}$ that provides a convenient overall normalization (Madura 2010). Typically, $\bar{Q} \sim 2000$. The line force ensemble for a point-star line-force can then be expressed as

$$\mathbf{g_{lines}} = \frac{1}{1 - \alpha} \frac{\bar{Q} \kappa_e L_*}{4 \pi r^2 c} \left(\frac{\partial v / \partial r}{\rho c \bar{Q} \kappa_e} \right)^{\alpha} \, . \tag{3.53}$$

3.5.4   The One-Dimensional Point-star CAK Wind Model

Modeling stellar winds from massive stars requires applying both radiative acceleration and line acceleration. Radiation pressure becomes the main driving

force over gas pressure in stable stars. The sound speed, a, is assumed to be zero in this case, so that the radial momentum equation in one dimension from equation 3.23 is expressed as

$$v\frac{dv}{dr} = (\Gamma - 1)\frac{GM_*}{r^2} + \frac{\bar{Q}\kappa_e L_*}{4\pi r^2 c}\frac{1}{1 - \alpha}\left[\frac{4\pi r^2 v dv/dr}{\bar{Q}\kappa_e \dot{M}c}\right]^\alpha ,$$ (3.54)

where the mass loss rate is $\dot{M} = 4\pi r^2 \rho v$ is used to determine ρ and Γ is the Eddington parameter. Further simplification starts by defining a single term ω' in terms of the Eddington parameter and gravitational force

$$\omega' = -\frac{1}{1 - \Gamma}\left(\frac{r^2}{GM_*}\right)\left(v\frac{dv}{dr}\right) ,$$ (3.55)

which will be used to represent the left hand side (LHS) of 3.54. For the right hand side (RHS), after some algebra, equation 3.54 becomes

$$\omega' = -1 + \frac{L_*}{c^{1+\alpha}(1 - \alpha)\dot{M}^\alpha}\left[\frac{4\pi GM_*(1 - \Gamma)}{\bar{Q}\kappa_e}\right]^{\alpha - 1}\omega'^\alpha ,$$ (3.56)

or equivalently,

$$\omega' = -1 + C\omega'^\alpha ,$$ (3.57)

where

$$C \equiv \frac{1}{1 - \alpha}\left(\frac{\bar{Q}\Gamma}{1 - \Gamma}\right)^{1-\alpha}\left(\frac{L_*}{\dot{M}c^2}\right)^\alpha .$$ (3.58)

Because the mass loss rate is inversely proportional to C, solving for this term in 3.57 is the final task in determining the functional form of the wind velocity. The RHS in equation 3.57 is referred to as the line force while the LHS refers to the amount of inertia in relation to gravity. There are two solutions possible assuming that the mass loss rate is small, and no solution exists when mass loss is high (Madura 2010). At the critical value, the expression is

$$\alpha C_c \omega'^{\alpha - 1} = 1$$ (3.59)

where the critical conditions occur at

$$\omega'_c = \frac{\alpha}{1 - \alpha} = \text{constant} \tag{3.60}$$

and

$$C_c = \frac{1}{\alpha^\alpha (1 - \alpha)^{1-\alpha}} \ . \tag{3.61}$$

As a result, simplifying equation 3.59 with equation 3.60 and 3.61 yields the

maximum CAK mass loss rate as

$$\dot{M} = \frac{L_*}{c^2} \frac{\alpha}{1 - \alpha} \left[\frac{\bar{Q}\Gamma}{1 - \Gamma} \right]^{(1-\alpha)/\alpha} , \tag{3.62}$$

which holds at all radial distances. Determining the wind velocity requires a spacial

integration of equation 3.60, noting that the term $\omega' = r^2 v (dv/dr)/(1 - \Gamma)GM_*$.

This yields the CAK velocity law from the stellar surface at radius R_*

$$v_{\text{wind}} = v_{\text{esc}} \sqrt{\frac{\alpha}{1 - \alpha}} \left(1 - \frac{R_*}{r} \right)^\beta , \tag{3.63}$$

where v_{esc} is the escape velocity defined as

$$v_{esc} = \sqrt{\frac{2GM_*(1 - \Gamma)}{R_*}} \tag{3.64}$$

and β determines how fast the terminal speed v_∞ is reached (typically $\beta = 1/2$ or

1). The terminal speed of the wind is

$$v_\infty = v_{esc} \sqrt{\frac{\alpha}{1 - \alpha}} , \tag{3.65}$$

which is close to the escape speed. In fact, for $\alpha = 1/2$, the terminal and escape

speeds are equal. Applying this formalism to η Car allows us to set the parameters

necessary for modeling the system's stellar winds.

CHAPTER 4
COLLIDING WINDS OF MASSIVE BINARIES

Stellar winds are a result of a driving radiation pressure, and for a massive binary system like η Car, the winds produced by each star will collide between the stars, forming a wind-wind collision (WWC) zone. In order to provide context for the later discussion of η Car's WWC, here we briefly discuss the physics and dynamics involved in colliding wind binary systems. Recent studies of η Car show that forbidden line emission near the WWC observed by the Hubble Space Telescope (HST, Gull et al. 2011) can be compared to the results of 3D hydrodynamical modeling (Madura 2010), helping provide tighter constraints on the system's stellar, wind, and orbital parameters. These results show strong evidence in fortifying models that explain the structure of η Car. Earlier modeling on binary interactions begins with an analytical approach to the wind-wind interaction problem (Canto et al. 1996). Other studies set some fundamental groundwork for modeling the interaction of the collision zone in two and three dimensions.

4.1 The Thin-shell Two-Wind Interaction Problem

The physics of colliding winds are an important aspect of modeling the η Car binary, and by solving this problem analytically we gain insights useful for interpreting numerical simulations. We start with the assumptions of spherical symmetry and a near static orbital motion relative to the winds (i.e. the orbital velocity is assumed to be much smaller than either wind velocity, a valid assumption for wide binaries). The two stars are separated by a distance D. The plane equidistant from both stars where the winds collide is referred to as the contact discontinuity. The interaction of the two winds produces two oppositely faced shocks

that are separated by the contact discontinuity. Here, opposite facing winds meet after reaching terminal velocity (it is assumed for simplicity that each star's wind has reached its terminal velocity before collision), and d_1 and d_2 are the distances of each star from their respective shocks on each side of the contact discontinuity. In the case of two identical colliding stellar winds (illustrated in Figure 4.1), the contact discontinuity is simply a plane equidistant between the stars.

For unequal wind velocities and wind separation, the intersection of the line of centers and the contact discontinuity is found using one-dimensional momentum balance

$$\rho_1 v_1^2 = \rho_2 v_2^2 \ , \tag{4.1}$$

where, by replacing the wind density with the appropriate expression in terms of the mass loss rates ($\dot{M}_i$) and distances d_1 and d_2, we can write

$$\left(\frac{\dot{M}_1 v_1}{\dot{M}_2 v_2} \right)^{1/2} = \frac{d_1}{d_2} \ . \tag{4.2}$$

This works nicely when the stellar separation satisfies $D >> R_*$, where R_* is the radius of a given star (Stevens et al. 1992). However, in the case of close binaries or highly elliptical systems like η Car, the interaction region may, at times, be within the acceleration region of one of the stellar winds, in which case the above formula does not hold. Also, if the momentum flux of one star is significantly greater than that of the other it is possible that no balance exists and that the stronger wind will overwhelm the companion star's wind and strike the surface of the companion star directly (Stevens et al. 1992).

Nonetheless, the above approach is still valid for the majority of η Car's binary orbit when the stellar separation is large (~ 29 AU) and orbital velocities are low. An analysis carried out by (Canto et al. 1996) shows that for two hypersonic,
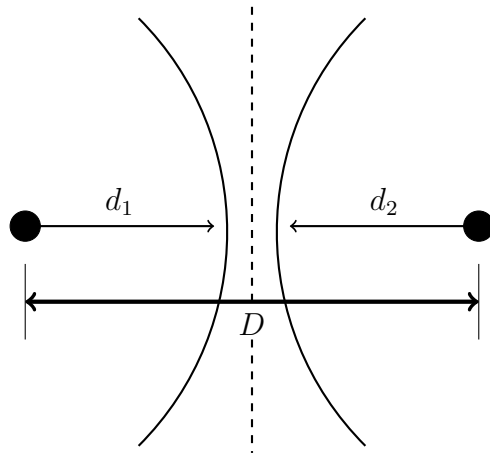
Figure 4.1: An illustration of a simple binary wind-wind collision between two stars with identical winds. Here the binary wind collision occurs at the center equidistant between the stars, which are separated by a distance D. The distances of the winds from each star to the contact discontinuity are d_1 and d_2. Symmetry is to be assumed for this simple case.

constant velocity, isotropic stellar winds in the "thin-shock approximation" (when radiative cooling is so efficient that gas pressure never plays a role in the overall shock dynamics), there exists a system of four algebraic equations describing the contact discontinuity surface that can be solved analytically. The analysis of (Canto et al. 1996) also includes analytic forms for the asymptotic opening angle of the shock surface and the tangential velocity and mass surface density of the flow along the thin-shell wall.

4.1.1   An Algebraic Expression of the Two-Wind Interaction

The formalism of (Canto et al. 1996) begins with the assumption of two non-accelerated hypersonic colliding winds forming a thin shell at the collision zone. The collision zone center is where the contact discontinuity will exist as it plays a role in how the curvature is adjusted on different parameters of the radiative shocks. Other assumptions to be made are cylindrical symmetry and zero azimuthal velocity. The locus of the thin shell is parameterized by $R(\theta)$, where R is the radial distance describing the curve at an angle θ, the polar angle. In further describing the thin shell, and because gas is well mixed in this zone, there exists a single flow velocity

$$\bar{\mathbf{v}} = v_r\hat{\mathbf{r}} + v_z\hat{\mathbf{z}} , \tag{4.3}$$

where $\hat{\mathbf{r}}$ and $\hat{\mathbf{z}}$ are unit vectors along the cylindrical and symmetry axes (looking at the system from above), respectively. Suppose that θ is the angle of the control line on the surface layer of this shell. Moreover, suppose that $\dot{M}(\theta)$, $\dot{\Pi}_r(\theta)$, $\dot{\Pi}_z(\theta)$, and $\dot{J}(\theta)$ are the mass, r and z momentum, and angular momentum around the origin through the control line, respectively. The relationships between these terms are

$$\dot{\Pi}_r(\theta)\hat{\mathbf{r}} + \dot{\Pi}_z(\theta)\hat{\mathbf{z}} = \dot{M}(\theta)[v_r(\theta)\hat{\mathbf{r}} + v_z(\theta)\hat{\mathbf{z}}] , \tag{4.4}$$

$$\dot{J}(\theta) = \dot{M}(\theta)v_\theta(\theta)R(\theta) , \tag{4.5}$$

where $v_\theta = v_r \cos\theta - v_z \sin\theta$. The assumption of a steady state means that the rates of mass and linear/angular momentum through the control line must equal those injected by the two winds between the direction of the symmetry axis and the angle θ. Through the control line the equivalent injected winds have the same relationship $\dot{M}_w(\theta)$, $\dot{\Pi}_{wr}(\theta)$, $\dot{\Pi}_{wz}(\theta)$, and $\dot{J}_w(\theta)$, where one of the winds is denoted w and the other w_1 (subscript 1). Then,

$$\dot{\Pi}_r(\theta)\hat{\mathbf{r}} + \dot{\Pi}_z(\theta)\hat{\mathbf{z}} = [\dot{\Pi}_{wr}(\theta) + \dot{\Pi}_{wr_1}(\theta)]\hat{\mathbf{r}} + [\dot{\Pi}_{wz}(\theta) + \dot{\Pi}_{wz_1}(\theta)]\hat{\mathbf{z}} \quad (4.6)$$

$$\dot{J}(\theta) = \dot{J}_w(\theta) + \dot{J}_{w1}(\theta) \quad (4.7)$$

$$\dot{M}(\theta) = \dot{M}_w(\theta) + \dot{M}_{w1}(\theta) \quad (4.8)$$

Then by equating these to the earlier equations above,

$$\dot{M}(\theta)[v_r(\theta)\hat{\mathbf{r}} + v_z(\theta)\hat{\mathbf{z}}] = [\dot{\Pi}_{wr}(\theta) + \dot{\Pi}_{wr_1}(\theta)]\hat{\mathbf{r}} + [\dot{\Pi}_{wz}(\theta) + \dot{\Pi}_{wz_1}(\theta)]\hat{\mathbf{z}} \quad (4.9)$$

$$\dot{M}(\theta)v_\theta(\theta)R(\theta) = \dot{J}_w(\theta) + \dot{J}_{w1}(\theta) \quad (4.10)$$

Dividing by $\dot{M}v_\theta$ and using the fact that $v_\theta = v_r \cos\theta - v_z \sin\theta$, it follows that

$$R = \frac{\dot{J}_w(\theta) + \dot{J}_{w1}(\theta)}{v_\theta(\theta)R(\theta)} = \frac{\dot{J}_w(\theta) + \dot{J}_{w1}(\theta)}{[\dot{\Pi}_{wr}(\theta) + \dot{\Pi}_{wr_1}(\theta)]\cos\theta - [\dot{\Pi}_{wz}(\theta) + \dot{\Pi}_{wz_1}(\theta)]\sin\theta} , \quad (4.11)$$

the locus of the contact discontinuity layer. The mass-loss rate now can be determined through the surface mass density σ and flow velocity v as

$$\dot{M}(\theta) = 2\pi[R(\theta)\sin\theta]\sigma v \quad (4.12)$$

4.1.2 The Two-Wind Interaction of Unequal Wind Velocities

Now, consider two spherical unequal winds separated by a distance D. A detailed illustration representative of this scenario is shown in Figure 4.2.
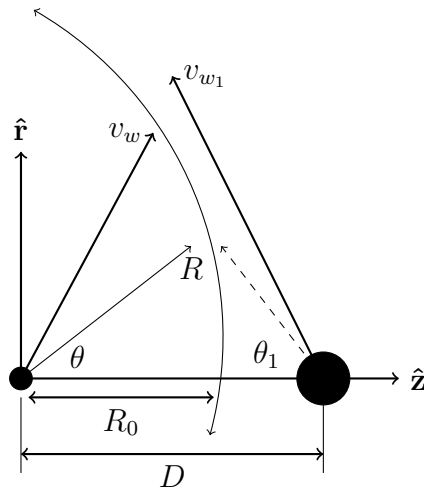
Figure 4.2: Schematic diagram representing two point star sources of spherical winds separated by distance D. With two unequal wind velocities, v_w of the first (left) source and v_{w_1} of the second (right) source, the contact discontinuity shell is curved towards the star with the weaker wind, intersecting the symmetry axis $\hat{\mathbf{z}}$ at a distance R_0 from the origin. The surface layer is described by shell distance R over an angle θ from the first source, and angle θ_1 from the second source.

Writing out the equations for mass loss rate, velocity, and angular momentum for the first source,

$$\dot{M}_{w_1}(\theta_1) = \frac{\dot{M}_{w_1}^0}{2}(1 - \cos\theta_1) \tag{4.13}$$

$$\dot{\Pi}_{wz_1}(\theta_1) = -\frac{\dot{M}_{w_1}^0 v_{w_1}}{4}\sin^2\theta_1 \tag{4.14}$$

$$\dot{\Pi}_{wr_1}(\theta_1) = \frac{\dot{M}_{w_1}^0 v_{w_1}}{4}(\theta_1 - \sin\theta_1\cos\theta_1) \tag{4.15}$$

$$\dot{J}_{w_1}(\theta_1) = \frac{\dot{M}_{w_1}^0 v_{w_1}}{4}(\theta_1 - \sin\theta_1\cos\theta_1)D , \tag{4.16}$$

where θ_1 is the angle from second source to the thin shell and $\dot{M}_{w_1}^0$ is the mass loss rate of the second wind source located at $z = D$. The equations for the second source located at the origin are similar,

$$\dot{M}_w(\theta) = \frac{\dot{M}_w^0}{2}(1 - \cos\theta) \tag{4.17}$$

$$\dot{\Pi}_{wz} = \frac{\dot{M}_w^0 v_w}{4}\sin^2\theta \tag{4.18}$$

$$\dot{\Pi}_{wr}(\theta) = \frac{\dot{M}_w^0 v_w}{4}(\theta - \sin\theta\cos\theta) \tag{4.19}$$

$$\dot{J}_w(\theta) = 0 . \tag{4.20}$$

Then, with the equations above and equation 4.11, and using the geometric relationship

$$R = D\sin\theta_1\csc(\theta + \theta_1) \tag{4.21}$$

one obtains

$$\theta_1\cot\theta_1 = 1 + \eta(\theta\cot\theta - 1) , \tag{4.22}$$

where η, is the momentum ratio defined as $\eta \equiv (\dot{M}_w^0 v_w)/(\dot{M}_{w_1}^0 v_{w_1})$. Solving for radius R then only involves giving values for θ, which in turn determines θ_1 for R. Given an angle θ, equation 4.22 can be approximated via an expansion assuming

small values of θ_1 and β, giving

$$\theta_1 \cot \theta_1 \approx 1 - \frac{\theta_1^2}{3} - \frac{\theta_1^4}{45} , \qquad (4.23)$$

and through substitution with 4.22, an approximation for θ_1 is

$$\theta_1 \approx \left\{ \frac{15}{2} \left[-1 + \sqrt{1 + \frac{4}{5}\beta(1 - \theta \cot \theta)} \right] \right\}^{1/2} . \qquad (4.24)$$

At the point of stagnation, the value R_0 can be determined from

$$R_0 = \frac{\sqrt{\eta}D}{1 + \sqrt{\eta}} . \qquad (4.25)$$

The asymptotic opening angle of the bow shock, θ_∞, corresponding to $R \to \infty$, is found using the condition $\theta_\infty + \theta_{\infty_1} = \pi$ in equation 4.22, which gives

$$\theta_\infty - \tan \theta_\infty = \frac{\pi}{1 - \beta} . \qquad (4.26)$$

Comparing the equations for mass loss rate, velocity, and angular momentum, the tangential velocity of the flow along the shell is

$$\frac{v_t}{v_w} = \frac{\sqrt{[\alpha(\theta - \sin\theta\cos\theta) + (\theta_1 - \sin\theta_1\cos\theta_1)]^2 + [\alpha\sin^2\theta - \sin^2\theta_1]^2}}{2[\alpha(1 - \cos\theta) + \beta(1 - \cos\theta_1)]} , \qquad (4.27)$$

where $\beta = v_w/v_{w_1}$ is the ratio of the wind velocities from both sources (note that this is NOT the same β as that used for the CAK wind velocity law). The mass surface density can be also obtained to be

$$\sigma = \frac{\sigma_0 \sin(\theta + \theta_1) \csc\theta \csc\theta_1 [\alpha(1 - \cos\theta) + \beta(1 - \cos\theta_1)]^2}{\sqrt{[\alpha(\theta - \sin\theta\cos\theta) + (\theta_1 - \sin\theta_1\cos\theta_1)]^2 + [\alpha\sin^2\theta - \sin^2\theta_1]^2}} , \qquad (4.28)$$

where $\sigma_0 = \dot{M}_w^0/2\pi\beta D v_w$.
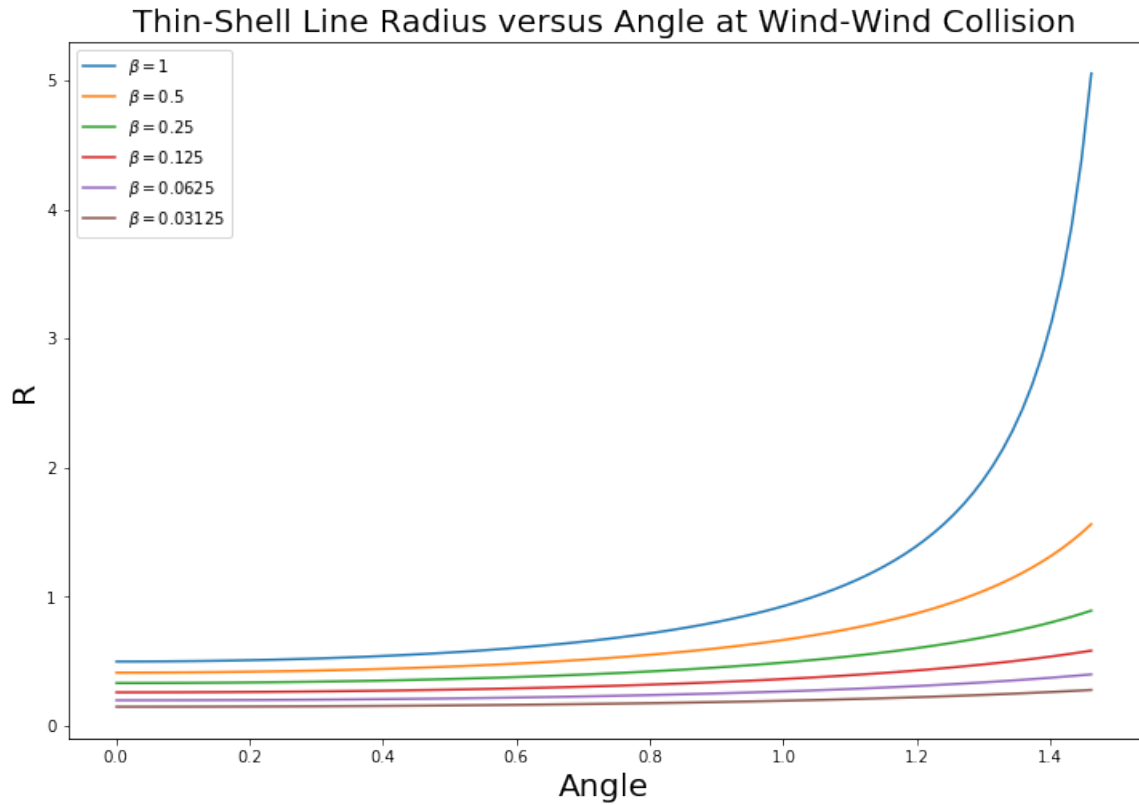
Figure 4.3: An approximate solution of radial distance from first source with respect to angle. As momentum balance shifts away from $\beta = 1$, the curvature of radius approaches a constant value for increasing angular values. For $\beta = 1$, the radius approaches large values for increasing angle given that there is a momentum balance at the collision zone.
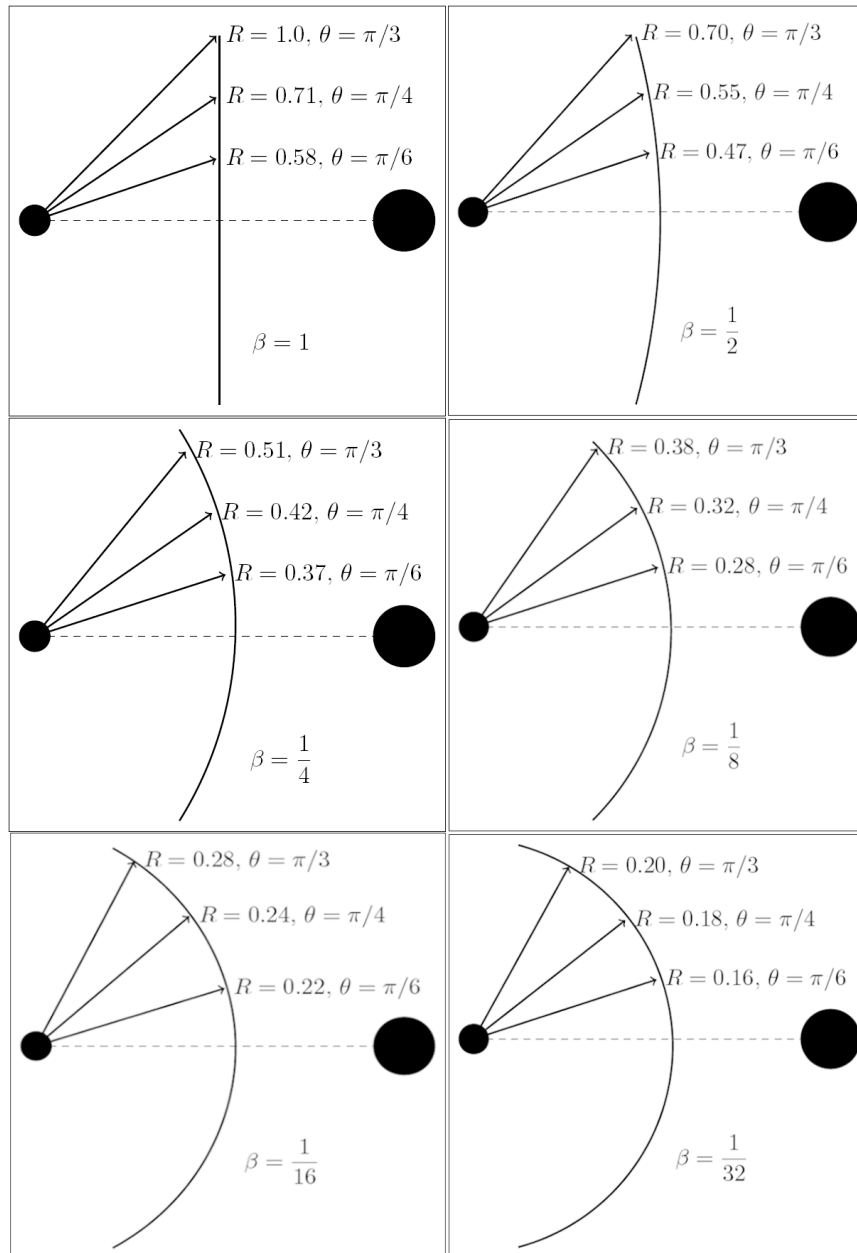
Figure 4.4: Further illustrating figure 4.3 are changes in momentum balance $\beta = 1, 1/2, 1/4, 1/8, 1/16$, and $1/32$. Shown in each figure are radial distance at a given an angle θ. As momentum begins to unbalance $\beta < 1$, the values of distance begin to approach a constant value. This indicates in increasing curvature of the thin-shell collision zone as momentum balance shifts.

4.2   Wind Temperature and Radiative Cooling

Some important physical effects that occur in the shocks of the WWC zone are those of radiative and adiabatic cooling. The presence or absence of radiative cooling can have a significant effect on the overall geometry of the WWC zone. Radiative cooling also plays an important role in determining the thickness, final temperature, and density of the post-shock region, which can have important implications for various physical processes and the interpretation of observations (Madura 2010).

When radiative cooling plays a role in colliding winds, an additional length scale is introduced into the system, $l_{cool} = t_{cool}v$. A cooling parameter χ, as defined by (Stevens et al. 1992), is the ratio of the cooling time for the shocked gas to the escape time from the intershock region, $\chi = t_{cool}/t_{esc}$. For an emission rate, Λ, the cooling time is approximately

$$t_{cool} = \frac{kT_s}{4n_w\Lambda(T_s)} \ , \tag{4.29}$$

where n_w is the number density of the wind at the shock and T_s is the temperature of the shock-heated wind. The escape time from the shocked region near the line of centers is

$$t_{esc} = \frac{d}{c_s} \ , \tag{4.30}$$

where d is the distance from the star to the contact discontinuity (radius of curvature) and c_s is the post-shock sound speed along the line of centers. The shock temperatures that occur in colliding wind binaries lie near a local minimum in $\Lambda(T)$, see (Stevens et al. 1992) for details. This allows $\Lambda(T)$ to be approximated locally with a constant value. In this case,

$$\chi = \frac{t_{cool}}{t_{esc}} \approx \frac{v_8^4 d_{12}}{\dot{M}_{-7}} \ , \tag{4.31}$$

where v_8 is the wind velocity in units of 10^8 cm s^{-1}, d_{12} is the distance to the contact in units of 10^{12} cm, and $\dot{M}_{-7}$ is the mass loss rate in units of $10^{-7}\,M_\odot\,\text{yr}^{-1}$. As a note, this is only an approximation since the temperature dependence is neglected. However, χ does serve as a characteristic measure of the importance of radiative cooling, and each of the two stellar winds in the system will have its own characteristic value of χ. The physical meaning for χ occurs when $\chi \gtrsim 1$ or $\chi \ll 1$. When $\chi \gtrsim 1$, the shocked wind cools adiabatically, while for $\chi \ll 1$, it is roughly isothermal (i.e. highly radiative). Additionally, $\chi \propto d_{12}$, which implies $\chi \propto P_{orb}^{2/3}$, meaning that, all else being equal, the longer the orbital period of the binary, the more adiabatic the shocked region will be. Alternatively, in highly elliptical systems like η Car, χ can vary with orbital phase, with the cooling switching from one regime to the other as the stellar separation changes (i.e. adiabatic to radiative and back, or vice versa; Madura et al. 2013).

4.3   Past Two and Three Dimensional Modeling

With nearly three decades in the history of modeling CWBs, it starts first with two dimensional hydrodynamical modeling and through the progression of time came three dimensional modeling. There are however, varying elements to modeling other than a simple, in-plane colliding wind binary problem. Elements such as the consideration of rotation or effects at different orbital periods are added complexity to further detail CWBs but are not applied to this effect. In the early stages two dimensional hydrodynamical modeling performed by (Owocki et al. 1994) starts by applying a piecewise parabolic method (PPM) of line driven stellar winds. The results in this study show the fluid-like flow of radiation drive stellar winds constrained to a plane geometry. The authors of this study then applied the method of PPM in a code for modeling hydrodynamic fluid flows called VH-1, a

multidimensional ideal compressible hydrodynamics code written in FORTRAN. On more recent simulations, are three dimensional (3D) hydrodynamical modeling performed by (Okazaki et al. 2008) through applying Smooth Particle Hydrodynamics (SPH) on η Car wind collisions modeling an X-ray lightcurve. Subsequent to this study are ongoing SPH simulations in the η Car system with (Madura 2010) to further understand the intrinsic properties of the system. These simulations model η Car's binary wind-wind collision along with properties on radiative transfer that allow for synthesizing observations across a broad range of of wavelengths. When mass loss is apparent, further properties could be understood through a recent study performed by (Madura et al. 2013). From applying small-domain SPH simulations on η Car colliding winds this study shows that the post-shock winds can vary through switching from adiabatic to radiative cooling at periastron passage. Radiative transfer also becomes important for presenting a dynamical model of η Car's broad [Fe III] emission from observations by the Hubble Space Telescope (Madura et al. 2012). Now with SPH simulations on η Car's binary colliding winds, and also for the first time, a three dimensional orientation is constrained to a definite binary orbit.

At present, modeling stellar winds take on 3D high resolution hydrodynamical simulations making use of adaptive-mesh refinement grid-based code RAMSES, see (Teyssier 2002) and (Calderón et al. 2020). In this study, RAMSES is applied to study theoretical models that are generated from wind collisions resulting in cold, dense clumps that are not well understood. These results also indicate the importance of radiative and adiabatic transfers in wind collisions while instabilities are responsible for forming material clumps. Ultimately, modeling the wind collision of η Car's binary wind collision this same numerical process can be applied.

CHAPTER 5
NUMERICAL SIMULATION SETUP

5.1   Equations

We simulate η Car's time-dependent binary wind-wind collisions using the adaptive-mesh refinement (AMR) hydrodynamics code `RAMSES` (Teyssier 2002). Our numerical setup closely follows that performed by (Calderón et al. 2020), but with parameters and adjustments unique to η Car's system. To start, `RAMSES` is based on solving the Euler fluid equations in conservative form,

$$\frac{\partial \rho}{\partial t} + \nabla \cdot (\rho \mathbf{u}) \;=\; 0 \;, \tag{5.1}$$

$$\frac{\partial}{\partial t}(\rho \mathbf{u}) + \nabla \cdot (\rho \mathbf{u} \otimes \mathbf{u}) \;=\; \rho \mathbf{f}(\mathbf{x}) - \nabla P \;, \tag{5.2}$$

$$\frac{\partial}{\partial t}(\rho e) + \nabla \cdot \left[\rho \mathbf{u} \left(e + \frac{P}{\rho} \right) \right] \;=\; -\frac{\rho^2}{(\mu m_H)^2} \Lambda(T) \;, \tag{5.3}$$

where ρ, $\mathbf{u}$, and P are the mass density, velocity, and pressure of the fluid, respectively, while $\mathbf{f}$ is the gravitational force per mass unit and e is the total specific energy density given by

$$e = \frac{1}{2}\mathbf{u} \cdot \mathbf{u} + \frac{P}{(\gamma - 1)\rho} \;, \tag{5.4}$$

where γ is the adiabatic index that is set to 5/3 for adiabatic gases. In addition, μ is the mean molecular weight, m_H is the proton mass, T is the temperature of the gas, and $\Lambda(T)$ is the energy losses due to optically thin radiative cooling.

5.2   Numerical Setup

Performing the 3D simulation of η Car begins by making use of AMR on a Cartesian coordinate grid, where the resolution is enhanced in regions of the domain where specified physical criteria area met. The origin of the Cartesian coordinate

system $(0, 0, 0)$ lies at the center of the cubic computational domain and on each side of the cubic domain there is an outflow boundary condition. The cubic domain side length is set to 108.15 AU, where 1 AU is the mean distance from the center of the Earth to the center of the Sun. This corresponds to a side length of $7a$, where $a = 15.45$ AU is the length of the η Car system's orbital semimajor axis. The length scale was chosen to ensure that the development of instabilities in the wind-wind interaction regions would be adequately captured by the AMR grid while still allowing the simulations to be completed within the maximum allowed time frame (5 days) on available NASA supercomputing resources. We also used an exact Riemann solver with a first-order flux limiter (MinMod) in order to avoid quenching of instabilities by numerical diffusion (Calderón et al. 2020). Flow variables followed throughout the simulation include density, temperature, and wind velocities in each coordinate direction. AMR is set based on density gradients so that resolution increases in the shock zones and any other discontinuities. For the coarse resolution before refinement, the resolution of the simulation is set to 128^3 cells. We allow for up to an additional four levels of grid refinement, leading to an effective resolution of 2048^3 cells (see e.g., Figures 5.2 and 5.3). An element of resolution can reach lengths as low as 54.075 AU$/1024 \approx 0.053$ AU.

Our simulation uses stellar, wind, and orbital parameters specific to the η Car system. These parameters are based on previous works and 3D hydrodynamical simulations of η Car (e.g., Madura et al. 2012, 2013). Table 5.1 lists the parameters used for the simulation in this thesis. The initial condition for our simulation places the stars at their appropriate orbital positions at an orbital phase of $\phi = 0.8$ (phase $\phi = 1.0$ corresponds to periastron and $\phi = 0.5$ apastron). Due to computational resource and time constraints, we ran the simulation only for orbital phases of interest around periastron passage when the η Car system is most dynamic and

Parameter	η_A	η_B
$M_\star$ ($M_\odot$)	90	30
$R_\star$ ($R_\odot$)	60	30
T_{wind} (10^3 K)	4.5	4.5
$\dot{M}$ (10^{-4} $M_\odot$ yr^{-1})	8.5	0.14
v_∞ (km s^{-1})	420	3000
β	1	1
η	0.12	
q	22.28	
P_{orb}(days)	2024	
e	0.90	
a (AU)	15.45	

Table 5.1: η_A and η_B refer to the primary and secondary star, respectively. $M_\odot$ and $R_\odot$ are the solar mass and radius, respectively. T_{wind} is the initial wind temperature. $\dot{M}$, v_∞, and β are the stellar-wind mass-loss rate, terminal speed, and velocity-law index, respectively. $\eta \equiv (\dot{M}v_\infty)_{\eta_B}/(\dot{M}v_\infty)_{\eta_A}$ is the wind momentum ratio, q is the η_A/η_B stellar luminosity ratio assuming $L_{\star,\eta_A} = 5 \times 10^6$ $L_\odot$, P_{orb} is the orbital period, e is the orbital eccentricity, and a is the length of the orbital semimajor axis. Reference: (Madura et al. 2013)

orbital speeds are comparable to the primary star's wind terminal speed, i.e., $0.8 \leq \phi \leq 1.2$ (Madura et al. 2013). The two stars orbit counter-clockwise when the system is viewed from above along the $+z$ axis.

The simulation in this thesis was performed using resources provided by the NASA High-End Computing (HEC) Program through the NASA Advanced Supercomputing (NAS) Division at Ames Research Center. Specifically, the simulation was performed on the Pleiades supercomputer using 1152 Intel Xeon 12-core E5-2680v3 2.5-Ghz (Haswell) CPUs (48 nodes with 24 CPUs and 128 GB of memory per node) in parallel and a run time of 120 continuous hours (5 days).

5.2.1 Stellar Wind Generation

The generation of the individual stellar winds follows the general procedure outlined in (Lemaster et al. 2007) and (Calderón et al. 2020). We impose the wind solutions starting from the Euler fluid equations onto a spherical mask of appropriate radius a_w around each star. Within these "masked regions" the hydrodynamic variables are reset to the appropriate 1D wind solutions after every time step in the simulation. We set the individual stellar winds using the standard 'beta-velocity law' $v(r) = v_\infty (1 - R_\star/r)^\beta$, where v_∞ is the wind terminal velocity, $R_\star$ the stellar radius, and β the velocity-law index. The wind density for each star is set following Equation 3.22, assuming $\dot{M} = \text{constant}$. In order to fully capture the spherical nature of the winds on our Cartesian grid, we force the masked regions to be refined up to the maximum level of AMR. The hydrodynamic variables, including density, velocity, and pressure, within the masks are kept fixed in time. The initial temperatures of the winds and the floor temperature of the simulation are set by the adiabatic sound speed, c_s. We set the sound speed in our simulation to $c_s \approx 10 \, \text{km s}^{-1}$, corresponding to $T \approx 4.5 \times 10^3$ K. We note that the effect of the

initial wind temperature on the flow dynamics is negligible (Madura et al. 2013). Additionally, the floor temperature used is a reasonable approximation for that which would be set in reality via photoionization heating by the UV radiation fields of the stars (Madura et al. 2013). Solar metallicity ($Z = Z_\odot$) is assumed for both winds, consistent with previous 3D simulations of η Car (Madura et al. 2012, 2013).

Figures 5.1 and 5.2 show the density in the orbital plane, with and without the AMR grid, at a time shortly after the initialization of our simulation (orbital period $\phi \approx 0.80$). Figure 5.3 is a 2.5× zoom of the central region of Figure 5.2, presented to highlight the AMR used to resolve the spherical stars and winds, and the wind-wind collision shock.
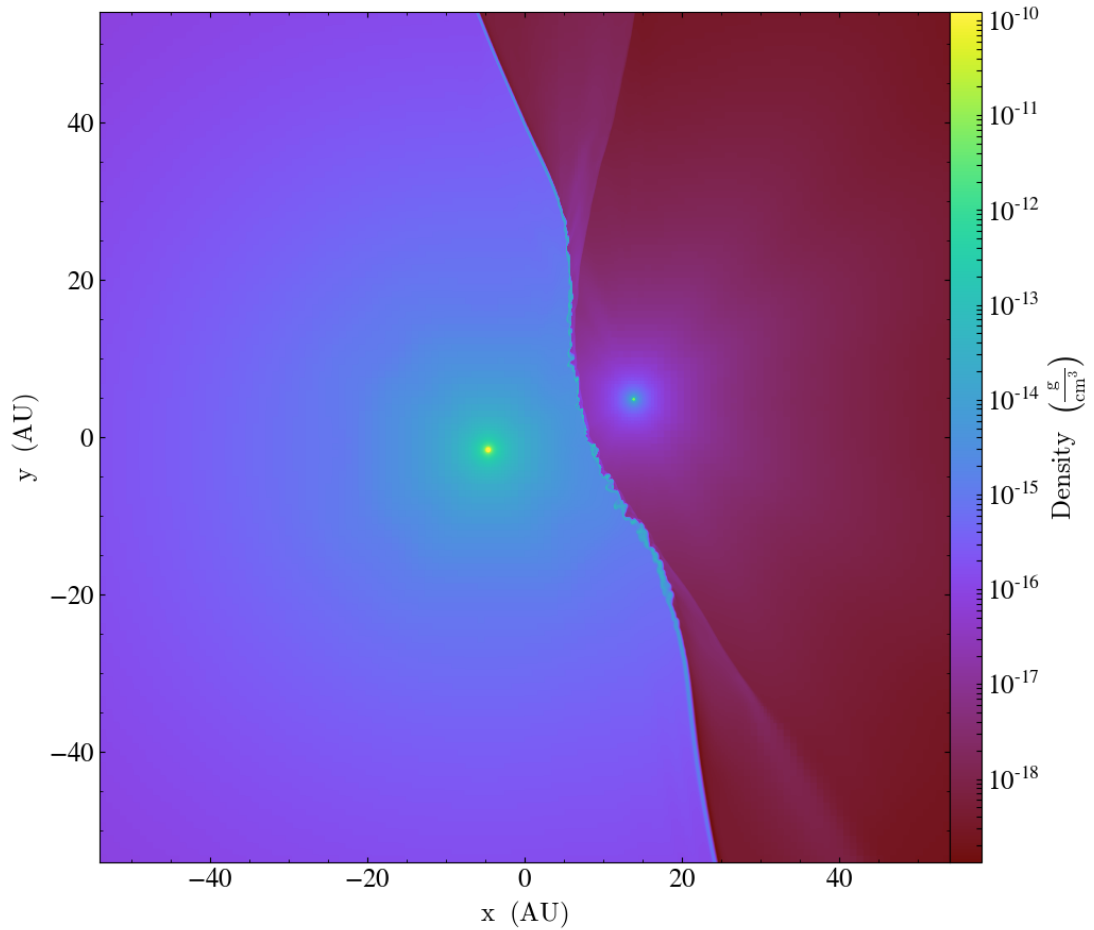
Figure 5.1: Density (color, log scale, cgs units) in the orbital xy plane at a time shortly after the start of our 3D simulation of η Car ($\phi \approx 0.80$). The discontinuity in density and wind-wind collision shock are visible between the stars in the center of the figure. The cubic domain side length is set to 108.15 AU ($7a$), with a base grid resolution of 128^3 cells and up to four additional levels of grid refinement (effective resolution of 2048^3 cells). See text for details.
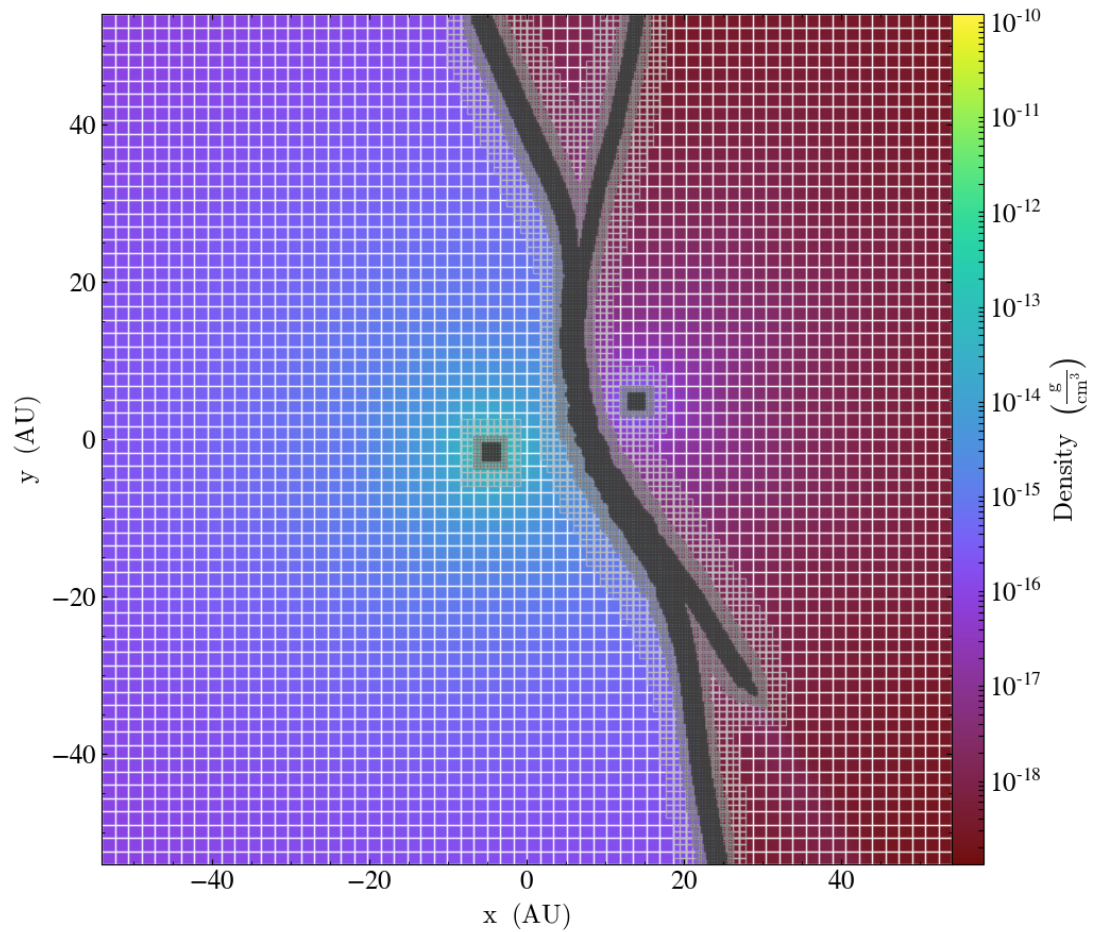
Figure 5.2: Same as Figure 5.1, but with the AMR mesh grid lines overlaid. With strong density gradients over and near the wind collision zone, the grid resolution is automatically increased by up to four additional levels in order to properly resolve the shock and any physical instabilities. Further away from the wind collision zone and the stars is the base-level coarse grid where AMR is not needed due to the lack of any strong density gradients.
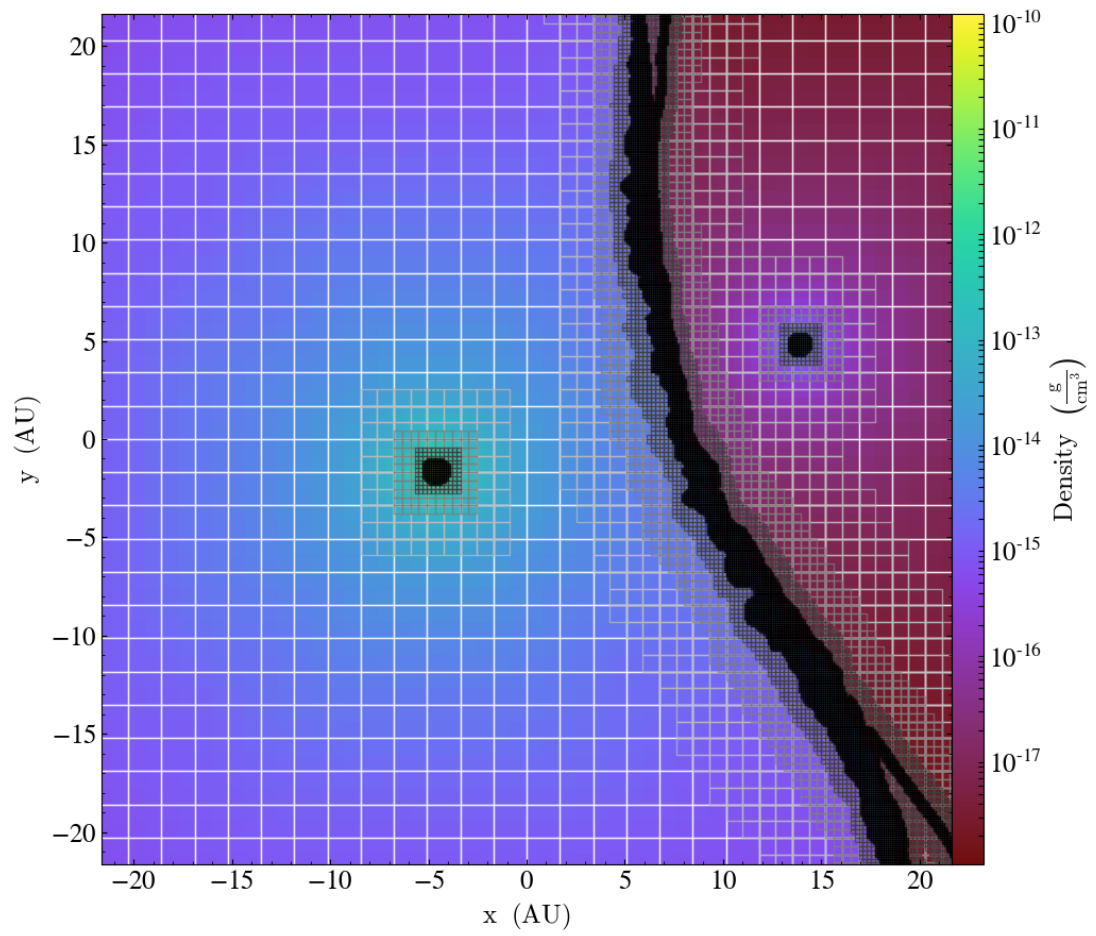
Figure 5.3: Same as Figure 5.2, but zoomed in by a factor of 2.5× in order to highlight the AMR used to resolve the spherical stars and winds, and the wind-wind collision shock between the stars.

CHAPTER 6
RESULTS

6.1   Results in the Orbital xy Plane

The figures presented in this chapter show the results of our 3D time-dependent, grid-based AMR simulation of η Car around periastron. We begin by discussing slices from the simulation showing the orbital xy plane (i.e., slices through the center of the simulation at $z = 0$) at different specific orbital phases, ϕ, before, during, and after periastron in the system's 5.54-year orbit. Slices through the simulation in the other coordinate planes perpendicular to the xy plane (the xz and yz planes) at the same times are shown and discussed in the next section. The chosen orbital phases we discuss are $\phi = 0.900, 0.950, 0.980, 0.985, 0.990, 1.00,$ 1.010, 1.020, 1.030, and 1.040, with each phase presented in sequential order (Figures 6.1 through 6.5). These phases were specifically chosen so that the results of this simulation could be directly compared to results from past 3D simulations performed using entirely different methods (e.g., Madura et al. 2013). The spatial range of each plot spans the entire computational domain of $\pm 3.5a$ (± 54.075 AU) about the origin in both the x and y directions. For the remainder of this thesis, we will refer to the more massive and more luminous primary star as η_A, and to the less massive and less luminous companion star as η_B. Wind densities (ρ), distances (d), temperatures (T), wind velocities (v), and other parameters of interest associated with a particular star will use the same corresponding η_A or η_B subscript (e.g., the primary's mass-loss rate would be $\dot{M}_{\eta_A}$).

For each phase, we present plots of density ($\log_{10}$ scale), temperature ($\log_{10}$ scale), and magnitude of the wind velocity (linear scale). As a general note for the reader, we note the appearance of apparent "square-like" artifacts located around

η_B in the plots of the temperature. Further investigation revealed that these are due to the changes in resolution between the different levels of grid refinement around η_B, and the chosen base grid resolution of the simulation. We find that this issue is easily solved by simply increasing the base grid resolution of the simulation from 128^3 cells to 512^3 cells. However, due to time and computational resource constraints, a completely new simulation using this higher base grid resolution was not possible before completing this thesis. Nevertheless, we note that these small artifacts are limited to the downstream non-shock side of η_B's wind, which is not the primary focus of this work. Artifacts are generally not present on the shock side of η_B's wind or in/near the wind-wind collision interface due to the fact that the AMR scheme keeps the resolution in these regions at the maximum level of refinement throughout the simulation. Thus, any effects on the results of this work or their interpretation due to these artifacts in the temperature plots are expected to be negligible. This is supported by the lack of any artifacts in plots of the density or magnitude of the wind velocity. Future simulations will use a higher base resolution to ensure the elimination of any such grid artifacts.

Key features can be seen at the early phases of $\phi = 0.900$ and 0.950 in Figure 6.1. A distinct line cuts through the center of the plots representing the WWC zone where the winds meet. The primary η_A and its dense wind can be recognized on the left $(-x)$ side, while the secondary η_B and its lower-density wind is located on the right $(+x)$ side. The WWC zone opens to the right with the apex pointing towards η_A, as expected. η_B is positioned to the other side of the apex. The WWC shock zone can be seen as the result of the momentum balance at the contact discontinuity (CD). As seen in (Canto et al. 1996) and previous simulations making use of smoothed particle hydrodynamics (SPH; Madura et al. 2013), the initial shift in momentum balance and the overall conical shape of the WWC region (due to the

slower orbital speeds compared to the η_A wind terminal speed) are consistent in this AMR simulation. Past SPH simulations show a measured half-opening angle of $\approx 55°$, while the half-opening angle of the AMR simulation is $\approx 60°$.

A clear bow shock forms as a result of the η_B wind forming a lower-density cavity in η_A's denser mass outflow. Differences in wind densities between the two stellar winds in our AMR simulation are consistent with past SPH simulation results in (Madura et al. 2013). Temperatures in the shocks at the WWC zone also range approximately four orders of magnitude, with density-enhanced portions of the post-shock η_A wind having $T \lesssim 10^4$ K, while the hot post-shock η_B wind near the apex of the WWC zone reaches $T \approx 10^8$ K. These temperatures are consistent with those obtained from X-ray observations of η Car. Along the arms of the shock cone the temperature of the colliding winds is lower, since the WWC is not as directly head-on and thus is less efficient at thermalizing the flow (Madura et al. 2013).

At phases $\phi = 0.900$ and 0.950, the wind velocities of each star follow the expected β-velocity law, reaching terminal velocity at the WWC zone with $v_{\eta_A} \approx 0.5 \times 10^8$ cm s^{-1} and $v_{\eta_B} \approx 3 \times 10^8$ cm s^{-1}. The trailing arm of the η_B shock shows slower velocities $v_{\eta_B} \approx 2 \times 10^8$ cm s^{-1} and lower temperatures. The slowing wind velocity is consistent with discussions in Owocki (2005) and Vink (2012) as velocity begins to decrease due to overall energy loss.

Orbital velocity eventually contributes to the increasing spiraling shape of the WWC zone and η_B's nested wind cavity as orbital phase increases. The degree of downstream curvature of the WWC region is determined by the ratio of the orbital speed to the pre-shock wind speed (Madura et al. 2013). As the stars approach periastron, the orbital speed of η_A relative to η_B increases to a value near its wind terminal speed. This leads to a gradual, but eventual strong distorting of the WWC zone (Figure 6.2). The increasing orbital speeds also cause the post-shock η_B wind

in the leading arm of the WWC zone to be heated to higher temperatures than the gas in the trailing arm, as seen in our simulation. Radiative effects also clearly play a role in determining the temperatures in the shocks, following the $\chi = t_{cool}/t_{escape}$ parameter (see Stevens et al. 1992). For η_A's slower and higher-density post-shock wind, $\chi \ll 1$, compared to η_B's much faster and lower-density post-shock wind where $\chi > 1$. The post-shock η_B wind therefore cools adiabatically and remains hot, whereas η_A's post-shock wind is highly radiative and cools extremely quickly.

At $\phi = 0.980$ and $\phi = 0.985$ (Figure 6.2), there is a progression in the changing position as both stars move towards each other down to a stellar separation $d \approx 5$ AU. The apex of the WWC zone also continues to move closer to each star while the trailing colliding winds begin to decrease in opening angle at about 45° and 40°, respectively, at each phase. As the stars move closer, instabilities in the WWC zone arise. These were somewhat visible in Figure 6.1, but they become more visible as the system moves towards periastron. Since the winds collide at different velocities, at the CD there is a velocity sheer that can cause Kelvin-Helmholtz (KH) instabilities. The extremely-rapidly-cooling, dense, thin and radiative post-shock η_A wind is also subject to non-linear thin-shell instabilities (NTSI). Both instabilities have also been described in past SPH simulations, as seen in (Madura et al. 2013), but they are much clearer and significantly more highly resolved in these new AMR simulations. The time scale for exponential growth of KH instabilities is proportional to $\sqrt{\rho_1\rho_2}/(\rho_1 + \rho_2)$, where ρ_1 and ρ_2 are the different values of the density on either side of the CD (Stevens et al. 1992; Madura et al. 2013). For the NTSI, the stability of the dense shell depends on the shell's thickness, with thicker, denser shells typically less prone to the NTSI (Madura et al. 2013).

The separation between the stars at $\phi = 0.980$ (5 AU) is small enough that η_B's wind collides with η_A's wind before the η_B wind has reached its terminal speed.

The lower pre-shock η_B wind speed moves the WWC apex closer to η_B. The lower pre-shock wind speed and shorter distance between the star and the CD causes the η_B shock to heat to lower temperatures (compared to earlier phases). The shorter distance to the shock also increases the η_B wind density. As a result, the cooling parameter χ for the η_B wind near the WWC apex drops to a value of ~ 2. The most important factor responsible for this decrease in the value of χ is the decrease in the pre-shock η_B wind speed, since $\chi \propto v_{\text{wind}}^4$. The post-shock temperature of the η_B wind at the WWC apex is thus reduced. This is clearly visible in the simulation for the hottest gas between the stars, which was $\sim 10^8$ K at $\phi = 0.900$, but is only on the order of $\sim 10^7$ K at $\phi = 0.980$ and 0.985. The lower pre-shock η_B wind speed also changes the wind momentum ratio and decreases the opening angle of the WWC shock cone. The trailing wind of η_B also collides with the η_A wind at a more oblique angle in the trailing arm of the WWC region. The asymmetry in temperature between the leading and trailing arms of the WWC shock on the η_B side becomes more apparent, with the leading arm having much hotter gas than the trailing arm.

The increasing orbital speeds as the system progresses towards periastron distorts the WWC region and eventually produces a spiral WWC zone as the binary pair moves in a counter clockwise motion at each step. At phases $\phi = 0.990$ and $\phi = 1.000$ (Figure 6.3), the stars are extremely close. The stellar separation at periastron is only 1.54 AU. In addition to the sudden shift in the stellar positions there is a rapid shift in the location of the WWC apex, which is now located on the back side of η_A directly opposite in direction to where it would be located at apastron. The pre-shock η_B wind speed is reduced even further, drastically changing the WWC opening angle and moving the apex closer to the stars. By phases $\phi = 0.990$ and 1.000, the cooling parameter χ has dropped below 1 and the

post-shock η_B wind switches from adiabatic to radiative cooling. This is clearly seen in the WWC zone at $\phi = 1.000$, where there is no longer any hot gas located near the apex of the WWC zone. The post-shock η_B wind now has temperatures $< 10^4$ K around the WWC apex or is entirely gone. This is sometimes referred to as a "collapse" of the WWC apex region (Madura et al. 2013). Only the backside of η_B that points away from η_A is able to drive a steady wind, leading to a cooler WWC leading arm, and a trailing arm that is slowly cooling adiabatically and vanishing since the η_B wind can no longer collide downstream with η_A's wind due to the strong distortion of the WWC region caused by the rapid orbital motion.

Meanwhile, the spiraling effect begins to appear at periastron as the lower-density, faster wind of η_B cuts through the higher-density, slower η_A wind. A lower-density cavity forms within the η_A wind trailing to the $-x$ side that will continue to expand as the stars complete periastron passage. Further out in the $+x$ direction velocity sheering has a greater effect as the KH instability increases, while on the $-x$ side these effects are not as great. At the apex of the WWC zone, the density is at its greatest, reaching $> 10^{-12}$ g cm^{-3}.

Following periastron, at phases $\phi = 1.010$ and 1.020 (Figure 6.4), the after effects of rapid orbital motion become increasingly more pronounced. The wind of η_B carves a low-density spiral cavity in η_A's wind. This cavity moves in the $-x$ and $-y$ directions following periastron. The higher-velocity η_B wind in the cavity also continuously rams into the denser, slower η_A wind that moves in the $-x$ and $-y$ directions. Due to the large difference in density between the two winds, and because the η_B wind is colliding and accelerating the slower, receding η_A wind, thin-shell and Rayleigh-Taylor (RT) instabilities are created that greatly distort the spiral WWC region as it moves in the $-x$ direction. Large radial protrusions or "fingers" of low-density η_B wind penetrate into the η_A wind as a result of these

instabilities, as originally noticed by (Madura et al. 2015). Hot, shock-heated η_B gas fills the fingers.

The opening of the apex increases in angle as the momentum balance shifts with the change in orbit. The half-opening angle has now widened. At $\phi = 1.010$ and 1.020, on the $+x$ side, the η_A wind starts to flow to fill the low-density cavity left behind by η_B that it formed prior to periastron. This is easily seen in the plots of velocity on the $+y$ side of the system. The magnitude of η_A's wind velocity increases with radius in the $+x$ and $+y$ directions to a value well above it's normal wind terminal speed, up to $\sim 2 \times 10^5$ cm s^{-1}, as the denser wind expands to fill the void left behind by η_B's lower-density wind. Near the WWC apex, the temperature of the dense wind of η_A continues to remain low. As η_B starts to reestablish its wind as the orbital separation increases after periastron, the conical WWC shape begins to return, as does hotter shocked gas. The post-shock η_B wind returns to $T \sim 10^8$ K near the WWC apex at phases around 1.020.

Figure 6.5 shows our final orbital phase snapshots from the simulation at $\phi = 1.030$ and 1.040. The orbital velocity has decreased to the point where η_B's wind and the WWC zone have started to fully reappear. The opening angle widens as the momentum balance changes with both stars moving further apart. The WWC apex now has shifted away from η_A as the apex widens. The lower-density cavity carved by η_B's faster wind opens up along the $+x$ side with a circular radius of $R \approx 40$ AU. The magnitudes of the RT instabilities in the receding η_A wind around the edge of the new circular η_B wind cavity have increased noticeably. Hot shocked gas exists within the finger-like cavities created by the instabilities, and at the apex of the WWC zone. The temperature of the hottest gas located at the apex between the stars is now again at $T \gtrsim 10^8$ K. As the system moves slowly back towards apastron, orbital speeds gradually decrease and the WWC zone and η_B

wind cavity regain their axisymmetric conical shape. Features present in the winds at $\phi = 1.040$ also gradually expand outward as the system moves back towards apastron, with the whole process repeating every 5.54-years.

6.2   Results in the xz and yz Planes

Figures 6.6 through 6.10 show slices in the xz plane, while Figures 6.11 through 6.15 show slices in the yz plane, from our 3D simulation. The z coordinate measures distance above $(+)$ and below $(-)$ the orbital plane, while the x coordinate is along the orbital semimajor axis, and y is along the orbital semiminor axis. The layout of the figures, quantities plotted ($\log_{10}$ density, $\log_{10}$ temperature, velocity magnitude), and orbital phases shown are identical to Figure 6.1 through 6.5 above. The focus here is on some of the most apparent features along other planar slices so that the reader can better appreciate the 3D structure of the colliding winds.

The xz-plane slices show η_A's wind starting on the $-x$ side and η_B's wind on the $+x$ side of the system, more deeply embedded behind a dense layer of gas. Moving towards periastron, there is an apex with a wide opening angle showing the momentum balance along this line of sight. Gas throughout the WWC zone is heated to $T \approx 10^7$ K and above, but cools as the system approaches periastron. Similarly, velocity magnitudes have reached their terminal values as the faster, low density wind of η_B begins to shear the denser, slower wind of η_A and KH instabilities take effect. Moving through periastron, radiative cooling takes over in the post-shock η_B wind and the temperature around the WWC apex drops. A low-density cavity of η_B wind appears in the $-x$ region of the plots and expands as the system moves away from periastron. As both stars approach post-periastron, the lower-density cavity of η_B's wind begins to radiate from the center outwards in the plane of view. On the $-x$ side, the shocked gas begins to cool. An outline of the

Figure 6.1: Shown here are the orbital phases at $\phi = 0.900$ (top row) and 0.950 (bottom row) along a slice of the orbital plane. Color shows from left to right, density (log scale), temperature (log scale), and magnitude of velocity (linear scale). The domain size represented in each plot are at ± 50 AU with each tick mark representing ± 5 AU

Figure 6.2: Shown here are the orbital phases at $\phi = 0.980$ (top row) and 0.985 (bottom row) along a slice of the orbital plane. Color shows from left to right, density (log scale), temperature (log scale), and magnitude of velocity (linear scale). The domain size represented in each plot are at ±50 AU with each tick mark representing ±5 AU
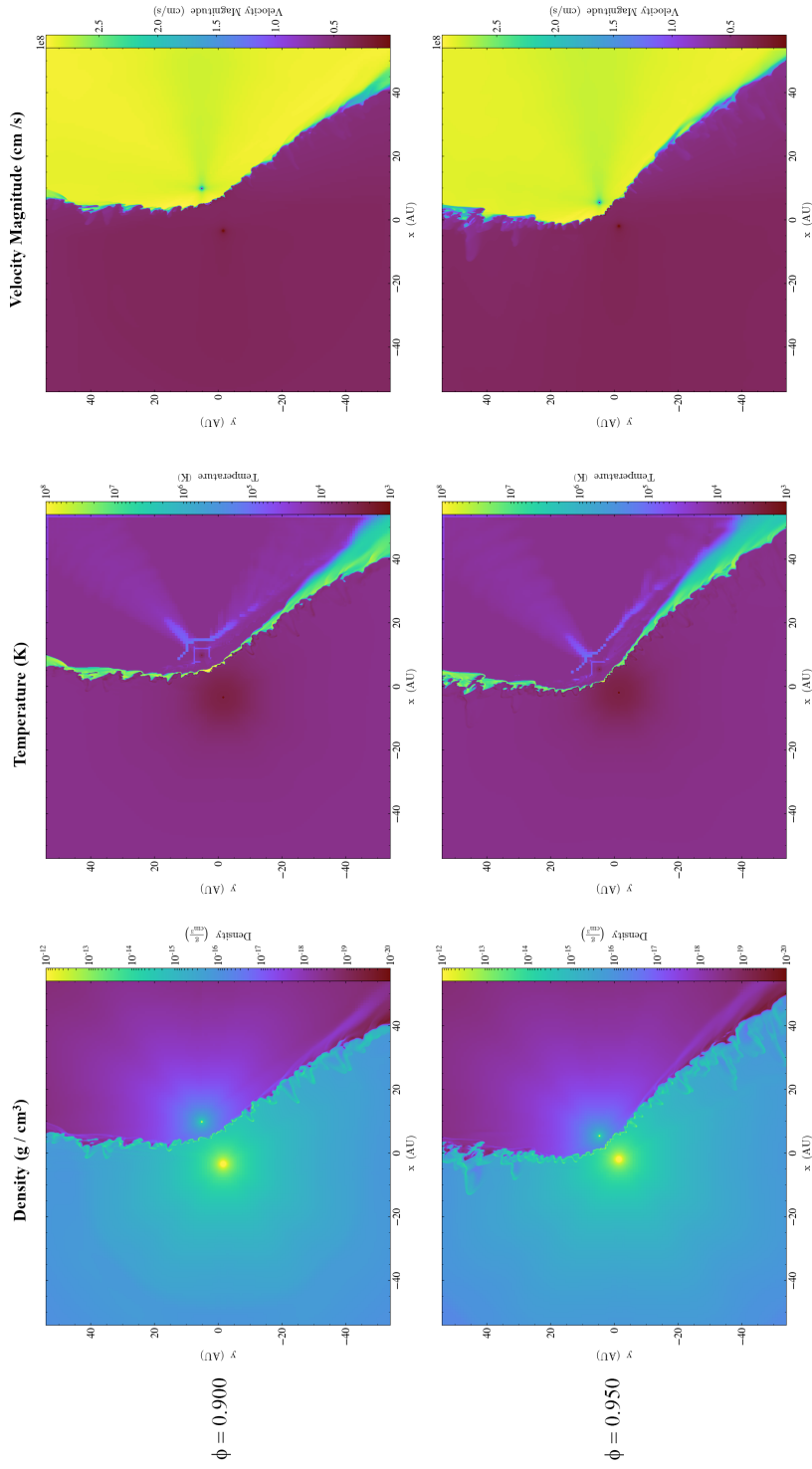
Figure 6.3: Shown here are the orbital phases at $\phi = 0.990$ (top row) and 1.000 (bottom row) along a slice of the orbital plane. Color shows from left to right, density (log scale), temperature (log scale), and magnitude of velocity (linear scale). The domain size represented in each plot are at ± 50 AU with each tick mark representing ± 5 AU

Figure 6.4: Shown here are the orbital phases at $\phi = 1.010$ (top row) and 1.020 (bottom row) along a slice of the orbital plane. Color shows from left to right, density (log scale), temperature (log scale), and magnitude of velocity (linear scale). The domain size represented in each plot are at ± 50 AU with each tick mark representing ± 5 AU
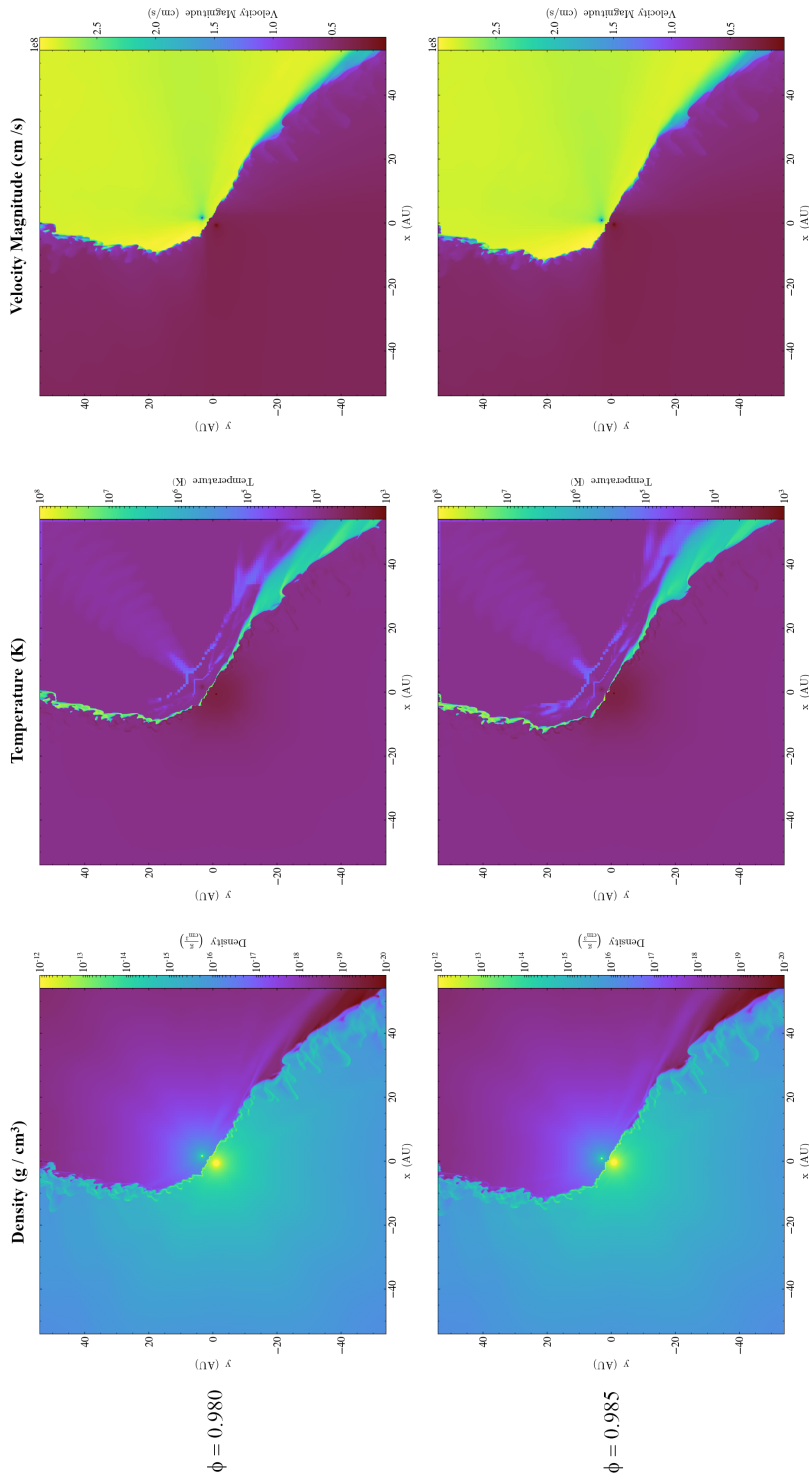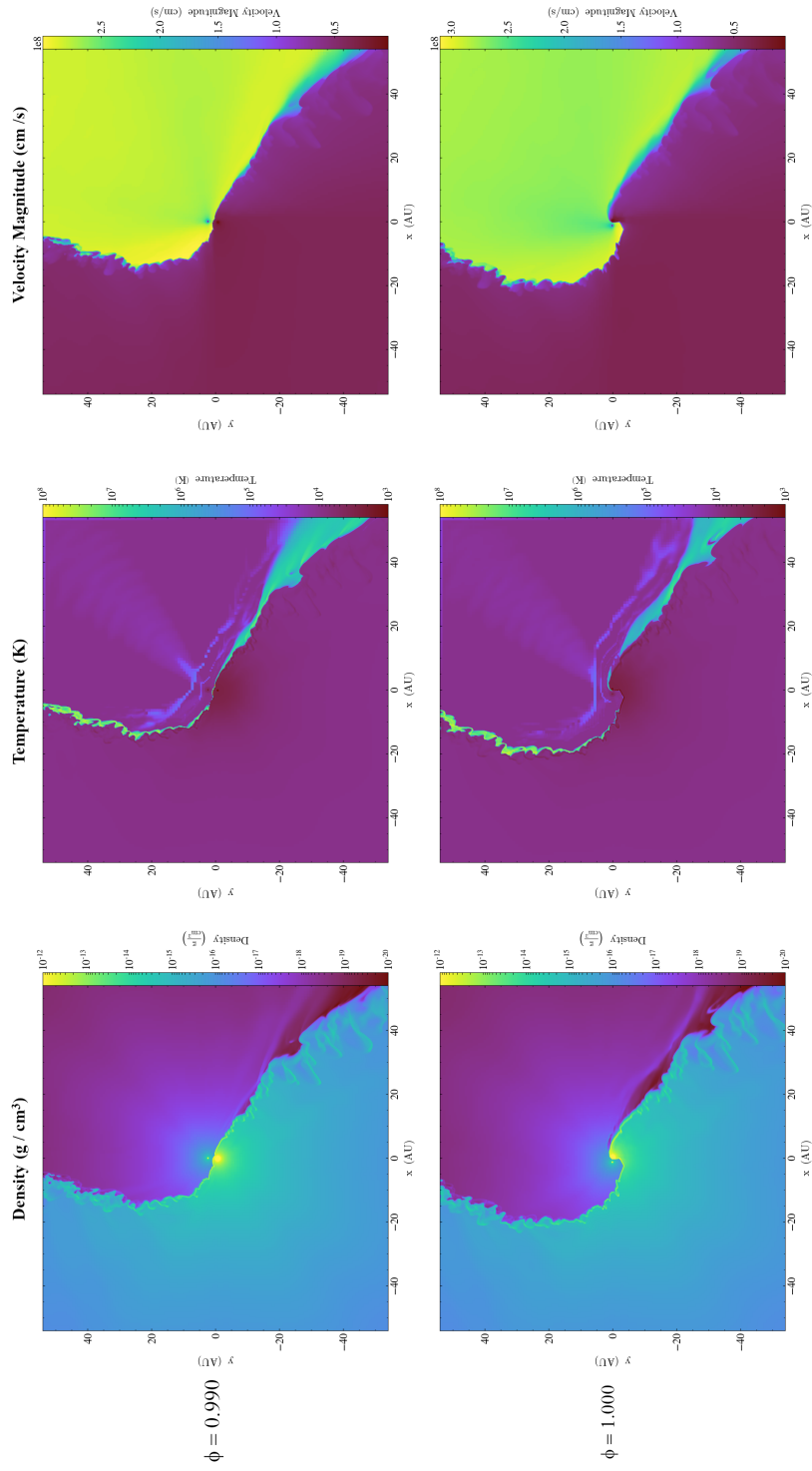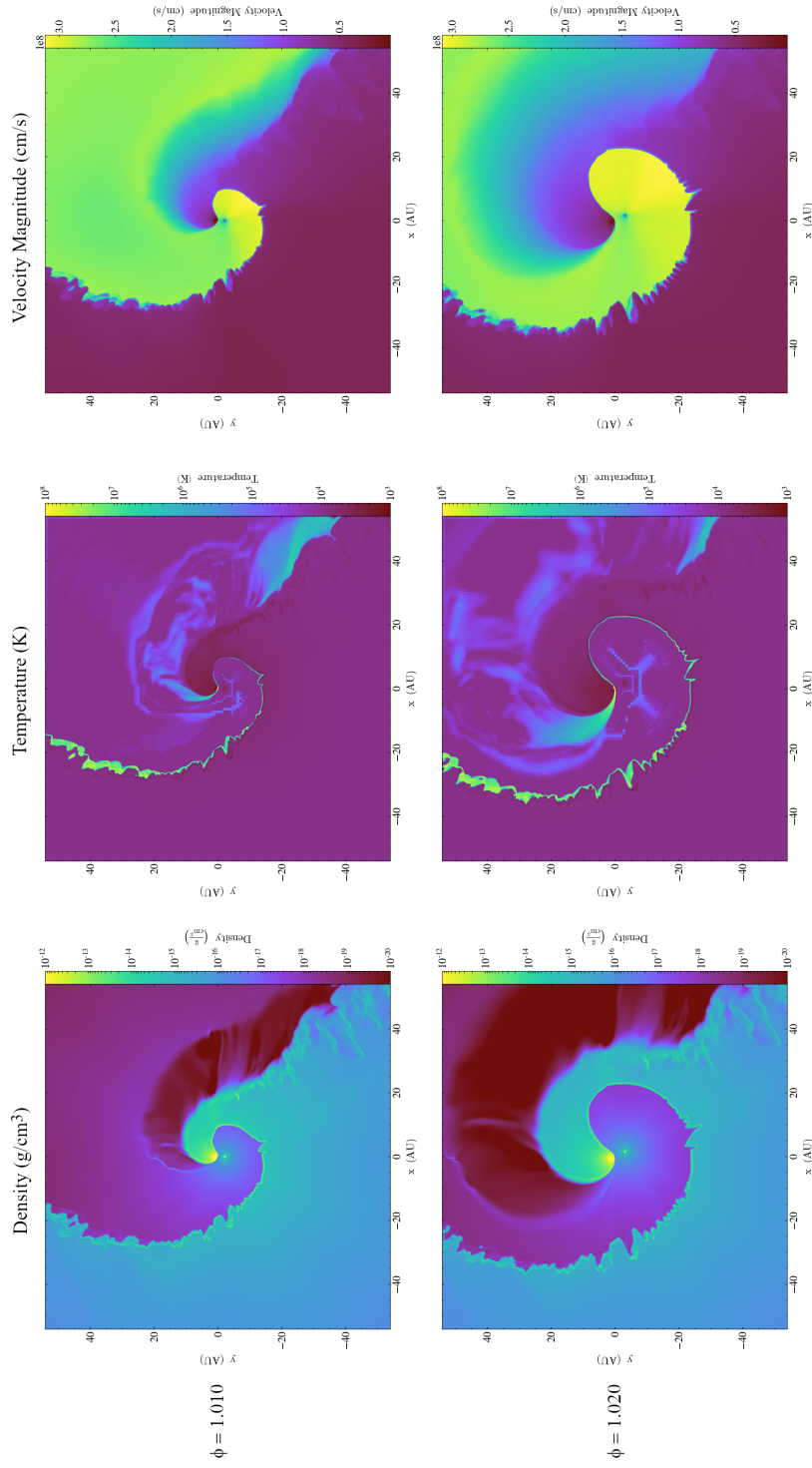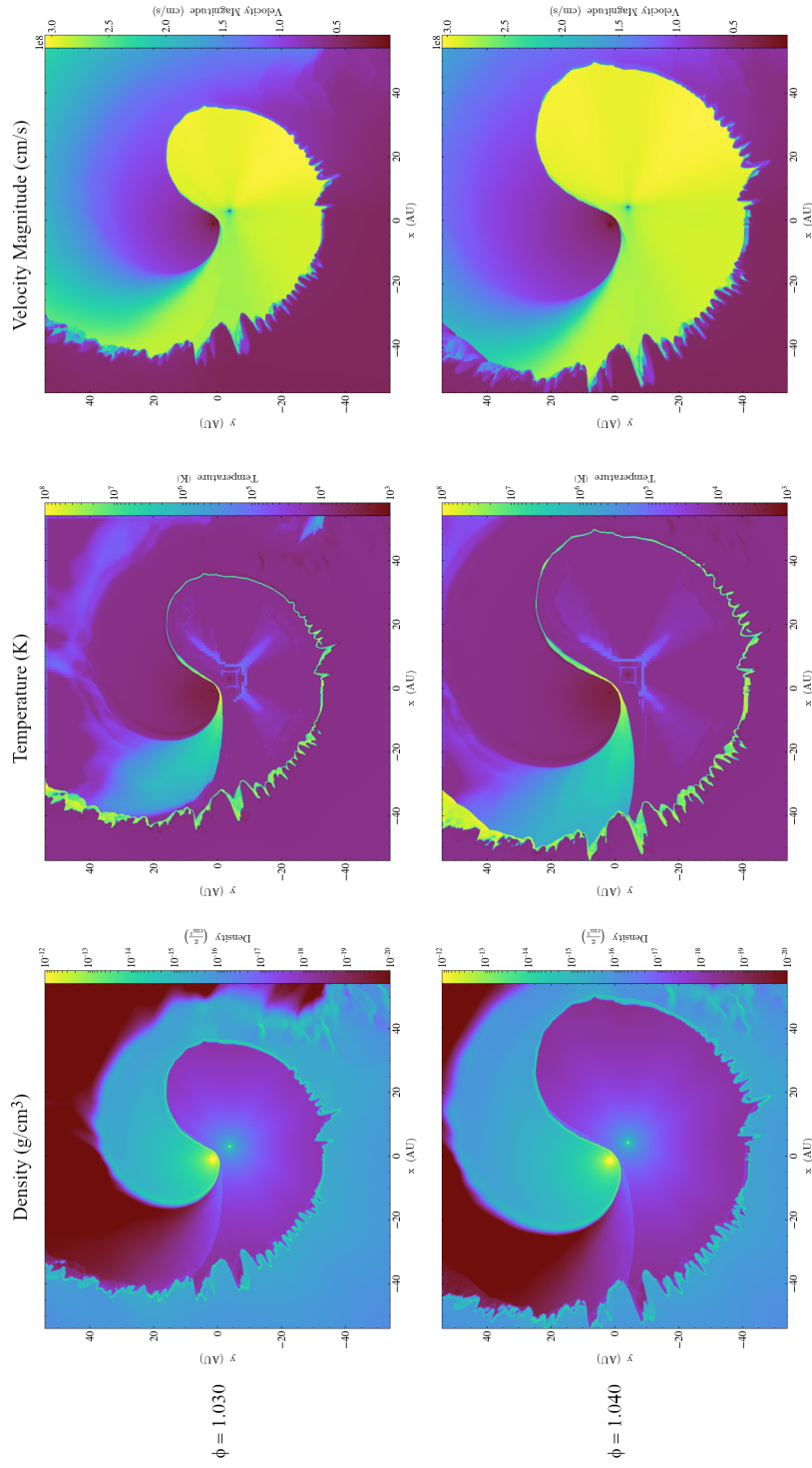
Figure 6.5: Shown here are the orbital phases at $\phi = 1.030$ (top row) and 1.040 (bottom row) along a slice of the orbital plane. Color shows from left to right, density (log scale), temperature (log scale), and magnitude of velocity (linear scale). The domain size represented in each plot are at ± 50 AU with each tick mark representing ± 5 AU

CD shows the high temperature of the heated gas at incredible distances near ± 40 AU from the center. At later phases after periastron, the hot WWC region is reestablished and fingers in the dense η_A wind in the $-x$ region of the plot, caused by RT instabilities, are visible.

In contrast to the xz-plane, the yz plane slices show the movement of the leading and trailing arms of the WWC zone around periastron (i.e., the leading and trailing arms pass through this plane as the system moves through periastron). The curvature of the WWC zone in the plane of view up to periastron at phase $\phi = 1.000$ increases in angle with shearing effects at the upper $+z$ and lower $-z$ trailing arms. After periastron, η_A briefly appears on the $+y$ side eclipsing η_B. Here the lower density region forms on the right side of $+y$ with the higher density regions of η_A following through. Sharp protrusions form at the WWC from the wake η_B leaves behind, each filled with heated gas. Changes in temperature near the WWC apex are very apparent as the system moves through periastron, with a notable absence of any hot material at the WWC apex at periaston. Reestablishment of the η_B wind and hot WWC zone after periastron are also easily seen, as are the fingers in η_A's wind caused by RT instabilities. Changes in velocity magnitude appear as expected as the arms of the WWC region pass through the yz plane around periastron.

Figure 6.6: Shown here are the orbital phases at $\phi = 0.900$ (top row) and 0.950 (bottom row) along a slice of the xz-plane. Color shows from left to right, density (log scale), temperature (log scale), and magnitude of velocity (linear scale). The domain size represented in each plot are at ± 50 AU with each tick mark representing ± 5 AU.

Figure 6.7: Shown here are the orbital phases at $\phi = 0.980$ (top row) and 0.985 (bottom row) along a slice of the xz-plane. Color shows from left to right, density (log scale), temperature (log scale), and magnitude of velocity (linear scale). The domain size represented in each plot are at ± 50 AU with each tick mark representing ± 5 AU.

Figure 6.8: Shown here are the orbital phases at $\phi = 0.990$ (top row) and 1.000 (bottom row) along a slice of the xz-plane. Color shows from left to right, density (log scale), temperature (log scale), and magnitude of velocity (linear scale). The domain size represented in each plot are at ± 50 AU with each tick mark representing ± 5 AU.
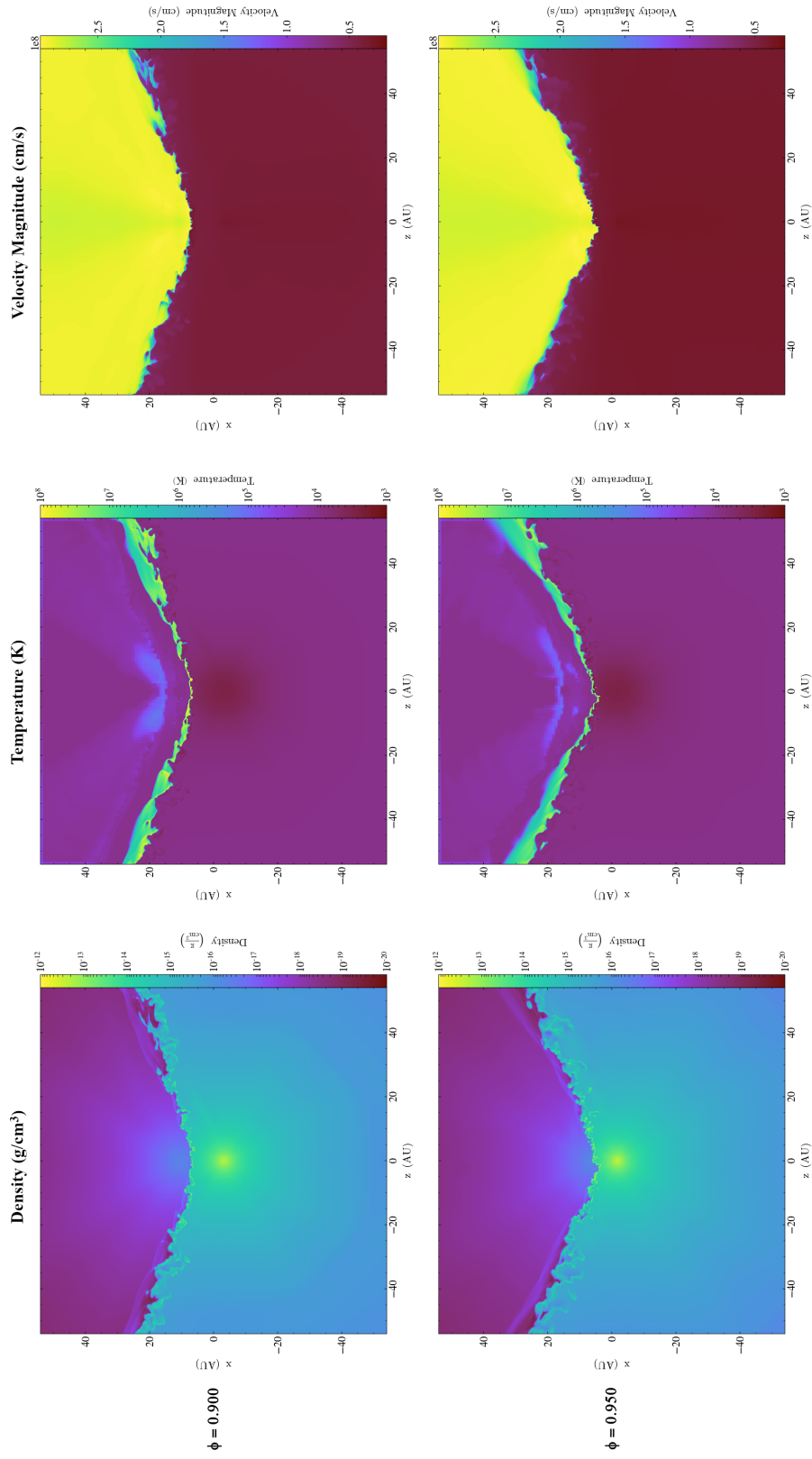
Figure 6.9: Shown here are the orbital phases at $\phi = 1.010$ (top row) and 1.020 (bottom row) along a slice of the xz-plane. Color shows from left to right, density (log scale), temperature (log scale), and magnitude of velocity (linear scale). The domain size represented in each plot are at ±50 AU with each tick mark representing ±5 AU.

Figure 6.10: Shown here are the orbital phases at $\phi = 1.030$ (top row) and 1.040 (bottom row) along a slice of the xz-plane. Color shows from left to right, density (log scale), temperature (log scale), and magnitude of velocity (linear scale). The domain size represented in each plot are at ±50 AU with each tick mark representing ±5 AU.
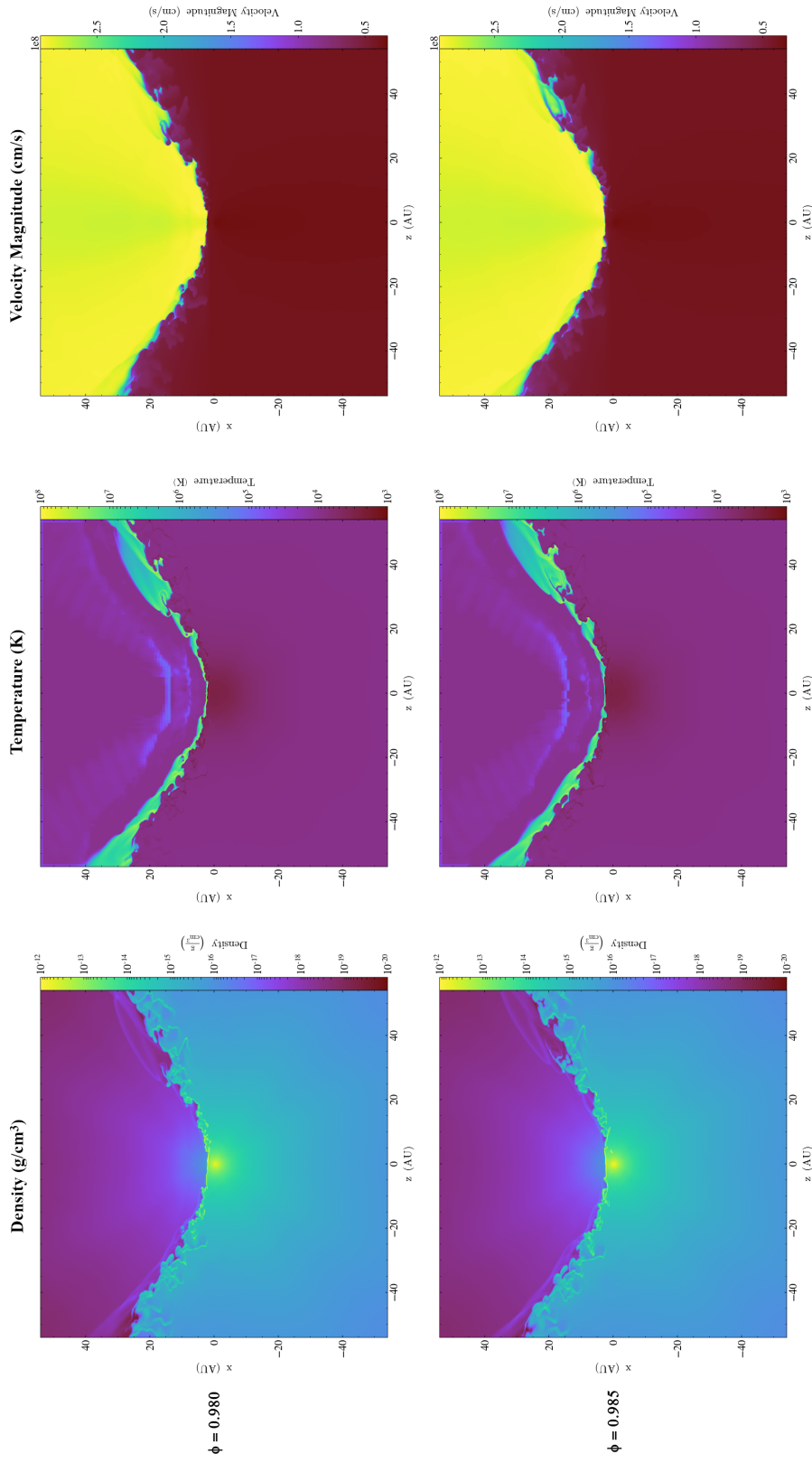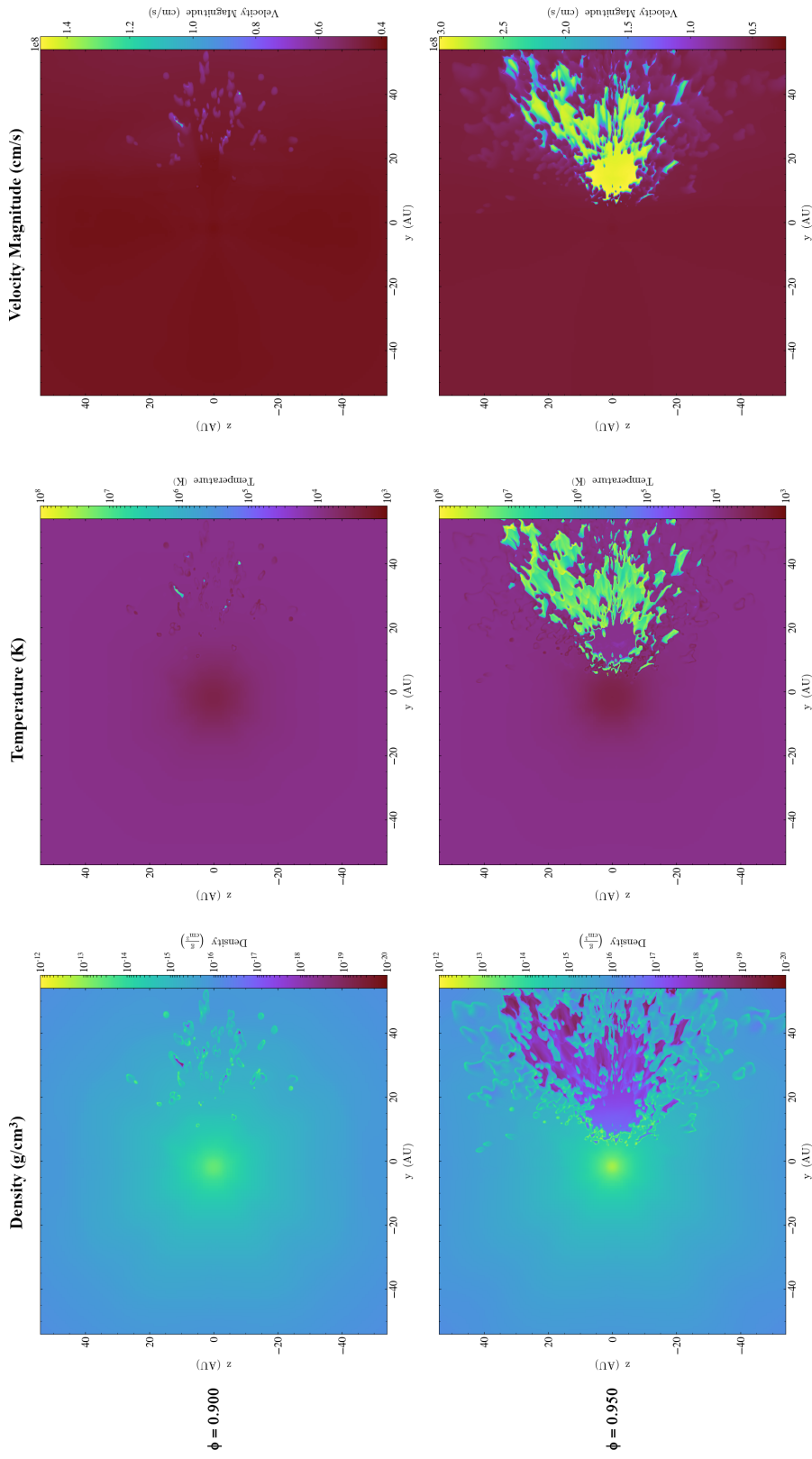
Figure 6.11: Shown here are the orbital phases at $\phi = 0.900$ (top row) and 0.950 (bottom row) along a slice of the yz-plane. Color shows from left to right, density (log scale), temperature (log scale), and magnitude of velocity (linear scale). The domain size represented in each plot are at ± 50 AU with each tick mark representing ± 5 AU.

79
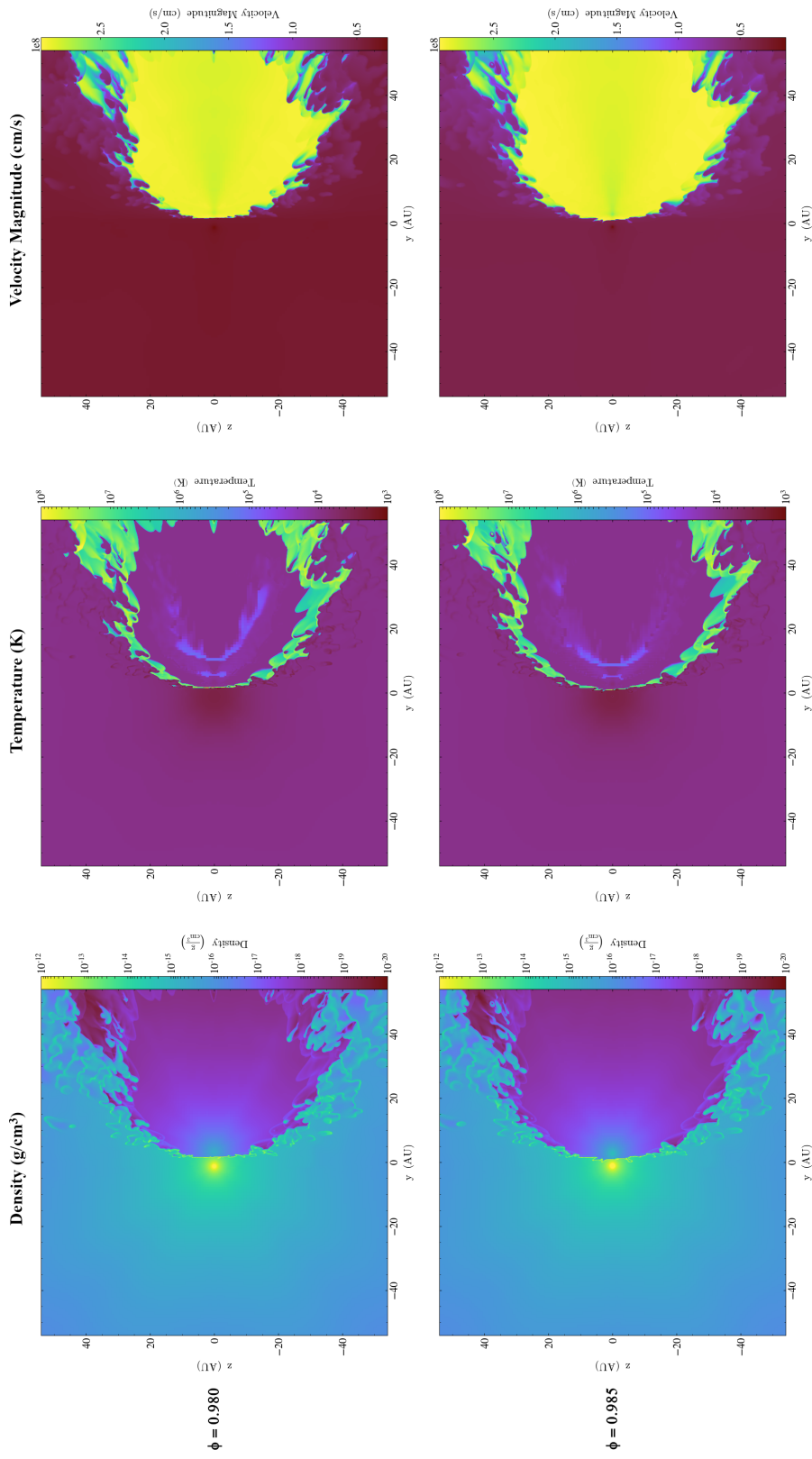
Figure 6.12: Shown here are the orbital phases at $\phi = 0.980$ (top row) and 0.985 (bottom row) along a slice of the yz-plane. Color shows from left to right, density (log scale), temperature (log scale), and magnitude of velocity (linear scale). The domain size represented in each plot are at ±50 AU with each tick mark representing ±5 AU..
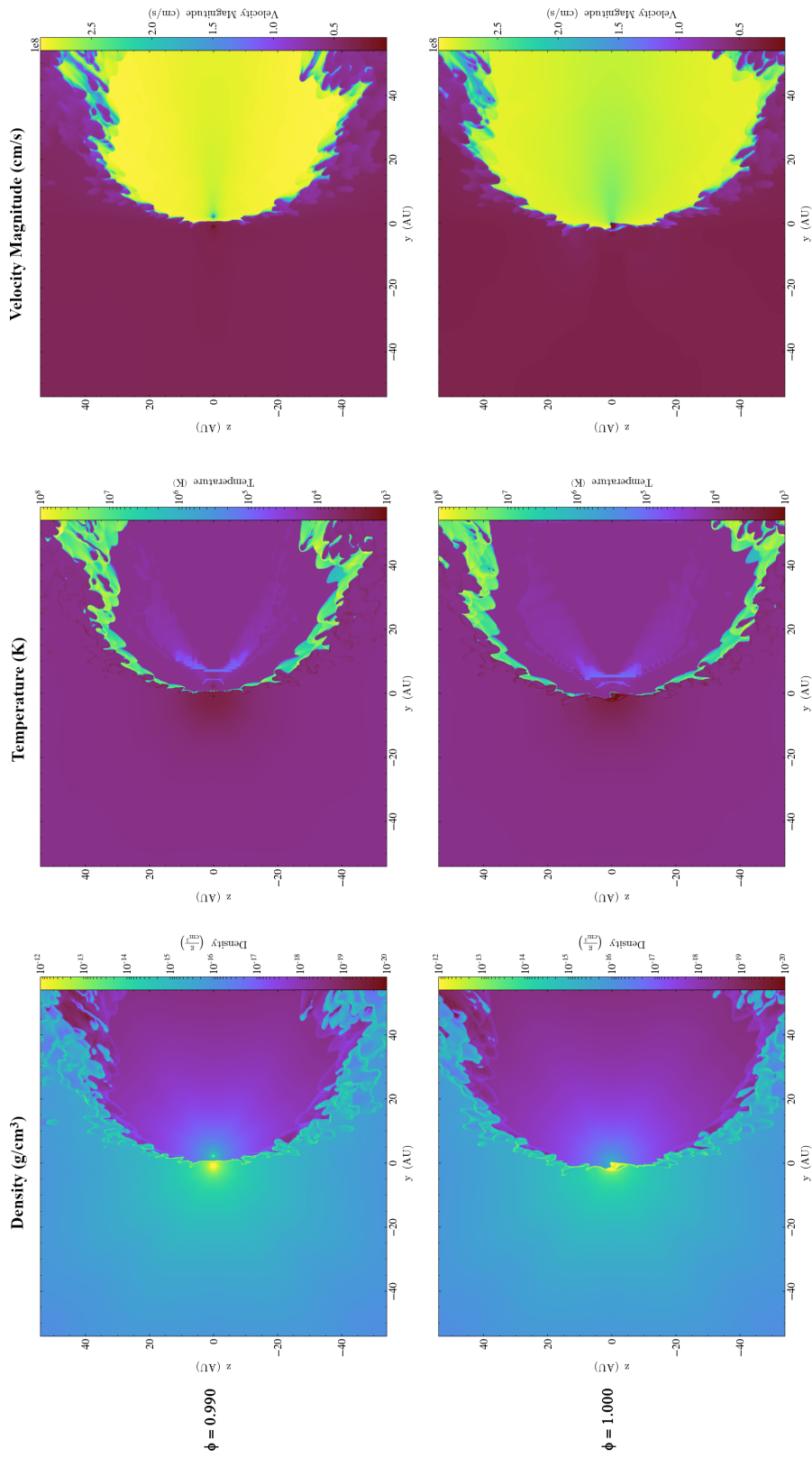
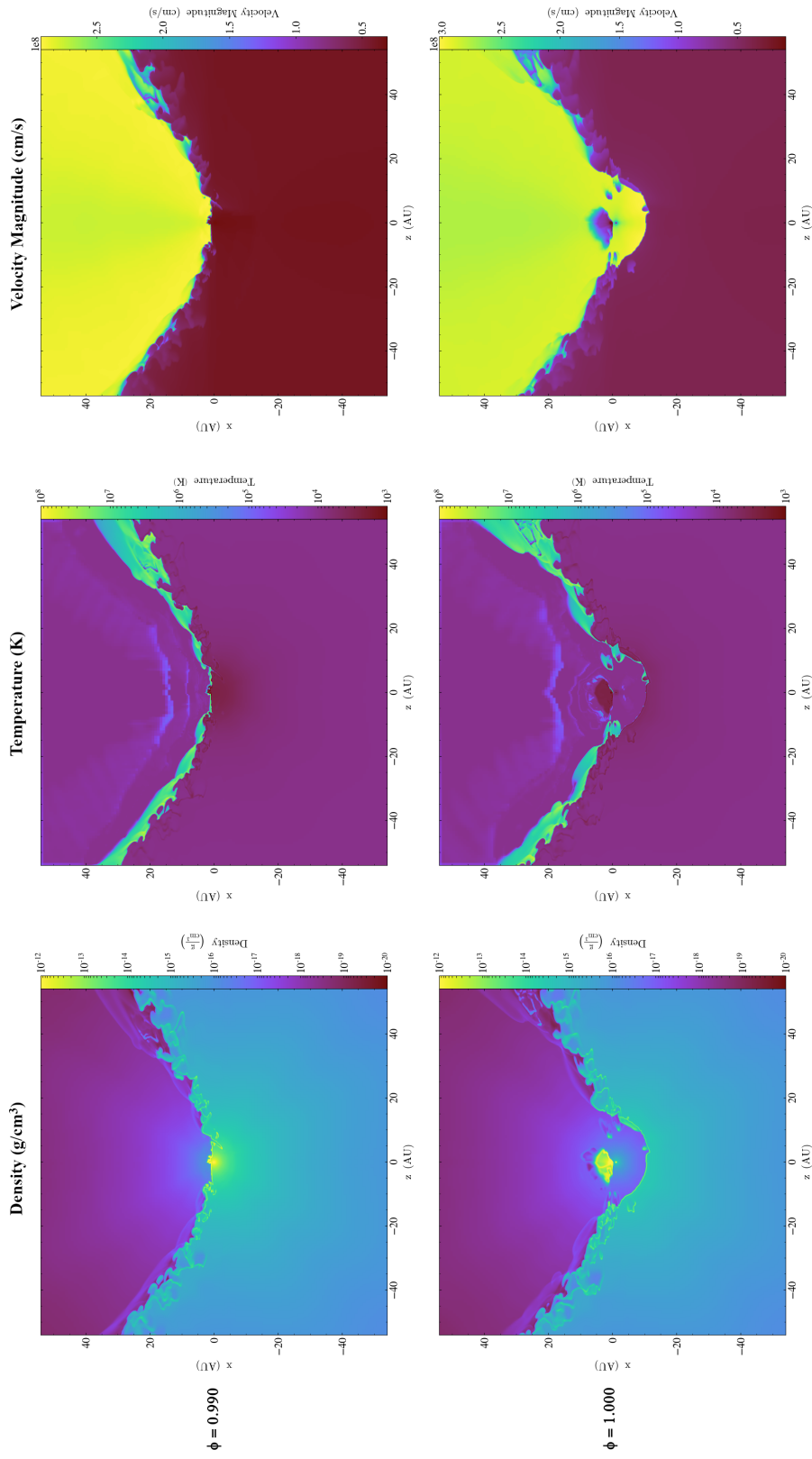Figure 6.13: Shown here are the orbital phases at $\phi = 0.990$ (top row) and 1.000 (bottom row) along a slice of the yz-plane. Color shows from left to right, density (log scale), temperature (log scale), and magnitude of velocity (linear scale). The domain size represented in each plot are at ± 50 AU with each tick mark representing ± 5 AU.
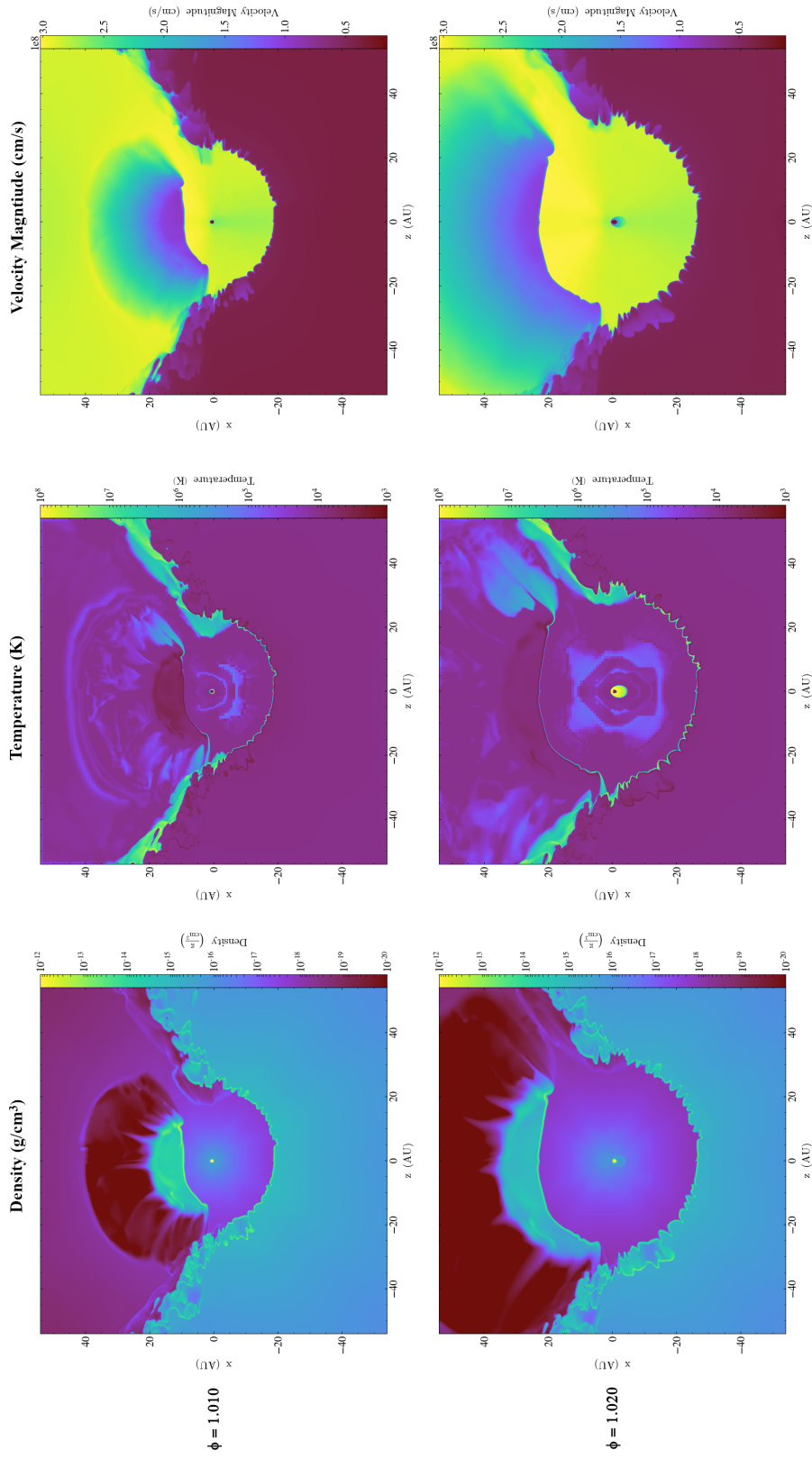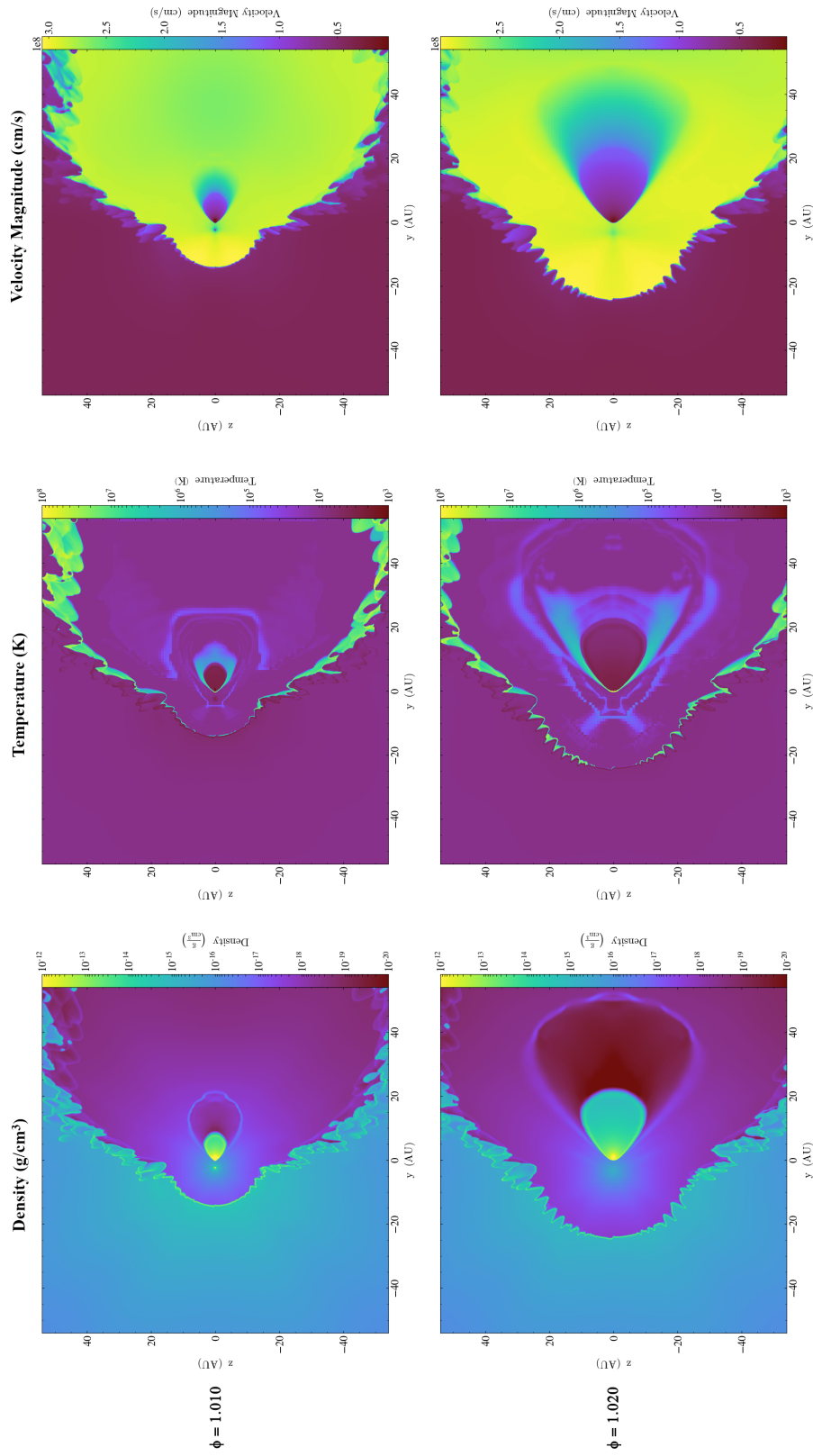
Figure 6.14: Shown here are the orbital phases at $\phi = 1.010$ (top row) and 1.020 (bottom row) along a slice of the yz-plane. Color shows from left to right, density (log scale), temperature (log scale), and magnitude of velocity (linear scale). The domain size represented in each plot are at ± 50 AU with each tick mark representing ± 5 AU.
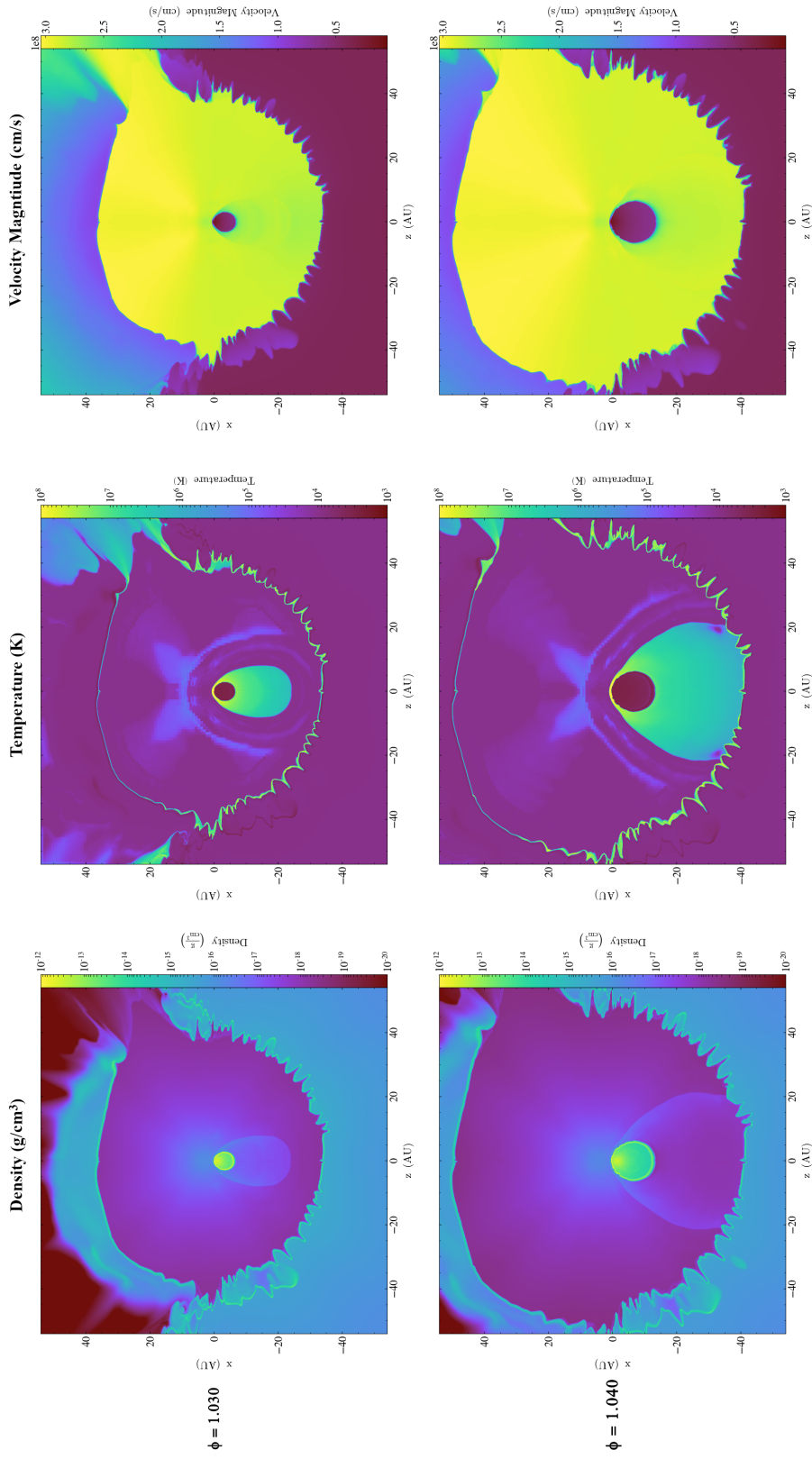
Figure 6.15: Shown here are the orbital phases at $\phi = 1.030$ (top row) and 1.040 (bottom row) along a slice of the yz-plane. Color shows from left to right, density (log scale), temperature (log scale), and magnitude of velocity (linear scale). The domain size represented in each plot are at ±50 AU with each tick mark representing ±5 AU.
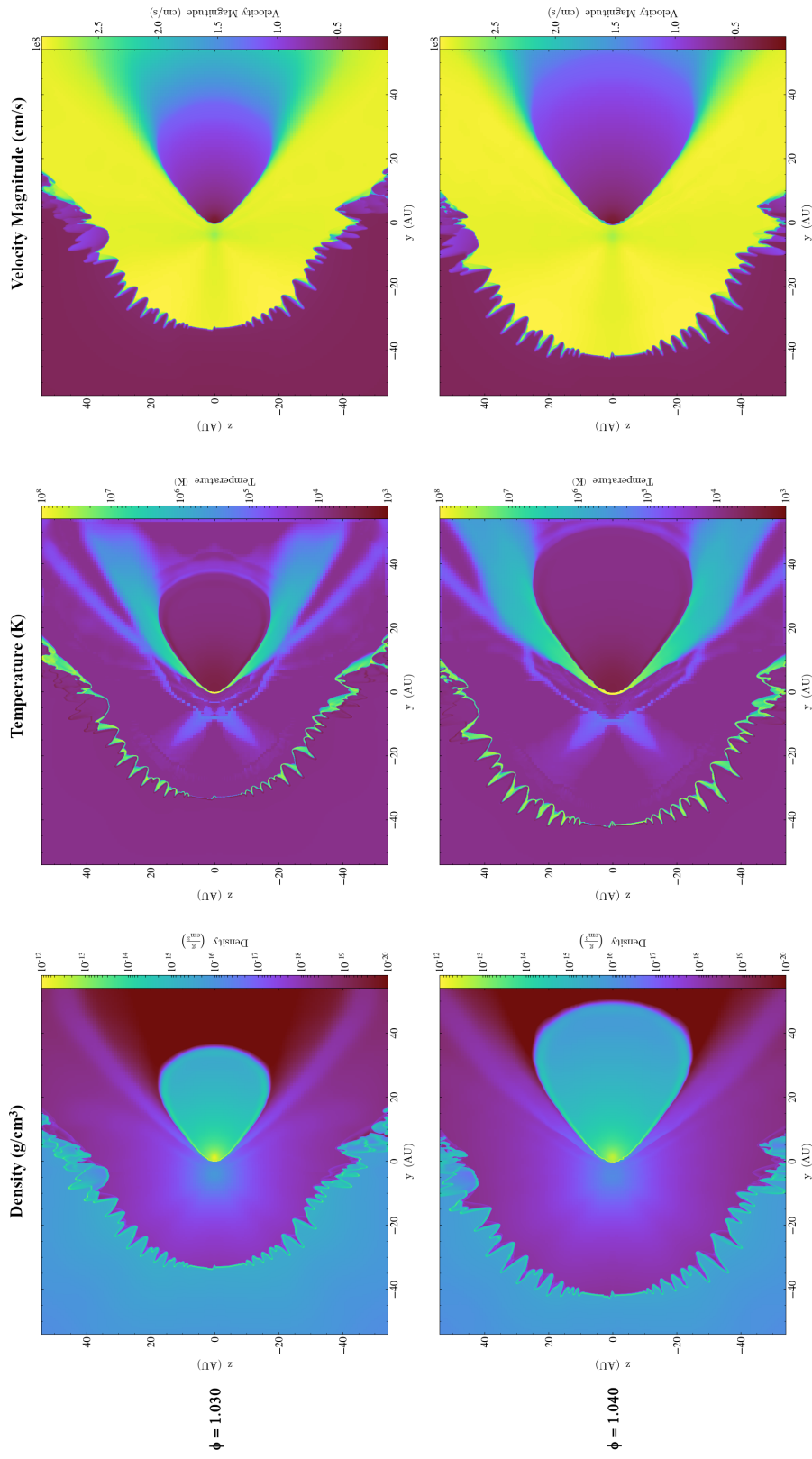
CHAPTER 7
DISCUSSION

7.1   Comparing SPH and Grid-based AMR Simulations

When it comes to SPH versus grid-based AMR codes for computational fluid dynamics, each method has its advantages and disadvantages in modeling astrophysical problems. Both SPH and AMR methods have experienced developments from as early as the 1970s to throughout the 2000s, see (Madura 2010) for a short historical context. The common advantage of both methods is the ability to model large-scale three dimensional fluid dynamics, now applied to problems in astrophysics, and more specifically, towards η Car's complex colliding binary winds. In modeling η Car, SPH was primarily used to constrain the binary system's orbital orientation (Madura et al. 2012). The primary advantage now in making use of a grid-based AMR code over SPH is the ability to better numerically resolve the shocks and instabilites in the WWC region using modern advanced computational processing facilities. This is particularly true since the SPH method is notorious for under-resolving hydrodynamical instabilities (Madura et al. 2013).

To summarize, modeling η Car with SPH has its advantages, specifically, in simulating the large-scale global outflows, which are still not practical with even AMR methods. Where SPH is not capable of resolving features in higher resolution, grid-based AMR can make up for the lack of refinement. The SPH method treats fluids as a mechanical and thermodynamical particle system. Modeling η Car's outflows via advection is possible with SPH. Interfacing problems are not an issue since a set of particles can be described by one material. The changing in resolution is dependent on position and time. This also means that computational speed is more efficient as higher density regions automatically receive more particles, helping

$\phi = 1.000$
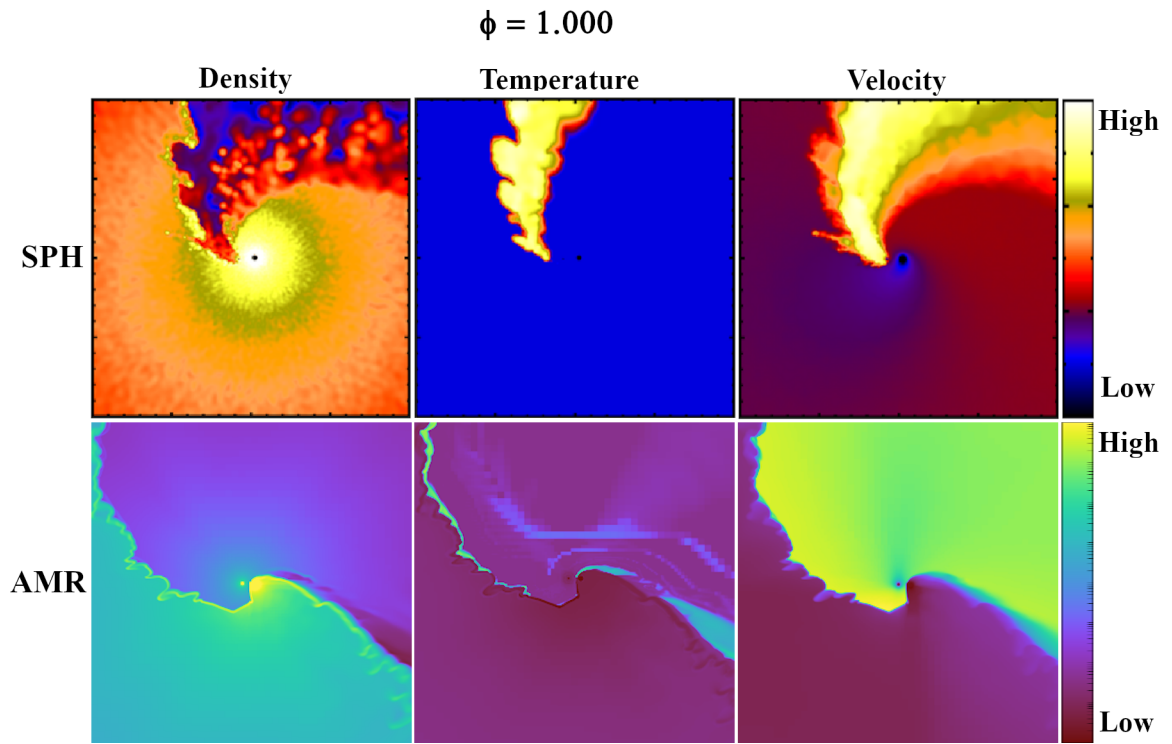
Figure 7.1: A side-by-side comparison of results from a 3D SPH (top row, from Madura et al. 2013) and AMR (bottom row, this thesis) simulation of η Car within similar domain ranges (SPH is ± 15 AU while AMR is scaled to ± 20 AU). Panels show slices in the orbital plane at a phase corresponding to periastron. Color shows, from left to right, density (log scale), temperature (log scale), and magnitude of the velocity (linear scale). This figure demonstrates the significant improvement in resolution obtained with the AMR method over the SPH method.

to save computational time since less dense regions receive fewer particles. Vorticity is not an issue as there is no grid system in place to account for the inbound and outbound flow calculations with grid boundaries. Particles that are bound within a domain are not lost through SPH, whereas in grid-based AMR, some fluids are lost in simulation. Visualization is important in studying the properties of η Car, where SPH allows for a straightforward detailed analysis (Madura 2010).

There are some disadvantages to using the SPH method though. In low density regions, calculations of dynamics are not quite as accurate as those in high density regions. Poisson noise becomes an issue for a complex simulation like η Car, and the level of accuracy is lowered for small perturbations. One other disadvantage of SPH concerns the idea of resolution. Decreasing grid cell size in a grid-based code in order to increase resolution is proportional to computational time, since there is a need for the increase in number of grid cells in each dimension. However, doubling the spatial resolution of a 3D SPH simulation requires 2^3 more particles. Thus, increasing the resolution of a 3D SPH simulation can quickly increase the computational costs, with still no guarantee that low-density regions and shocks will be properly resolved.

Now with the availability of high-performance computing clusters, the use of grid-based AMR codes can make up for the shortcomings of SPH. Figure 7.1 shows a side-by-side comparison among the plots of density, temperature, and velocity from the AMR simulation in this thesis with a previous SPH simulation performed by (Madura et al. 2013). The results of the AMR simulation are clearly at a much higher resolution compared to the SPH simulations. In the AMR scheme, the dense regions are held at higher levels of resolution, while lower-density regions are kept at a lower resolution, allowing for computational efficiency in a "tree-based" code, as discussed by (Teyssier 2002). When moving up a step in level of refinement, areas

susceptible to perturbations are then targeted for computation with a decrease in grid size. Although computational time increases with the increase in the number of grid cells, AMR follows a strict rule on a smaller region to calculate, whereas SPH can provide a solution without a grid. In the simulation in this thesis, the levels of refinement go up to a level of 14, and it is possible for an even higher increase in the level of refinement given adequate computational resources. To the benefit of AMR, figure 7.1 shows at higher resolution the various physical instabilities that occur as a result of η_B's faster, lower-density wind creating a velocity shear along the higher-density and slower wind of η_A. These instabilities were discussed in detail in the previous chapter. The SPH simulation does a poorer job of resolving the detailed structure of the WWC region and the instabilities within it. This is not ideal if one hopes to eventually use the results of 3D simulations to reproduce and explain various observations.

Nonetheless, there are similarities between the SPH and AMR simulation results. Figure 7.1 shows that both methods produce the spiral distortion of the WWC cavity due to increased orbital speeds around periastron. The asymmetry in the temperature of the shocked gas in the leading and trailing arms of the WWC region is also generally reproduced. However, with higher resolution, temperatures on the AMR simulation follow a much thinner spatial region along the line of the CD. The post-shock primary wind is also much thinner, denser, and exhibits more physical instabilities in the AMR simulation. Some remaining heated gas exists along the trailing arm of the WWC zone in the AMR simulation, but no such heated gas exists in the trailing arm in the SPH simulation, likely due to an inability to properly resolve the shock in the trailing arm. The WWC opening angle at this phase is also much more acute in the SPH simulation. Finally, the switch between adiabatic and radiative cooling in the post-shock η_B wind seems to be

consistent in both simulations. Overall, the AMR method proves itself to be superior when it comes to simulating small-scale features, shocks, and instabilities, so long as sufficient computational resources are available.

7.2   Application to Observations and X-ray Variability

This 3D hydrodynamic modeling sees its application in eventually qualitatively and quantitatively detailing the structure, orientation, and changes in mass loss in η Car. Efforts in constraining the properties of η Car have always been the goal of 3D modeling, and to further understand details where observations are limited in ability to capture the entire picture. Hydrodynamic modeling furthermore helps lay the foundation in determining the intrinsic properties at the core of the Homunculus nebula. An example are the observations of forbidden emission line structures by HST that were used to constrain the 3D orientation of η Car's binary orbit (Madura et al. 2012) and primary star mass-loss rate (Madura et al. 2013). Changes in mass loss rate were modelled using SPH simulations and used to interpret various observations of η Car throughout its 5.54 year binary orbit (Madura et al. 2013). Simulation results can also be used to predict changes in observations leading into future periastron passages. Observations of various absorption lines can also be compared with simulations to better understand the instabilities arising in the post-shock winds within the WWC, as done by (Richardson et al. 2016). The absorption features are carefully compared to detailed SPH simulations for the interpretation of He lines.

Modeling changes in the stellar wind speeds as the orbital velocity increases can give different perspectives and help with understanding the observed emission and absorption lines within the WWC zone (see Damineli et al. 2008). While portions of the WWC regions and Homunculus are illuminated by or shadowed from

different types of stellar radiation during the orbit, a 'lighthouse effect' occurs as a result of the observer's line of sight (Madura 2010). Ultimately, such lighthouse effects are the key identifier in the determination of η Car as a binary system. The periodicity gives further clues in all wavebands, including the important X-ray band, as discussed by (Corcoran et al. 2017). The X-ray variability is recognized to arise from the WWC zone between the stars and modulated by the orbital motion. X-rays have thus been one of the most important observational diagnostics of the η Car system, helping to constrain the orbital, orientation, and stellar wind parameters (Madura et al. 2013; Corcoran et al. 2017).

The results of 3D hydrodynamical modeling like that performed in this thesis can be applied to help understand various X-ray observations in further detail. Arguably, periodic X-ray variability gives one of the most direct views of η Car's intrinsic properties (Corcoran et al. 2017). This AMR simulation makes modeling such periodicity in detail possible. The model periodicity then gives a comparison for X-ray periodicity with past periaston events. Additionally, there is the extended η Car X-ray minimum, which is defined by a prior gradual rise in X-ray brightness, followed by a sudden rapid decrease to a minimum that lasts several months (Corcoran et al. 2017). Variations that arise in the X-ray emission and absorption due to changes in the stellar wind properties of either star come with weakly correlated explanations. By refining and improving on the 3D modeling of the various physical instabilities in the WWC zone, a much clearer understanding of the observed variations in the X-ray emission can be obtained.

7.3   Future work

The AMR simulation in this thesis has primarily been focused on understanding the behavior of η Car's binary wind-wind collision across periastron.

Due to time and computational resource constraints, a complete 3D hydrodynamical model of η Car's entire 5.54-year binary orbit is not fully captured in this thesis. The modeling of the entire orbit is left for future work, as running a complete orbit using the RAMSES AMR code takes a significant amount of time, even when using NASA Ames supercomputing facilities. In any case, even without a complete orbit simulation, many observational diagnostics can be qualitatively and quantitatively modeled, including the most interesting parts of the X-ray light curve, X-ray spectra, optical and UV spectra, optical light curves, interferometric infrared imaging, and more. The basic structure of the η Car system around apastron is relatively well understood thanks to earlier simulations and analytic analyses like that in (Canto et al. 1996). Apastron is much easier, and less interesting, to model since orbital velocities are much slower and the WWC region is more symmetric. Modeling apastron at this time would simply represent a waste of computational resources due to the time required to simulate such a broad and relatively uninteresting part of the highly eccentric orbit.

Stellar wind velocity and the role of radiative cooling have been primary themes in this thesis, in addition to running a simulation at periastron. The effects of orbital separation on wind velocity and the efficiency of cooling, and how both change with orbital phase, play a key role in the various instabilities that arise in the WWC zone and the presence of extremely hot ($\sim 10^8$ K) post-shock gas. Undetermined are how, exactly, wind velocities change in the real η Car system with orbital motion, and how such changes affect numerous observables, including X-rays. Nevertheless, the results in this thesis further support the idea that radiative cooling of the post-shock η_B wind is primarily responsible for the disappearance of hot X-ray emitting gas, the "collapse" of the WWC region during periastron passage, the extended X-ray light curve minimum, and the unpredictable

nature of the X-ray light curve recovery out of minimum (Madura et al. 2013; Corcoran et al. 2017). The β-velocity law nature of the stellar winds helps facilitate the transition from adiabatic to radiative cooling in the post-shock η_B wind during periastron by helping to slow η_B's wind to well below its terminal speed before collision, since the cooling parameter $\chi \propto v_{\mathrm{wind}}^4$.

CHAPTER 8
CONCLUSION

The mysterious binary system known as η Car, located ~ 7500 light years away, contains two massive stars with a combined mass of $\gtrsim 120$ $M_\odot$. It is surrounded by the bipolar Homunculus nebula, a shroud of dust and gas formed in the aftermath of "The Great Eruption" during the 1840's, when η Car reached peak brightness. Meanwhile, η Car sits at the core of the Homunculus nebula, illuminating it at an incredible luminosity of 5×10^6 $L_\odot$. The primary star of η Car is estimated to be ~ 90 $M_\odot$ and the secondary ~ 40 $M_\odot$. However, historical eruptions may indicate even larger values of the masses due to the occurrence of mass loss over time. Continuous stellar winds driven by radiation pressure and occasional mass outbursts are responsible for decreases in total system mass. This places η Car in the class of LBVs. In between both stars a collision of the stellar winds occurs, which makes η Car an interesting laboratory to study the physics behind massive star mass loss and evolution. Periodic variable emission emanating from the WWC zone ranges from radio wavelengths up to gamma rays, allowing astronomers to make observations and build models of the system. In particular, state-of-the-art 3D modeling of η Car makes use of grid-based AMR hydrodynamical simulations, which will help improve constraints on the physical properties of η Car.

Prior to applying computational methods to model η Car and its colliding winds, this thesis summarized preliminary work on the physics of radiation-driven stellar winds that are responsible for continuous mass loss at rates of up to one Sun every thousand years. The inherent nature of η Car places the system in the upper range of the HR diagram, and above the HD limit for stability of stars. The HD

limit is defined by the Eddington limit, where the radiation pressure can exceed local gravity. Achieving sufficient force to overcome gravity requires an extreme luminosity. η Car's luminosity is one of the most significant of all known stars.

Radiation driving of stellar winds depends on the concept of stellar opacity. Photons carry momentum and can scatter off of free electrons in the atmosphere of a star. At the atomic level are Compton and Thompson scattering effects that can potentially lead to a mass outflow and hence a stellar wind. However, more efficient for stellar wind mass loss is line-driven acceleration. Starting with the momentum and force balance between gravity, mass loss rates are then defined while incorporating factors related to stellar opacity. Discrete atomic lines determine the acceleration for the outflow of the wind via the use of fluid equations. A continuum of lines describing the global acceleration can be expressed by making use of the Sobelov approximation. The global expression for the line ensemble then leads to the one-dimensional point-star CAK model (Castor et al. 1975), referenced in describing the basis for the physics of radiation-driven stellar winds.

The wind-wind interaction of two point star sources of stellar winds can next be described through a fairly straightforward algebraic expression in the case when orbital motion is negligible. Following this are the conditions that lead to the momentum balance between the interacting winds. Density and wind velocity are important in the changing momentum balance at the contact discontinuity between the wind-wind shocks. Missing from this analysis are the temperatures of the winds. A cooling parameter, χ, is introduced as the ratio of the cooling time to the escape time. If $\chi > 1$, the gas behaves adiabatically, whereas if $\chi << 1$, the gas cools radiatively. Furthermore, $\chi \propto v_{\mathrm{wind}}^4$ and the distance to the contact discontinuity.

Beyond analytical methods are detailed numerical methods that have the ability to model the detailed physics, allowing for the interpretation of observations.

Two dimensional modeling begin in the 1990's as hydrodynamical codes and computers began to develop. Later on, as numerical methods and computing power improved, three dimensional hydrodynamical modeling became possible via e.g. SPH simulations. Current simulations now take advantage of grid-base AMR methods and high-end computational resources. In this thesis, a 3D hydrodynamical AMR code, `RAMSES`, originally developed for modeling galaxy formation, was used to model η Car's binary colliding winds around its periastron passage.

The results of this AMR simulation represent some of the highest resolution 3D simulations of η Car to date. We presented plots of density, temperature, and velocity from the AMR simulations. Slices were taken in the xy, yz, and xz planes at multiple orbital phases around periastron. As expected from analytical solutions, the results of this simulation show consistent results. The AMR results are also consistent with those of past 3D SPH simulations, although the AMR simulations presented in this theses do a much better job of resolving the colliding wind shocks and various physical instabilities that arise in the shocks. As for changes in wind momentum with the change in orbital phase, this AMR simulation shows the differences in cooling and wind velocity comparatively with the SPH results.

Ultimately, the results show that grid-based AMR simulations represent a significant improvement in the 3D modeling of η Car. Applications to observational diagnostics at X-ray, UV, and optical wavelengths will allow tighter constraints to eventually be placed on the stellar, wind, and orbital properties of η Car, and a better understanding of bizarre behavior like the non-repeatable recovery from the extended X-ray light curve minimum. Meanwhile, future work with AMR simulations opens the potential for 3D modeling at an increased level of refinement and resolution. With that, the history of η Car has been part of a long standing problem in the evolutionary cycle of stars. There are still many other mysteries

involved in creating a more clear image of the this system. We will hopefully resolve the mystery of η Car's mass loss history, which has always been a goal in uncovering the nature of η Car.

BIBLIOGRAPHY

Calderón D., Cuadra J., Schartmann M., Burkert A., Prieto J., Russell C. M. P., 2020, MNRAS, 493, 447

Canto J., Raga A. C., Wilkin F. P., 1996, ApJ, 469, 729

Carroll B. W., Ostlie D. A., 2014, An Introduction to Modern Astrophysics, 2nd Edition. Pearson

Castor J., Abbott D. C., Klein R. I., 1975, ApJ, 195, 157

Corcoran M. F., Liburd J., Russell C., et al. 2017, ApJ, 838, 45

Cranmer S. R., 1996, PhD thesis, University of Delaware

Damineli A., Hillier D., Corcocan M. F., et al. 2008, MNRAS, 386, 2330

Damineli A., Fernandez-Lajus E., Almeida L. A., et al. 2019, MNRAS, 484, 1325

Davidson K., Humphreys R. M., 1997, ARA&A, 35, 1

Glatzel W., Kiriakidis M., 1993, MNRAS, 263, 375

Gull T. R., Madura T. I., Groh J. H., Corcoran M. F., 2011, ApJ, 743, 1

Hamaguchi K., Corcoran M. F., Pittard J. M., et al. 2018, Nature Ast., 2, 731

Humphreys R. M., 2019, Galaxies, 7, 1

Humphreys R., Davidson K., 1984, Science, 223, 243

Humphreys R., Davidson K., 1999, PASP, 111, 1124

Humphreys R., Davidson K., 2012, Eta Carinae and the Supernova Impostors. Astrophysics and Space Science Library, Vol. 384, Springer, Boston, MA

Humphreys R., Martin J. C., 2012, Eta Carinae: From 1600 to the Present. In: Davidson K., Humphreys R. (eds) Eta Carinae and the Supernova Impostors. Astrophysics and Space Science Library, Vol. 384, Springer, Boston, MA

Lemaster M. N., Stone J. M., Gardiner T. A., 2007, ApJ, 662, 582

Lucy L. B., Solomon P. M., 1970, ApJ, 159, 879

Madura T. I., 2010, PhD thesis, University of Delaware

Madura T. I., Gull T. R., Owocki S. P., Groh J., Okazaki A. T., Russell C. M. P., 2012, MNRAS, 420, 2064

Madura T. I., Gull T. R., Okazaki A. T., Russell C. M. P., et al. 2013, MNRAS, 436, 3820

Madura T., Clementel N., Gull T. R., Kruip C. J. H., Paardekooper J. P., 2015, MNRAS, 449, 3780

Morris P. W., Gull T. R., Hillier D. J., Barlow M. J., Royer P., Nielsen K., Black J., Swinyard B., 2017, ApJ, 842, 79

Okazaki A. T., Owocki S. P., Russell C. M. P., Corcoran M. F., 2008, MNRAS, 388, L39

Owocki S., 2005, Stellar Wind Mechanisms and Instabilities, Bartol Research Institute, University of Delaware, Newark, DE

Owocki S. P., Shaviv N. J., 2012, Instability and Mass Loss Near the Eddington Limit. In: Davidson K., Humphreys R. (eds) Eta Carinae and the Supernova Impostors. Astrophysics and Space Science Library, Vol. 384, Springer, Boston, MA

Owocki S., Cranmer S. R., Blondin J. M., 1994, ApJ, 424, 887

Rest A., Prieto J. L., Walborn N. R., Smith N., et al. 2012, Nature, 482, 375

Richardson N. D., Madura T. I., St-Jean L., et al. 2016, MNRAS, 461, 2540

Smith N., 2012, All Things Homunculus. In: Davidson K., Humphreys R. (eds) Eta Carinae and the Supernova Impostors. Astrophysics and Space Science Library, Vol. 384, Springer, Boston, MA

Smith N., Frew D. J., 2011, MNRAS, 415, 2009

Smith N., et al., 2018, MNRAS, 480, 1457

Sobolev V. V., 1960, Moving Envelopes of Stars. Harvard University Press

Steffen W., Teodoro M., Madura T. I., Groh J. H., et al. 2014, MNRAS, 442, 3316

Stevens I. R., Blondin J. M., Pollock A. M. T., 1992, ApJ, 386, 265

Teyssier R., 2002, A&A, 385, 337

Van Genderen A. M., 1984, Space Sci. Rev., 39, 317

Vink J. S., 2012, Eta Carinae and the Luminous Blue Variables. In: Davidson K., Humphreys R. (eds) Eta Carinae and the Supernova Impostors. Astrophysics and Space Science Library, Vol. 384, Springer, Boston, MA

van Altena W. F., Lee J. T., Hoffleit D., 1995, VizieR, p. I/174